Timing Analysis of the Accreting X-Ray Binary Cygnus X-1

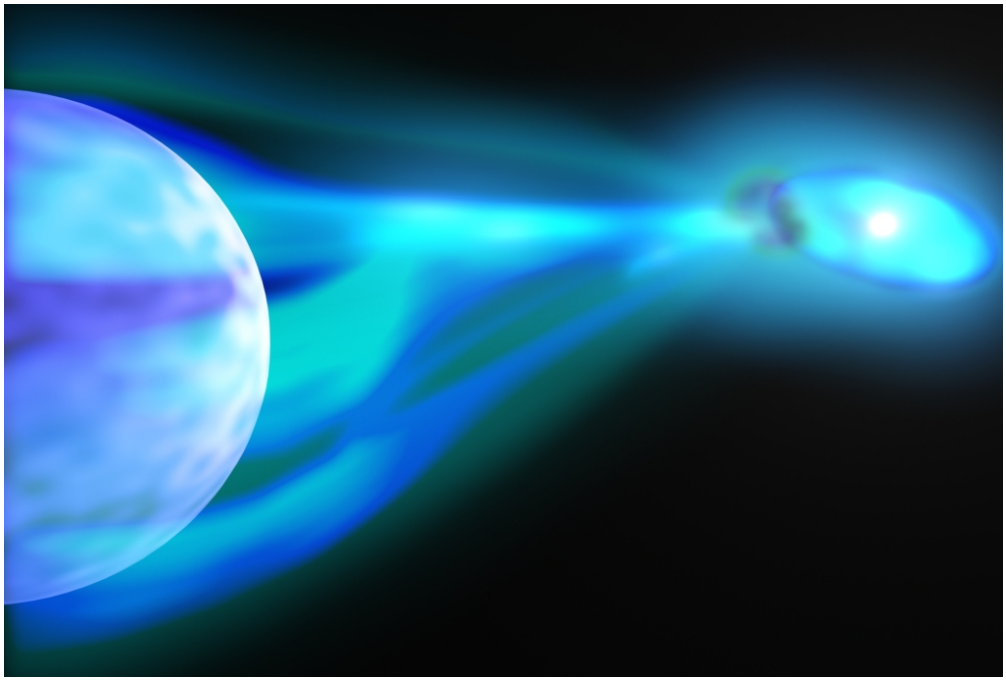

Diploma Thesis of

Stefan Pirner

Supervisor:
Prof. Dr. Jörn Wilms

March 2009

performed at the
Dr. Karl Remeis-Sternwarte Bamberg

Cover picture: Artist's impression of an X-ray binary. © ESA

Timing Analysis of the Accreting X-Ray Binary Cygnus X-1

Stefan Pirner

6. März 2009

Erweiterte deutsche Zusammenfassung

Stefan Pirner

Zeitreihenanalyse des akkretierenden Röntgendoppelsterns Cygnus X-1

Diese Arbeit beschäftigt sich mit der Analyse der Röntgenstrahlung des Galaktischen Schwarzen Lochs Cygnus X-1. Der Schwerpunkt liegt hierbei auf Zeitreihenanalysen von Röntgenlichtkurven, die mit einem Satelliten aufgezeichnet wurden. Bei den Beobachtungen handelt es sich natürlich nicht um direkte Beobachtungen des Schwarzen Loches selbst, da gemäß der Definition dieser Objekte, keinerlei Information aus dem Bereich innerhalb des sogenannten Ereignishorizontes nach außen dringen kann. Da das Schwarze Loch aber Bestandteil eines Doppelsternsystems ist, in dem es mit seinem Begleiter wechselwirkt, können Informationen aus der direkten Umgebung des Schwarzen Lochs gewonnen werden.

Die Daten, die in dieser Arbeit analysiert werden, wurden mit den Instrumenten des Rossi X-Ray Timing Explorer gemessen. Seit nunmehr über 10 Jahren existiert eine Langzeitbeobachtungskampagne, bei der im zweiwöchentlichen Rhythmus Beobachtungen von Cygnus X-1 erhalten werden. Der Großteil dieser Daten ab 1999 wurden hierzu extrahiert. Da Röntgendoppelsterne in vielen Fällen nicht nur im Röntgenbereich sichtbar sind, sondern auch in anderen Wellenlängen Strahlung emittieren, wurden zusätzlich noch Radiodaten des Ryle-Teleskops in England hinzugezogen. Das erste Kapitel dieser Arbeit erklärt diese Geräte. Im zweiten Kapitel wird auf die Klasse der Röntgendoppelsterne näher eingegangen. Durch die starke Anziehungskraft des Schwarzen Loches wird seinem Begleiter Sternmaterie entrissen, welche in das Gravitationsfeld des kompakten Objektes gezogen wird. Der Prozess der Massenakkretion ist eine Form der Energieumwandlung, die die der Kernfusion in Sternen, wie z.B. unserer Sonne an Effektivität bei weitem übertrifft. Durch den vorhandenen Drehimpuls des akkretierten Materials, kommt es zur Ausbildung einer Akkretionsscheibe um das Schwarze Loch. Von diesem Akkretionsfluß wird die Röntgenstrahlung abgestrahlt. Verschiedene Modelle solcher Quellen erklären diese als Comptonisierung, Synchrotronstrahlung, Schwarzkörperstrahlung oder Prozesse die mit dem Ausstoß eines Jets zusammenhängen. Je nach Art der Emission werden solche Röntgenquellen in Zustände eingeordnet.

Im Laufe dieser Arbeit wurden Werkzeuge programmiert, um die Zeitreihenanalysen auf den Computern der Dr. Karl Remeis-Sternwarte in Bamberg durchführen zu können. Die Algorithmen und Methoden des "Röntgentimings" waren Gegenstand vieler Veröffentlichungen der letzten 20 Jahre. Die Software, die hierfür geschrieben wurde, basiert auf den Fourieranalysemethoden, die in der Dissertation von Katja Pottschmidt (Pottschmidt, 2002) zusammengefasst sind. Das vierte Kapitel gibt eine Zusammenfassung über die Berechnungen, die ausgeführt werden müssen, um Größen, wie die spektrale Leistungsdichte, Kohärenzfunktion und die Verzögerung der Messungen in verschiedenen Energiebändern berechnen zu können. Ein weiterer Teil der Analyse der Messdaten wurde damit verbracht Spektren der Quelle zu erzeugen, um die Zeitreiheneigenschaften mit denen der Spektren vergleichen zu können.

Um genau die Vergleiche erzielen zu können, muss der komplette Datensatz modelliert werden. Eine Beschreibung dieser Fit Funktionen wird in Kapitel 5 abgehandelt. Die Spektren wurden mit einem phänomenologischen Modell gefittet, welches in der Rontgenastronomie weit verbreitet ist. Die Leistungsspektren der Quelle lassen sich am Besten mit zwei Funktionen modellieren. Zum einen erscheint ein breitbandiges Rauschen in den spektralen Leistungsdichten, welches mit Lorentz-Kurven modelliert werden kann, zum anderen findet ein Potenzgesetz mit exponentiellem Cutoff Verwendung. Bekannte spektrale Zustände von Cygnus X-1 lassen sich durch die Parameter dieser Funktionen wiedergeben. Im abschliessenden Kapitel werden die Korrelationen, die innerhalb der Leistungsspektren, als auch zwischen Spektren und Leistungsspektren gefunden wurden dargestellt und diskutiert. Zu Zeitpunkten an denen sich der Strahlungszustand der Quelle ändert, lassen sich Änderungen in den Zeitverzögerungen zwischen den einzelnen gemessenen Energiebändern erkennen.

Contents

1 Introduction **1**
1.1 X-ray Astronomy . . . 1
1.2 Thesis Outline . . . 1

2 The Instruments **3**
2.1 The Rossi X-Ray Timing Explorer . . . 3
2.1.1 PCA – Proportional Counter Array . . . 4
2.1.2 HEXTE – High Energy X-ray Timing Experiment . . . 6
2.1.3 ASM – All Sky Monitor . . . 7
2.2 Radio Data – The Ryle Telescope . . . 8

3 X-ray sources **11**
3.1 Black Holes . . . 12
3.2 X-ray Binaries . . . 14
3.3 Accretion Disks and Jets . . . 15
3.4 X-rays and Radiation Processes . . . 17
3.4.1 Black Body Radiation . . . 17
3.4.2 Comptonization . . . 18
3.4.3 The Iron Fluorescence Line . . . 18
3.4.4 Synchrotron Radiation . . . 19
3.5 States of Black Hole Binaries . . . 20
3.6 Cygnus X-1 and HDE 226868 . . . 23
3.6.1 The Binary System . . . 23
3.6.2 Orbital period . . . 24
3.6.3 Superorbital periods . . . 25
3.7 Short-term Variability of accreting BHB . . . 26

4 Data Extraction and Computation **31**
4.1 The Cyg X-1 Monitoring Campaign . . . 31
4.1.1 Data . . . 32
4.2 Timing Analysis . . . 33
4.2.1 Preparation of Lightcurves . . . 33
4.2.2 Power Spectral Density - PSD . . . 34
4.2.3 Normalization of the PSD . . . 36
4.2.4 Noise and Deadtime Influence on the PSD . . . 38
4.2.5 Cross Power Density - CPD . . . 40
4.2.6 The Coherence Function . . . 41
4.2.7 Phase and Time Lags . . . 42

5 Modelling the Data **45**
5.1 Spectral Fitting . . . 45
5.2 Timing Models . . . 48
5.3 Determining the right model . . . 51

6 Results for Cygnus X-1 **55**
6.1 Spectral Evolution . . . 55
6.1.1 Spectral Classification . . . 55
6.1.2 Correlations of the Broken Powerlaw . . . 58
6.1.3 The Iron Line Complex . . . 60
6.2 Spectro-Timing Analysis . . . 60
6.2.1 PSD Overview . . . 60
6.2.2 PSD Fit Results . . . 61
6.2.3 RMS–Frequency Correlation of the PSD . . . 64
6.2.4 Time Lag Spectra . . . 67
6.2.5 Cyg X-1 Evolution Overview . . . 70

7 Summary & Outlook **77**

References **79**

List of Figures **84**

Acknowledgements **87**

Chapter 1

Introduction

1.1 X-ray Astronomy

The field of astronomy was for a long time bound to the sense of sight. This changed completely with the inventions of the 20^{th} Century. New technologies enriched the field of astronomy. Radio transmission technology was used and by fluke a signal, which was originating from outside the atmosphere was discovered. The possibility to leave the Earth's atmosphere opened the window to the complete band of electromagnetic radiation. Even before 1950, rocket flights discovered X-ray radiation from the sky.
Nowadays the situation is very comfortable for astrophysicists. A large number of satellites observing the sky in infrared, visible, ultraviolet, X-ray and γ-ray light. Radio telescope arrays do the same on the other edge of the electromagnetic spectrum. Even other information sources like charged particles or neutrinos are nowt in use to gather more information about the cosmos. A look at Fig. 1.1 shows, how small the windows of the old astronomers was in comparison to today. This work uses two of the techniques mentioned above. A radio telescope array in Great Britain and one of NASA's satellites, a old workhorse of X-ray astronomy, the Rossi X-Ray Timing Explorer pointing on a source which is emitting at all energies. The source is at least as interesting as the technologies used to observe it. It is a system of two objects orbiting each other, where the one companion is not visible with the eye, even not with the best optical telescopes. The object is bright in X-rays, while it eats the atmosphere of its companion. A star was at this position many years ago, which ended his life and exploded. The remnant is a stellar corpse with such density that it can hold photons. The speech is about a black hole, namely Cygnus X-1 and its companion HDE 226868, a giant blue star, which are subject of the analyses in this work.

1.2 Thesis Outline

This work focuses on the analysis of the X-ray emission which originates from the stellar-mass black hole binary Cygnus X-1. The main goal is the computation of timing properties by using Fourier techniques and their interpretation. The calculated quantities are opposed to measured X-ray spectra and classifications is given. The database of satellite based X-ray measurements implies ten years and as far as possible simultaneous radio observations are taken into account.
The work is structured as follows:
In Chapter 2 the instruments which were used to obtain the data are discussed. The satellite Rossi X-ray Timing Explorer and the three instruments aboard this spacecraft with their excellent abilities for high time resolution observations are getting introduced. The technique of taking ground based radio observations is briefly described, as a well suited addition to high energy X-ray measurements.
Chapter 3 explains the nature of X-ray binaries and gives explanations for the different mechanisms

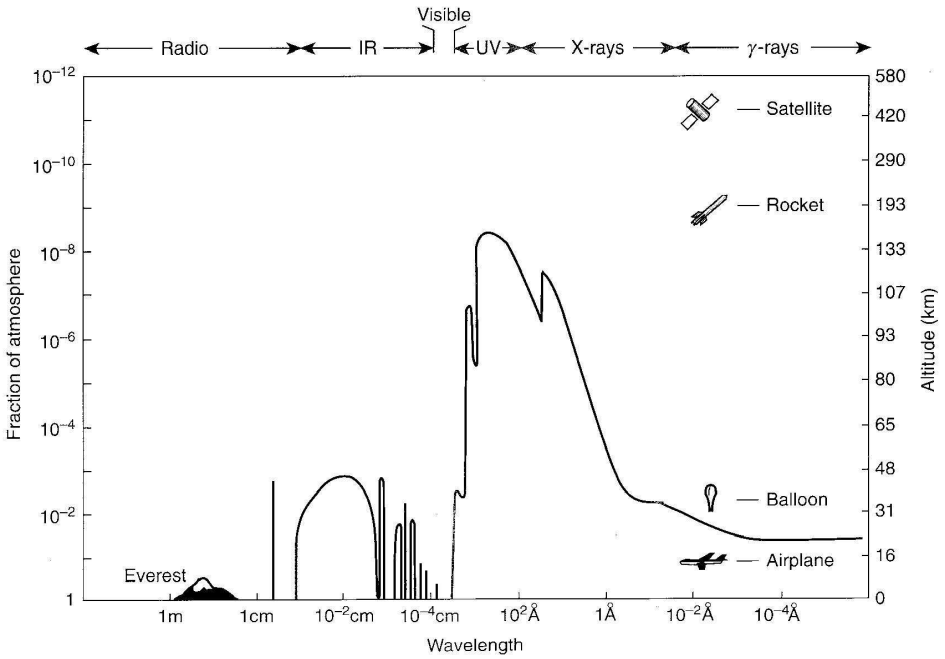

Figure 1.1: Penetration depth of electromagnetic waves into the Earth atmosphere. The solid line illustrates the altitude in which only the half of the incoming radiation remains. The only two wavelength bands in which radiation can penetrate to the ground are at radio wavelength and in the optical window. (Charles & Seward, 1995, Fig. 1.12)

causing X-ray emission in this type of celestial sources are given. The process of accreting matter in the strong gravitational field in the vicinity of a black hole is sketched. The process itself, manifesting as a hot blackbody emitter, and its effects on the surrounding space, like the existence of a Comptonization corona and/our a jet outflow with relativistic velocities are to be considered as source of X-ray photons. The last part of this chapter is dedicated to the source Cygnus X-1 and the class of black hole binaries.

Chapter 4 gives a summary about the processed data which were used to obtain the results of this work. Section 4.2 describes the software which was written to perform the timing analysis, and the underlying Fourier transformation. The data are divided into six energy bands. Their light curves, which were extracted from raw satellite data, are put into the software to compute power spectra (PSDs) for each of those energy bands. Furthermore, Fourier quantities, like coherence and time lag spectra, are calculated, which depend on simultaneous light curves from two different energy bands.

Chapter 5 gives an overview about the models which are fitted to the data. The data is divided into two parts at this point. On the one hand the power spectra show typical behavior and it is possible to model those with a few functions. On the other hand, the spectra obtained from the satellite's observations are fitted with an empirical model, which is known from preceding works. Both results, the spectral as well as the timing fit parameters, are groundwork for the analysis presented in the last chapter.

Chapter 6 displays the results of ten years of biweekly observations of Cygnus X-1. Section 6.1 shows how the X-ray emission of Cygnus X-1 changes with time and which implications can be seen in changes of the spectral parameters. Section 6.2 gives a summary of the timing results. There is a known spectral evolution of the source, in addition there is an analogical evolution in the timing properties. In order to describe the X-ray source as a whole, it is necessary to find correlations between spectral and timing data. The different emission states, in which a black hole binary resides in, are known from the spectral approach. They can be similarly described with the timing quantities. This combined spectro-timing analysis is done at the end of that chapter.

Chapter 2

The Instruments

In this work two completely different parts of the electromagnetic spectrum are analyzed. As mentioned in Chapter 1, only a small fraction of electromagnetic radiation reaches the Earth's surface. One has to deal with this problem in the case of X-ray radiation, which is completely absorbed by the atmosphere. The only possibility to achieve long and uninterrupted observations of a celestial X-ray source is to leave the atmosphere and take the advantage of a satellite. The other part of the data are radio measurements. The radio data can be taken from the ground, because of the transparency of the atmosphere for this kind of radiation. In this chapter the two instruments are introduced and the measurement techniques are explained.

2.1 RXTE - The Rossi X-ray Timing Explorer

The *Rossi X-ray Timing Explorer (RXTE)*, named after Bruno B. Rossi, an Italian astrophysicist, who worked in the the field of X-ray astronomy and discovered the first X-ray source (Scorpius X-1) outside our solar system. *RXTE* was launched end of December 1995 into a low earth orbit with an altitude of about 580 km and an inclination of 23°. The orbital period of such an low earth orbit lies at about 90 minutes. *RXTE* can take long observations of the whole X-ray sky except for directions close to the sun, as the infall of the strong radiation originating from the sun would damage the sensitive instruments and the solar panels of the spacecraft are mounted orthogonal to its pointing direction, therefore the power supply would fail in this direction. But there are two other restrictions to the observability of objects:
If a source is not located near the celestial poles, the line of of sight from the satellite to the object is interupted once per orbit by a earth occultation. For the object examined in this work, Cygnus X-1, with an declination of +35° the occultation occurs almost every orbit and so the maximum uninterrupted observation time is about 60 minutes.

Another problem for the satellite and its instruments, and therefore a further constraint of the observation is the high radiation and particle density in the Earth's magnetic field. Charged particles are trapped radiation belts in the magnetic field at height of about 1000 km, named after their discoverer the "van Allen belts". *RXTE* basically is protected from these particles, as its orbit is below the van Allen belts. There is one region in the configuration of the magnetic field, namely the South Atlantic Anomaly (SAA), in the area of the east coast of Brazil over the Atlantic ocean. The magnetosphere has a bulge there, so the radiation belts penetrate to a lower height. If the satellite crosses this region, there is a very intense particle background radiation, which causes very high detector count rates on board the spacecraft and thus the observation becomes impossible due to the background countrates. Actually there is the danger of damaging the instruments, so for safety the instruments are shut down, when the satellite passes through the SAA. One instrument on *RXTE*, which is not part of the scientific experiments, stays always turned on: a particle monitor, one of the auxiliary devices on board *RXTE*. Fürst et al. (2009) used this device to investigate the shape, intensity and temporal behavior of the SAA over several years, as RXTE is one of the oldest

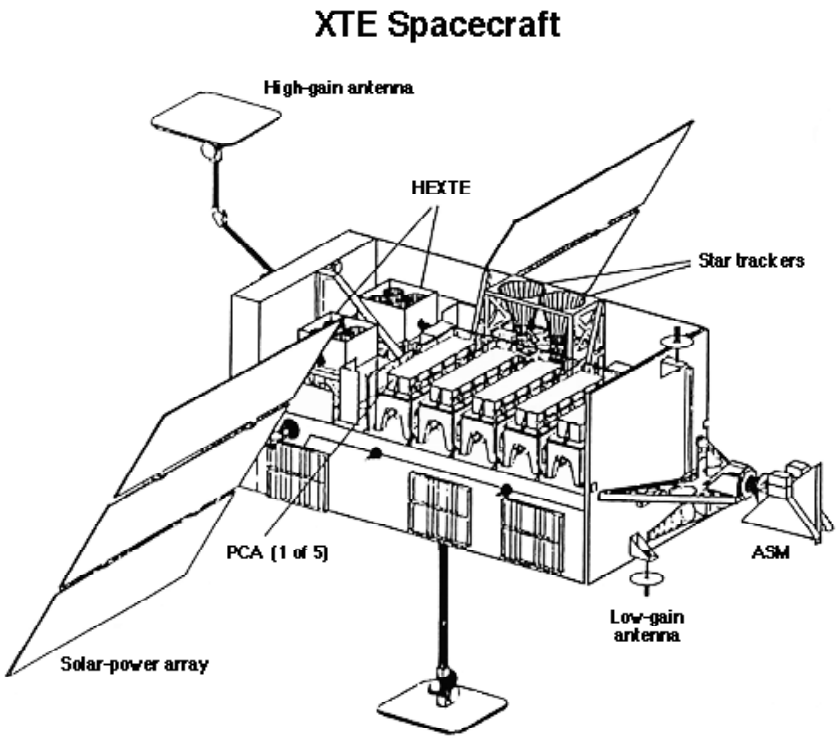

Figure 2.1: Schematic view of the *RXTE* spacecraft (picture taken from `http://heasarc.gsfc.nasa.gov/Images/xte/xte_spacecraft.gif`. The scientific instruments and the most important auxiliary devices are labeled. The HEXTE and PCA detectors are located in the body of the spacecraft, pointing in the same direction. The three shadow cameras on the ASM are located on the extension on the right side. The solar panels are the spacecraft's power supply. Two antennas send the acquired data to Earth and the two star tracker cameras are responsible for the correct orientation of the satellite.

in-service X-ray observatories. In Fig. 2.2 the schematic position of the SAA together with an example orbit of *RXTE* and the shape of the SAA as measured by ROSAT are shown. *RXTE* had a planned lifetime of 5 years, but is still in orbit and working. In the following sections the three experiments on board *RXTE* are described. A more detailed summary of *RXTE* can be found in Kreykenbohm (2004) and Bradt et al. (1993).

2.1.1 PCA – Proportional Counter Array

The most important instrument for this work is the Proportional Counter Array (PCA). It was constructed at NASA's Goddard Space Flight Center (GSFC) (Jahoda et al., 1996, 2006). PCA consists of five nearly identical proportional counter units (PCUs), each of them with several layers. There is one propane layer on top and four xenon filled layers below, each with a anode mesh. The propane layer and the bottommost xenon layer act as veto layers to distinguish between photons and other unwanted (charged) particles or between source photons and photons entering the detector from the side, respectively. Like HEXTE, the PCA has a collimator in front of each PCU to limit the field of view to 1°. All units together reach an effective collection area of $\sim$6500 cm^2. The experiment is designed to reach a very good time resolution of up to 1μs at the cost of a moderate energy resolution of 18% at 6 keV and a nominal energy range from 2 – 60 keV. In the mission's first years the PCUs had unexpected breakdowns caused by sparks in the detector chambers. As a countermeasure the PCUs are now no longer switched on all the time. Every unit is periodically switched off to bring the detectors back to a working level. Another measure was to lower the high

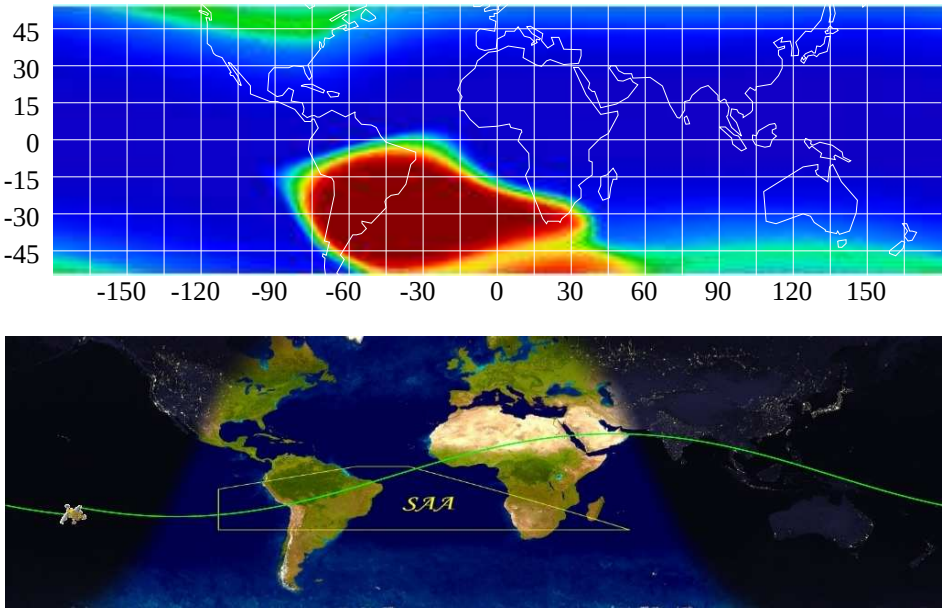

Figure 2.2: The picture on the top shows the location of the South Atlantic Anomaly as measured by *ROSAT*. (Kreykenbohm, 2004) *RXTE* has a smaller inclination and does not pass completely through this region. Below a schematic map of *RXTE*'s orbit. The theoretical position of the SAA, where the satellite is not able to operate, is indicated in the picture.(The picture can be found at `http://heasarc.gsfc.nasa.gov/docs/xte/SOF/CurrentLocation3.html`

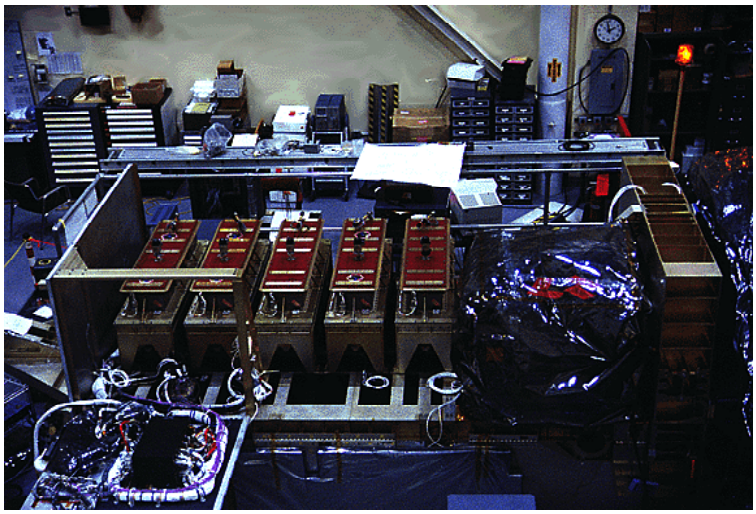

Figure 2.3: A view of *RXTE*'s assembly. Clearly visible are the five nearly identical proportional counter units (PCUs) of the proportional counter array in the body of the spacecraft. (`http://science.hq.nasa.gov/kids/imagers/ems/xrays.html`)

voltage of the detector nets in small steps. The lowering of the high voltage extended the energy range of the detector from 2 keV to now up to 100 keV, with the problem of changing energy response behavior and changing energy channels. Due to the age of the satellite, this detector has other troubles, too: The propane layer of PCU 0 was most likely hit by a micro meteorite and quickly lost pressure. This increases the background rate in this particular proportional counter and makes the data analysis of observations with PCU 0 switched on more difficult than others. Fig. 2.4 shows an example for a typical observation with the PCA with all of its problems. As discussed later (Chap. 4) one wishes to have long, uninterrupted lightcurves without changing the

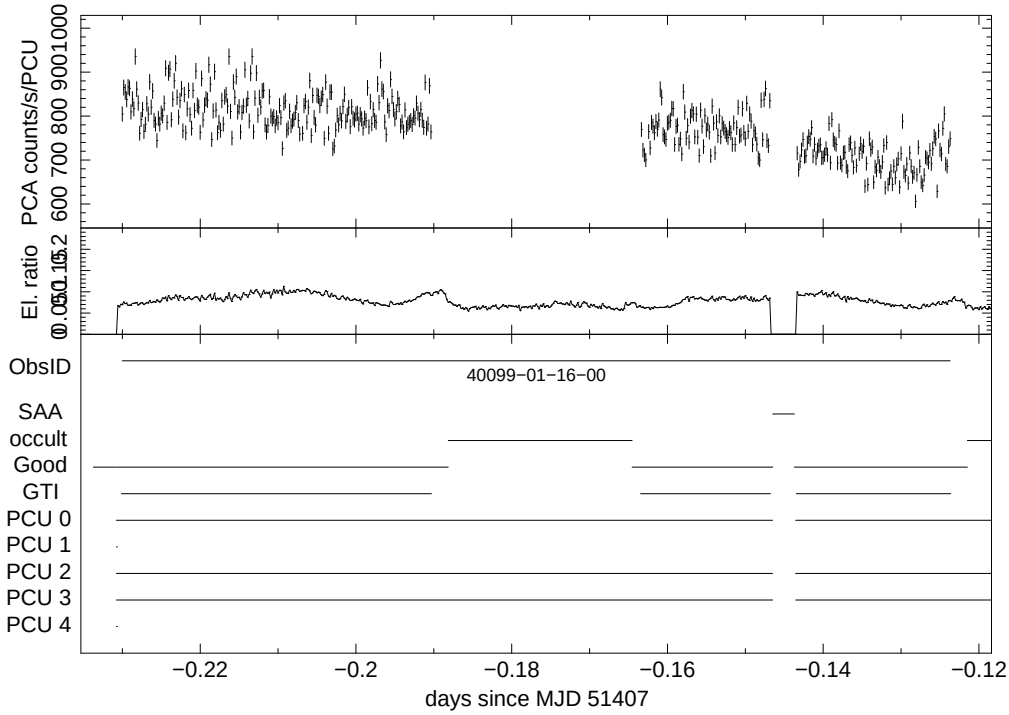

Figure 2.4: A typical observation of Cygnus X-1 with PCA is shown. The top panels shows the countrate per PCU. Below the electron ratio is plotted, which is a measure for the particle background. In the bottom panel the intervals are indicated, at which time a certain PCU is activated and when the satellite is in the SAA or the source is hidden behind the Earth (occult). The time intervals where no disturbing effect is active are the good time intervals (GTI), which indicate the timespace of a possible measurement.

combination of activated units. The figure shows the main problem that this is not possible to achieve so easily.

2.1.2 HEXTE – High Energy X-ray Timing Experiment

The second experiment aboard is the High Energy X-ray Timing Experiment (HEXTE Rothschild et al., 1998). It was built at the Center for Astrophysics and Space Sciences of the University of California in San Diego and is designed to cover the hard X-ray band from 15 – 250 keV in pointed observations. HEXTE consists of two clusters of four NaI/CsI-Phoswich scintillation detectors (Rothschild et al., 1998) each. A general description of this kind of detectors is given by Meschede (2002). In front of each detector a collimator is mounted to limit the field of view to 1°. The moderate spectral resolution of about 16% at 60 keV is counterbalanced by its good time resolution with a sampling rate up to 8μs. HEXTE is co-aligned with with the third instrument (PCA, see below) and both observe always the same target. However, the HEXTE clusters A and B are not fixed in their position. There is a so-called "rocking mechanism"(Gruber et al., 1996), which is used to determine the background radiation. This mechanism moves the cluster alternately on- and off-source, that means the position of the cluster is swapped through five possible positions ($\pm 3°$, $\pm 1.5°$ and on source). The two clusters do their rocking in orthogonal directions and the background can be extracted for each cluster separately, furthermore one can extract the background from the "+" position separated from the "–" position, if another X-ray source stands close to the one observed. Starting in March 2003 the electronics of the rocking mechanism of cluster A showed unusual behavior and had breakdowns. As this anomaly in switching on/off source became more frequent, the instrument team decided in October 2006 to switch off cluster A's rocking mechanism to make sure that it would not stop functioning in an off-source position. This complicated the background

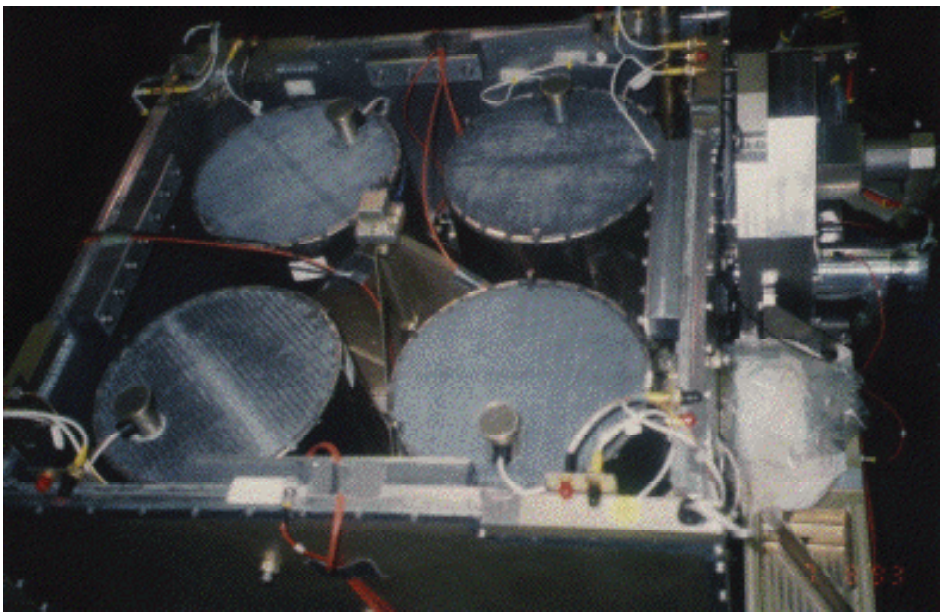

Figure 2.5: The four scintillation counters of one of HEXTE's clusters. There are two of these instrument aboard the satellite. (`http://heasarc.gsfc.nasa.gov/docs/xte/learning_center/hexte.html`

determination for this detector a lot. A calculation of the background from the cluster B data pointed out to be very difficult, because the two detectors have a different background behavior. Both clusters of the instruments show a different reaction on the particle background rates and therefore a extrapolation for cluster A is not easily possible (F. Fürst, priv. comm.).

2.1.3 ASM – All Sky Monitor

The All Sky Monitor (ASM) (Levine et al., 1996; XTE-Staff, 1995) is the only experiment on *RXTE* which is not designed for pointed observations. As its name indicates, ASM is designed to monitor the whole X-ray sky. X-ray sources are one of the most variable sources known. Some X-ray sources often change their spectral behavior or the flux changes dramatically on short timescales. Other ones have unsteady outbursts or appear as transient sources, which are quiet over many years and appear from one day to another with very strong X-ray fluxes. The ASM was built at the Massachusetts Institute of Technology (MIT) with the purpose of scanning the whole sky at least once a day. It consists of three shadow cameras, each with a field of view of $90° \times 6°$. Since in most cases in this wide field of view a number of X-ray sources are located, the coded mask technique is used. On top of each shadow camera a coded mask is located which produces a complicated shadow pattern on the detector below. This detector is a position sensitive proportional counter with an energy range from $\sim$ 2keV to 12keV. The shadowgram measured by the detector is telemetered to Earth and analyzed by computers. In this process a sky model is fitted to the data and thus one is able to reconstruct the position information and distinguish between the different sources observed at the same time. ASM is used primarily for two purposes. It contributes lightcurves from nearly all bright X-ray sources ($\gtrsim$ 10mCrab) over large timescales, so changes in the flux of a source can be monitored and correlated with measurements in other wavelength bands or pointed X-ray observations. On the other hand the ability to detect exceptional events in the X-ray sky, like transient sources or others mentioned above is of great importance and therefore it provides a basis for the decision if a short term pointed observation with the other instruments on *RXTE* should be made to get more data of such partially unknown phenomena in X-ray astronomy, which are worth being further analyzed.

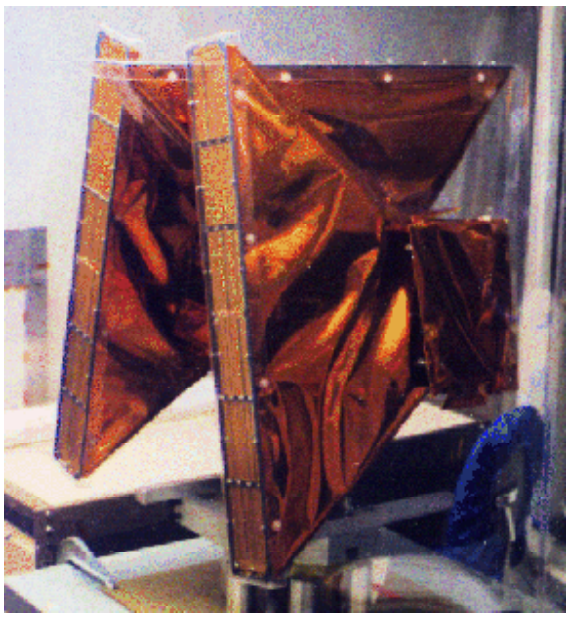

Figure 2.6: The three shadow cameras on the ASM. A position-sensitive proportional counter is located at the small end of each part, which detects the photons passing through the coded-mask on the top. (`http://heasarc.gsfc.nasa.gov/docs/xte/learning_center/asm.html`

2.2 Radio Data – The Ryle Telescope

Completely in contrast to the satellite described in the last section is the Ryle Telescope. Radio waves are among those wavelengths, which can penetrate the Earth's atmosphere and can be detected from the surface with radio telescopes. This easement of the measurement has of course a shady side: The angular resolution of a telescope depends on the diameter of the mirror D and the wavelength λ of the observed radiation. Because of the Rayleigh criterion,

$$\sin\theta = 1.22\frac{\lambda}{D} \tag{2.1}$$

the dish of a radio telescope has to be much larger than an optical mirror, because the wavelength of the radiowaves is in the order of millimeters, up to some metres. One needs to construct radio telescopes with dishes with a diameter of about 100 m or more to achieve an angular resolution in the order of about 1 degree. The resolution could be improved by constructing even larger dishes, what is not possible due to problems of statics and the immense cost of such devices. A corrective for this resolution problem is the invention of Very Long Baseline Interferometry (VLBI), which brings the angular resolution of radioastronomy not only in regions where scientific research is possible, furthermore it is with this technique the division of astronomy with the highest resolutions (Rohlfs & Wilson, 2004; Thompson et al., 2001). The principle of interferometry is the combination of many smaller telescopes spread over a wide area on the surface. The group of telescopes pointing to the same direction send their data with an exact timestamp an position information to a place, where the correlation is done. The array appears as one telescope with a dish diameter in the size of the longest distance between the two telescope farest away from each other. More telescopes can be placed in the plane of the baseline to achieve higher signal-to-noise ratios. The correlation process is done with powerful computers these days and still need a lot of computation time. Another restriction to radio astronomy is the commercial use of radio waves and the "radio pollution" caused by electric, radiating devices used by mankind like radar, telephony, navigation and heating. If an astronaut would have lost his mobile phone on the moon, this device would be among the strongest celestial radio sources (Böck, 2008, Chap. 3.1). Fortunately some wavelength bands with great importance for astrophysical research, like, among others, the 21 cm band, where the hyper finestructure transition of neutral hydrogen radiates, are protected for scientific use.

Radio fluxes are measured in units of Jansky (Jy). 1 Jy is defined as $10^{-26}\,\mathrm{W\,m^{-2}\,Hz^{-1}}$. Typical

Figure 2.7: The Ryle telescope in Great Britain. The antennas can be moved on rail tracks. The array consists of eight telescopes. Five of them are in a compact configuration here, as the photo was taken. (`www.mrao.cam.ac.uk/telescopes/ryle/`)

measured flux densities are $2 - 4 \cdot 10^6$ Jy for the sun and 15 mJy for Cygnus X-1. The radio data analyzed in this thesis were taken with the Ryle Telescope at Mullard Radio Astronomy Observatory (MRAO) in Cambridge (UK) at a wavelength of 2cm (15 GHz). The telescope array consists of 8 elements, identical in construction, with a 13 m dish. The telescopes are mounted on rail tracks, on which they can be moved over a wide area with the longest baseline of 4.8km. More information about the Ryle telescope is given by Pooley & Fender (1997) and Wilms et al. (2007).

Chapter 3

X-ray sources

In this chapter the description of X-ray binary systems is given. X-ray binaries are multiple star systems, where one companion has collapsed to a neutron star or black hole at the end of its life and is interacting in some way with its partner. At first it is explained what black holes are and how they are formed. Afterwards the physics of X-ray binaries are described and what radiation mechanisms are the reason for their X-ray detectability. In the last part the source observed in this work, Cygnus X-1, is introduced. The basic properties of this system and the characteristic spectral states are discussed.

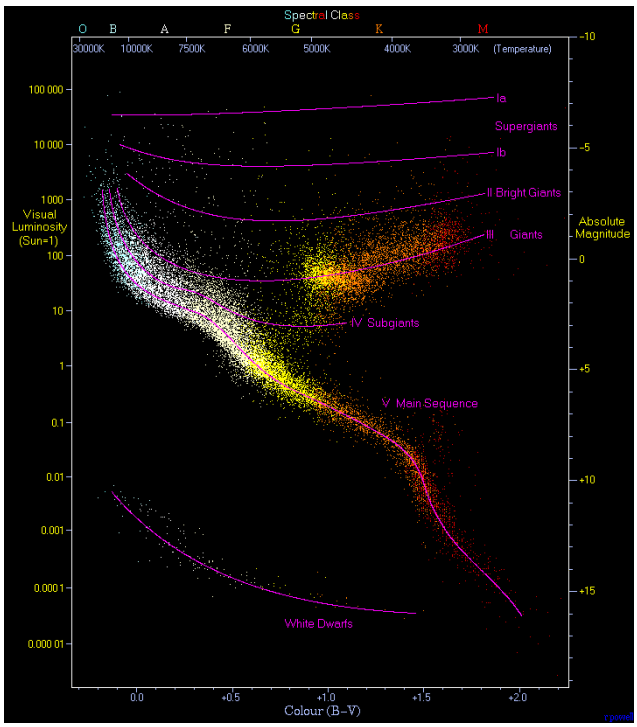

Figure 3.1: A Hertzsprung–Russell–diagram (HRD, taken from `http://www.atlasoftheuniverse.com/hr.html`. A HRD is a plot of the total luminosity of stars against their surface temperature or color, respectively. Hydrogen burning stars form a characteristic line across the diagram, called the main sequence.

3.1 Black Holes

A complete description of stellar evolution can be found in Karttunen et al. (2007). The important basics for the formation of a black hole are described in the following.
To form a black hole like Cygnus X-1 the predecessor star has to pass through all stages of stellar evolution and finally ends with a supernova explosion. Of course, not all stars meet the requirements to form such an object. All stars are formed out of dense clouds of gas and dust and begin their lives as hydrogen burning objects. The stability of the star is caused by the balance of its gravitational pressure and its countervailing gas pressure. In this state, the stellar parameters like mass, radius, luminosity, surface temperature and color are uniquely related. The stars remain for the bigger part of its lifetime in the main sequence until its fuel is depleted. The amount of nuclear fuel is proportional to the mass of the star, but the rate of nuclear fusion in the core is related to the mass, too and is growing stronger with increasing mass as the amount of fuel itself. This leads to different lifetimes for stars with different masses. While the sun with one solar mass is expected to exist for 10^{10} years, a star near the upper mass limit of about $120 M_\odot$ will consume the fuel in about 10^6 years. Fig. 3.1 shows a Hertzsprung-Russell diagram, which is a plot of stellar luminosity versus surface temperature. Here all hydrogen burning stars are located on the main sequence. If the hydrogen is depleted after the long phase of hydrogen burning on the main sequence, the star has to shrink due to the missing radiation pressure from the core. A lightweight star will end his energy producing life after this process as a white dwarf, a stable object, in which the degeneration pressure of the Fermi-gas of electrons withstands gravity (Iben & Renzini, 1983). If the star is more massive, the collapse generates higher temperature and higher pressure in the star's core, leading to the ignition of more burning phases. At first helium, the ash remaining of the hydrogen burning phase, will ignite and fuse to carbon. In big stars several phases of nuclear burning follow up one after another. The last nuclear reaction possible is the formation of iron cores. The energy balance of the fusion processes is positive up to iron, the formation of heavier elements would take more energy than it releases and is therefore not possible in stellar fusion processes. Heavier elements are produced in supernova explosions and shockfronts in the dense medium. The collapse is now irresistible and the consequence is a super nova explosion. White dwarfs can only exist with masses below a certain limit, the Chandrasekhar Limit of $1.4 M_\odot$ (Chandrasekhar, 1931a,b).

The gravitational pressure of collapsars above the Chandrasekhar Limit forces the electrons to combine with protons and a neutron star is formed (Heger et al., 2003). Now the degeneracy pressure of the neutrons withstands gravity. In X-ray binaries, where the neutron star is accreting matter from a companion star, or as a pulsar, which are neutron stars with strong magnetic fields not coaligned with their rotation axis, neutron stars can be observed. In the latter case, a pulsating signal can be found, if the magnetic poles point towards the earth periodically during the rotation.

For neutron stars there is again an upper mass limit of about $3 M_\odot$ (Oppenheimer & Volkoff, 1939; Oppenheimer & Snyder, 1939), which cannot be determined as accurately as Chandrasekhar's, due to uncertainties in the understanding of extremely dense matter. Above the Oppenheimer-Volkoff threshold mass, the degenerate neutrons cannot resist gravity and there is no escape from the final collapse to a black hole: the whole matter of the object will collapse to a singularity. A black hole is such a dense object, that its escape velocity exceeds the speed of light c, which is the maximum speed for the transmission of any information. In principle every mass can become a black hole if it is compressed strongly enough. If all the mass is inside a certain radius R_S around the object, no information can leave the so called event horizon. The radius of the event horizon is named after the astronomer Karl Schwarzschild and given by

$$R_\mathrm{S}(M) = \frac{2GM}{c^2} \approx 3 \text{ km} \cdot \frac{M}{M_\odot} \tag{3.1}$$

where $c = 2.9979 \cdot 10^8$ ms^{-1} is the speed of light, $G = 6.673 \cdot 10^{-11}$ m^3 kg^{-1} s^{-2} is the gravitational constant and $M_\odot = 1.989 \cdot 10^{30}$ kg is the mass of the sun. This simple picture of the escape velocity

is a bit misleading, because motion of photons and a classical particle, for which the escape velocity is defined, cannot compared. Karl Schwarzschild derived the radius of the event horizon by solving Einstein's field equations of general relativity (Einstein, 1916).
According to general relativity spacetime is curved in the presence of mass. The metric of flat spacetime in polar coordinates is given by

$$(ds)^2 = (c\,dt)^2 - (dr)^2 - (r\,d\theta)^2 - (r\,\sin\theta\,d\phi)^2 \tag{3.2}$$

Whereas, the Schwarzschild metric (Schwarzschild, 1916) describes the spacetime around a massive object

$$(ds)^2 = \left(c\,dt\sqrt{1-\frac{2GM}{Rc^2}}\right)^2 - \left(\frac{dr}{\sqrt{1-\frac{2GM}{Rc^2}}}\right)^2 - (r\,d\theta)^2 - (r\,\sin\theta\,d\phi)^2 \tag{3.3}$$

In Schwarzschild's metric it can be shown that a particle moving around a black hole feels the potential (Schutz, 1985)

$$V^2(r) = \left(1-\frac{2M}{r}\right)\left(1+\frac{L^2}{r^2}\right) \tag{3.4}$$

with the angular momentum L of the particle. Depending on the value of L the particle will fall into the black hole or is orbiting on a rather complicated orbit forever. The critical angular momentum $L_{\min}$ is the minimum angular momentum a particle must have to orbit the black hole. Schutz (1985) shows that $L_{\min} = \sqrt{3}McR_{\mathrm{S}}$, which yields a innermost stable circular orbit around a black hole of $R_{\mathrm{ISCO}} = 3R_{\mathrm{S}}$.

For rotating black holes this is not the right assumption. Particles which fall into the black hole, either accreted during the black holes life or the initial mass which collapsed to the hole, keep their angular momentum. Hence one expects the existence of rotating black holes. In the case of rotating black holes the metric of Schwarzschild is a inadequate description of spacetime. Kerr (1963) found a metric describing the spacetime around a spinning mass. The angular momentum of a spinning black hole can be described via the dimensionless Kerr parameter

$$a = \frac{cJ}{GM^2} \tag{3.5}$$

For a Schwarzschild black hole, $a = 0$, whereas a maximal rotating Kerr black hole has $a = 0.998$. Thorne (1974) showed that the upper limit for the Kerr parameter is 0.998 and not 1. As demonstrated by Bardeen et al. (1973), the cross-section of the capture by the black hole is bigger for photons with an angular momentum opposite to that of the black hole than for photons spinning in the direction of the hole. This effect prevents the black hole from a spinning-up to the value of $a = 1$. The frame dragging effect around rotating black holes forces the spacetime around the object to co-rotate with the central mass. This effect changes the behavior of the innermost stable orbit. The distance of the ISCO to the black hole is thereby decreasing with higher values of a. Around a maximal rotating black hole R_{ISCO} extends to the event horizon, so the observation of radiation from the innermost area of the accretion disk shows information about the spin of the black hole.

The above shows that black holes can be characterized by only two parameters, the mass M and the Kerr parameter a. (In addition one can assume an electric charge of the black hole, but in the electric neutral universe the charge of the black hole would attract opposite charges on a very short time scale. Astrophysical charged black holes are therefore not expected.)

Besides the stellar black holes described above, there is another type of supermassive black holes. In the core of Active Galaxy Nuclei (AGN) one expects a black hole with masses from $10^6 M_\odot$ up to $10^9 M_\odot$. Even the milky way has such an object in its center. Ghez et al. (2000) calculate the black hole's mass to $M = (4.8 \pm 0.3) \cdot 10^6 M_\odot$ by analyzing the orbits of stars in

the center of our galaxy. A similar mass is proposed by Genzel & Eckart (1999). The AGNs are expected to be the reason for the big amount of energy released by objects like quasars and radio galaxies.

3.2 X-ray Binaries

A large number of stars are part of a multiple system, in which two (or more) stars orbit around their common center of mass. Binaries consisting of stars can be observed in different ways. Visual binaries can be resolved by telescopes and the motion of both partners can be observed directly. If the binary cannot be resolved, there is still the chance to detect the nature of the system by analyzing the spectra. The orbital period and other parameters can be found due to periodic shifts of spectral lines caused by the Doppler effect. Objects of this class are called spectroscopic binaries. In the case of eclipsing binaries, the inclination angle of the system is in the order of 90° and thus there is a variation in the lightcurve of the system when one star eclipses the companion.
The description of stellar evolution above holds for single stars. In the case of a close binaries both components may influence each other and mass transfers may occur. X-ray binaries are formed when the more massive star ends his life in a supernova and a compact object (neutron star or black hole) is created (Iben, 1991). In the time of before the supernova the stars expands and is loosing its upper layers, when the core collapses. Primarily at this point there can be a huge mass transfer to the former smaller star, which is growing.

To determine the masses of the binary, one has to do spectroscopy as mentioned above. By measuring the shifts of the spectral lines the projected radial velocities of the object can be obtained. In the case of a small eccentric orbit, the Keplerian velocities can be assumed as constant and therefore the mass ratio can be calculated as

$$\frac{M_1}{M_2} = \frac{v_2}{v_1} = \frac{v_{\perp,2}}{v_{\perp,1}} \tag{3.6}$$

where $v_\perp = v \cdot \sin i$ is the projected radial velocity with the inclination angle i. The inclination angle is the problem in determining the sum of masses. It cannot be measured well, if the system is not eclipsing $i \approx 90°$ or is without any Doppler shift at $i \approx 0°$. With knowledge of the orbital period P of the system, and Kepler's third law

$$\frac{P^2}{a^3} = \frac{4\pi^2}{G(M_1 + M_2)} \tag{3.7}$$

one can show

$$M_1 + M_2 = \frac{P}{2\pi G} \cdot \frac{(v_{\perp,2} + v_{\perp,1})^3}{\sin^3 i} \tag{3.8}$$

In most cases it is difficult to determine all the values exactly. So many binary system have only a given mass range for both objects.
In close binary systems there can be mass exchange. By considering the effective gravitational potential in a rotating coordinate system, one can figure out the potential as a sum of the potential of the masses and a centrifugal potential (Frank et al., 1992, Eq. 4.5):

$$\Phi(\vec{r}) = -\frac{GM_1}{|\vec{r} - \vec{r_1}|} - \frac{GM_2}{|\vec{r} - \vec{r_2}|} - \frac{1}{2}(\vec{\omega} \times \vec{r})^2 \tag{3.9}$$

The five Lagrangian points, characterized by $d\Phi(\vec{r})/d\vec{r} = 0$, are points in this system where no forces act. The inner Lagrangian point L_1 between both masses defines the equipotential surface called Roche lobe. It is shaped like two connected drops. If matter from the one side crosses the Roche lobe it will be attracted by the other object.

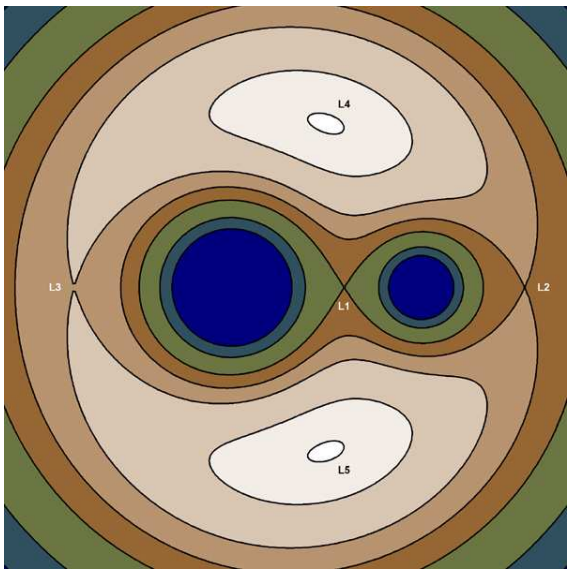

Figure 3.2: Visualization of the gravitational potenial $\Phi(\vec{r})$ of a binary system. The five Lagrangian points L_1 to L_5, where $d\Phi(\vec{r})/d\vec{r} = 0$, are shown in this figure. (source: `http://members.wri.com/jeffb/visualization/lagrange.shtml`

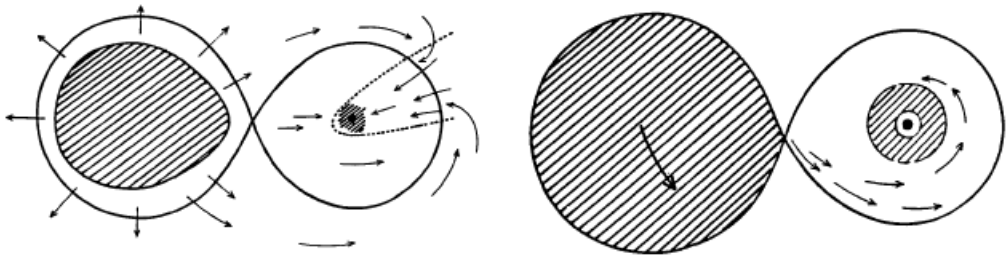

Figure 3.3: The mass transfer mechanisms of X-ray binaries via stellar wind accretion (left) and Roche-lobe overflow (right) (Oda, 1977)
.

The radiation of X-ray binaries in powered by the accretion of matter to the compact object (see Sect. 3.3). One distinguishes between two types of X-ray binaries in respect to the mechanism of accretion as illustrated in Fig. 3.3:

- A Low Mass X-ray Binary (LMXB) consists of a compact object (neutron star or black hole) and an old evolved star. The late-type star in its giant phase fills its Roche lobe. Matter can pass through the Lagrangian point L1 to the range of the collapsar. The conservation of angular momentum prevents the matter from falling directly onto the object. An accretion disk is formed.

- The other case is a High Mass X-ray Binary. A compact object is together with a young, massive star of O- or B-type, which shows strong stellar winds. The wind is focused to the black hole or neutron star. Due to the lack of angular momentum in the stellar wind the accretion disk is smaller than the disk of LMXBs or is missing completely (Iben et al., 1995).

3.3 Accretion Disks and Jets

The process of attracting matter into a strong gravitational potential in astrophysics is called accretion. The potential energy of the particles is released in this process. Due to conservation of angular momentum the particles attracted by the compact object may not fall directly into the potential sink. The best known model for this scenario is the thin accretion disk (Shakura & Sunyaev, 1973). The attracted gas flows into the disk of matter around the collapsar. After

entering the disk, the gas is moving on Keplerian orbits. The particles interact with each other and heat up due to friction effect. Viscosity transports the angular momentum outwards and the particles are forced to move to lower radii slowly. The disk terminates at the innermost stable circular orbit R_{ISCO}. If a particle in this orbit looses energy because of the above effects, it is doomed to fall beyond the event horizon of the black hole. The efficiency of accretion exceeds by far that of nuclear fusion in stars. A useful value to quantify the luminosity of accretion is the Eddington luminosity L_{Edd}. It is defined as the luminosity, which equals the gravitational pressure, assuming spherical symmetric accretion of ionized hydrogen. The gravitational force is calculated for the much heavier protons. The radiation pressure is primarily acting on the electrons with the much bigger Thompson cross section. Due to Coulomb coupling between both kinds of particles the forces act on the other particle as well. The gravitational force on protons is

$$F_G = \frac{FGm_p}{r^2} \tag{3.10}$$

The radiation force of the energy flux $S = L/4\pi r^2$ acting outwards on electrons is

$$F_R = \frac{\sigma_T S}{c} \tag{3.11}$$

The Eddington luminosity is the critical value of $F_R = F_G$. Above this luminosity accretion can no longer be maintained, the particles are pushed out of the gravitational sink. Thus the Eddington luminosity is

$$L_{\mathrm{Edd}} = \frac{4\pi GMm_p c}{\sigma_T} \approx 1.3 \cdot 10^{38} \mathrm{erg\,s^{-1}} \cdot \frac{M}{M_\odot} \tag{3.12}$$

The accretion onto black holes produces luminosities in the order of L_{Edd}. In Cygnus X-1 the optical OB-type companion has a mass loss rate in the range of $10^{-6} - 10^{-5} M_\odot \mathrm{yr}^{-1}$. If only a small fraction of the wind is attracted by the black hole (Frank et al. (1992) quote 0.1% a typical value for Cygnus X-1), it can reach the Eddington limit. To get a feeling of the enormous energy output of accretion, consider the energy source powering our planet and life. Nuclear fusion in the cores of common stars converts slightly less than 1% of the rest mass of each proton into energy. Accretion onto a Schwarzschild black hole releases 10% of the accreted mass. If the black hole is a maximum rotating Kerr black hole this increases up to $35\% - 40\%$ (Frank et al., 1992).

A phenomenon most probably directly linked to the existence of an accretion disk is the formation of a relativistic jet. Jets are collimated outflows of matter in two opposite directions. They are aligned perpendicular to the angular momentum of the accreting object or its accretion disk and are collimated over very long distances with small opening angles of only some few degrees. Jets are detected in the radio band in X-ray binaries and in many AGN. The length of a jet of an AGN can exceed the size of the host galaxy and extend to several kpc. The measurements at radio wavelengths show a strongly polarized radiation. It can be described by synchrotron radiation (see Sect. 3.4.4) in the magnetic field of the outer jet regions. Although they are well studied with radio telescopes their origin is not understood correctly yet. The nature of the ejected particles is just as unclear as the mechanisms of jet formation. The particle composition is is meant to be of ionized atoms and their electron, possibly in combination with a hot electron-positron plasma. Begelman et al. (1984) present a detailed discussion of possible jet formation mechanisms. Magnetohydrodynamical simulations therein show a connection between a rotating accretion disk or corona and the ejection of matter in perpendicular directions. A direct extraction of rotational energy of a Kerr black hole is possible (Blandford & Znajek, 1977).
The jet model of Markoff (2005) explains the whole X-ray and radio emission of black hole binaries with the existence of disk and jet. The model includes the radio observable synchrotron radiation from the outer jet. The base of the jet is in the place of the Comptonization corona provided by other models. In this area seed photons originating from synchrotron radiation are upscattered

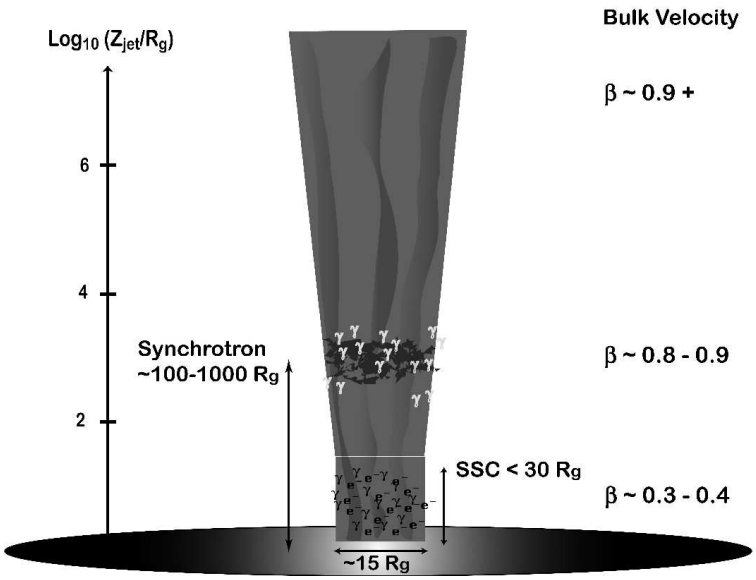

Figure 3.4: Sketch of the geometry of the jet model by Markoff (2005). There is thermal emission from the accretion disk, which is reprocessed in the base of the jet by Comptonization. Also synchrotron radiation of the jet itself undergoes the Comptonization process (Self-Synchrotron Comptonization). The outer regions of the jet are responsible for synchrotron radiation detected at radio wavelengths.

via synchrotron self-Comptonization (SSC) up to hard X-rays. It is possible that the base of the jet with its hot plasma and the Compton corona, favored by other models, describe the same phenomenon (Markoff et al., 2005).

3.4 X-rays and Radiation Processes

X-rays were discovered by W. C. Röntgen in 1895. While studying cathode rays, he noticed a fluorescent light on a screen behind a optical shielding, he used in his experiments. Röntgen obtained the first Nobel prize in 1901 for his discovery and in German the X-rays are called "Röntgenstrahlen". For technical use X-rays are commonly produced as bremsstrahlung from an electron beam stopped by a metallic anode. The maximum photon energy depends on the kinetic energy of the electrons and thus can be modulated by the accelerating voltage in the cathod ray tube. In the following section the radiative processes of a X-ray binary system are discussed. With the spectral shape of these emissions a lot of interesting physics can be done.

3.4.1 Black Body Radiation

In Sect. 3.3 the formation and physical conditions of an accretion disk are described. Due to friction and conversion of angular momentum of the particles orbiting the black hole the disk is heating up to very high temperatures. Hot surfaces, like stellar surfaces, in astrophysics are as a good approximation black body radiators. Rybicki & Lightman (1979, Eq. 1.51) describe the emission of electromagnetic radiation of a black body with the temperature T, known as Planck's law.

$$I(\nu, T) = \frac{2h\nu^3}{c^2} \frac{1}{e^{\frac{h\nu}{k_B T}} - 1} \tag{3.13}$$

where k_B = Boltzmann's constant and h = Planck's constant. Planck's law describes the emission of photons with $E = h\nu$ per solid angle and per frequency. The integral over Eq. 3.13 yields the luminosity of a black body at temperature T. Shakura & Sunyaev (1973) show for accretion disks

that the temperature profile of the disk is not constant. The temperature T depends on the radius R as follows

$$T(R) \propto R^{-3/4} \tag{3.14}$$

To obtain the total black body emission from an accretion disk one has to sum over all black body components at different temperatures. The disk is therefore called a multi-color disk (Mitsuda et al., 1984; Makishima et al., 1986).

3.4.2 Comptonization

The spectra of black hole binaries can be described as a broken powerlaw from soft to hard X-rays with an exponential cutoff at very high energies. This continuum cannot be described only with a black body component, as the emission of hard X-rays would require unphysical high temperatures in the accretion disk. The mechanism of Comptonization is believed to be responsible for this spectral shape. The process is based on Compton scattering. Compton scattering is the process of photons scattering on electrons at rest. Following the description of Rybicki & Lightman (1979) the photon energy after the scattering for an angle θ is

$$E' = \frac{E}{1 + \frac{E}{mc^2}(1 - \cos\theta)} \tag{3.15}$$

Expressed in wavelengths the process can be written as

$$\Delta\lambda = \lambda_\mathrm{c}(1 - \cos\theta) \quad \text{with the Compton wavelength } \lambda_\mathrm{c} = \frac{h}{mc} \tag{3.16}$$

If the photon energy is small, $E \ll m_\mathrm{e}c^2$, the energy change of the photon averaged over all angles θ is given by

$$\langle \Delta E \rangle = -\frac{E^2}{m_\mathrm{e}c^2} \tag{3.17}$$

If the electron is in motion one has to apply Lorentz transformations between the lab frame and the frame of rest. This complicates the integration over the angle θ. In Rybicki & Lightman (1979, Sect.7.2,7.3) the energy change of photons scattering with non-relativistic electrons with a Maxwellian distribution, coupled to the temperature T, is calculated as

$$\frac{\Delta E}{E} = \frac{4kT - E}{m_\mathrm{e}c^2} \tag{3.18}$$

If the thermal energy of the photons is high enough, the photons gain energy during this process. In the case of X-ray binaries one assumes a Comptonization corona around the object or the accretion disk. The origin of the corona is unclear. One possible scenario is given by magnetohydrodynamical instabilities in the accretion disk (Balbus & Hawley, 1998). Sunyaev & Titarchuk (1985), Sunyaev & Trümper (1979) show that Comptonization of seed photons from a black body disk produce powerlaw spectra with an exponential cutoff at about $E_0 \approx k_B T$. Comptonization is also thought to be responsible for upscattering photons up to γ-ray energies (McConnell et al., 2002)

3.4.3 The Iron Fluorescence Line

A very prominent feature of the spectra of X-ray binaries is the iron fluorescence line (Reynolds & Nowak, 2003; Miller, 2007). It is caused by the transition of an electron from the $2p$ orbital to the $1s$ orbital, which is also known as the Kα emission line. The former $1s$ electron is missing due to photo ionization with hard X-rays or a collision with a relativistic particle. The line energy of this transition is about 6.4 keV in neutral iron and increases slightly with higher ionized states.

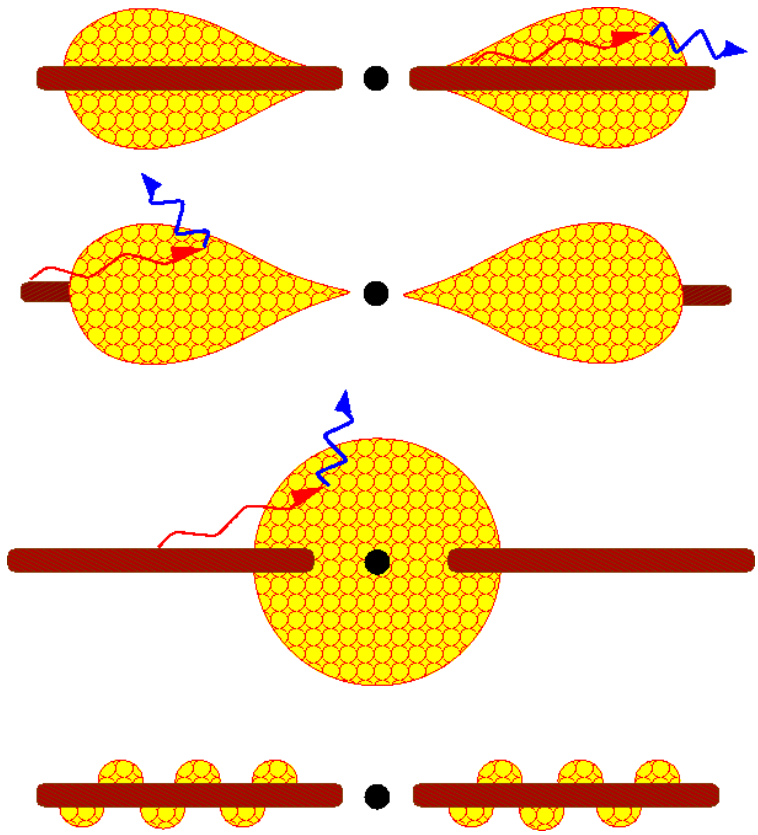

Figure 3.5: Different models for the position and shape of the Compton corona, which is colored in yellow. The accretion disk is shown in red. The most favored models are the two middle ones (Nowak, 2006, Fig. 1)

The area around the black hole is slightly enriched with iron as a consequence of the precedent supernova and the iron burning star, which formed the black hole. Furthermore iron has a large fluorescence yield, so processes involving iron become more dominant than others. The iron line is a great diagnostic tool for effects of general relativity and can be a hint for geometry in the immediate vicinity of a black hole. Its shape is influenced by the inclination and properties of the accretion disk, as well as by the spin and mass of the black hole itself. The iron line complex of Cyg X-1 was analyzed by Miller et al. (2002) and Hanke et al. (2009) with *Chandra* observations. Some effects are depicted in Fig. 3.6.

3.4.4 Synchrotron Radiation

The radiation of nonrelativistic charged particles accelerated by a magnetic field is commonly called cyclotron radiation. The emitting frequency in this case is the frequency of gyration in the magnetic field. If the particles have relativistic velocities the frequency spectrum changes and becomes harder. This radiation is called synchrotron radiation. The relativistic equation for the Lorentz force on a charged particle in a magnetic field B is

$$m\gamma\dot{\vec{v}} = \frac{q}{c}\vec{v} \times \vec{B} \tag{3.19}$$

Taking into account that only the perpendicular component of the velocity in respect to the magnetic field contributes to the radiation, one obtains

$$\dot{\vec{v_\perp}} = \frac{q}{\gamma mc}\vec{v_\perp} \times \vec{B} \text{ and } \dot{\vec{v_\parallel}} = 0 \tag{3.20}$$

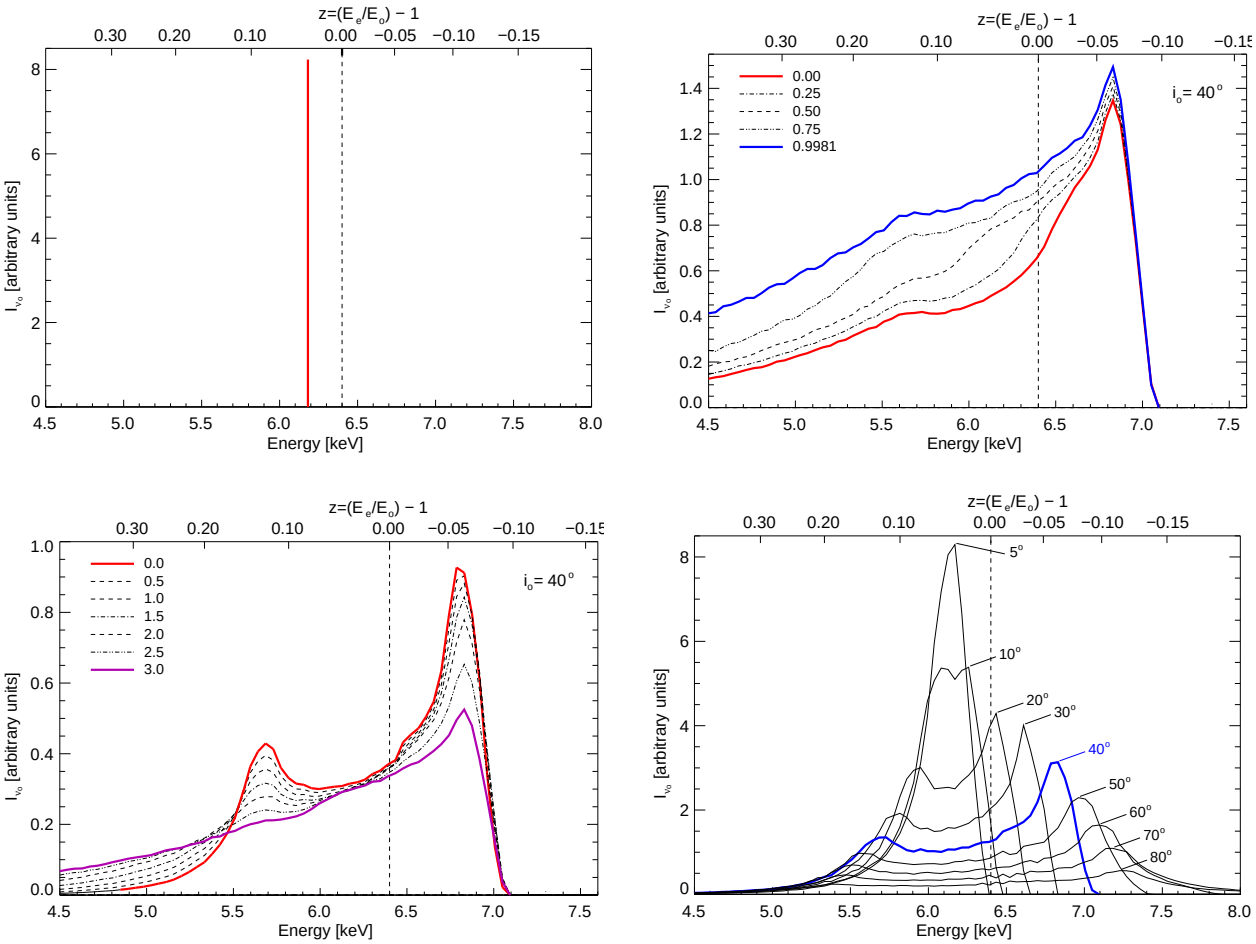

Figure 3.6: Different effects on the shape of the iron line. The top left plot shows, that the energy of the iron line can be lower than 6.4 keV due to gravitational redshift. In the top right plot the influence of the inclination angle of the accretion disk on the shape of the iron line is illustrated. Responsible for this influence are light bending effect and a Doppler shift in the strong gravitational field of the black hole. The bottom left figure demonstrates the shape of the iron line, if the disk has different emissivity profiles. The influence of the black hole spin on the line is shown in the bottom right plot. (J. Wilms, priv. comm.)

This yields a helical motion around the magnetic field lines. In the example of a relativistic jet, the direction of the jet is coaligned with the magnetic field.

Following the description of Rybicki & Lightman (1979, Chap. 6) the total emitted radiation of an isotropic distribution of particle velocities is

$$P = \frac{4}{3}\sigma_T c \beta^2 \gamma^2 \frac{B^2}{8\pi} \tag{3.21}$$

3.5 States of Black Hole Binaries

The behavior of galactic black hole binaries is generally very variable. Every black hole X-ray binary has its own typical fingerprint in the spectral and timing properties. But almost all of them are usually found in one of few states. These states are characterized by their spectral and timing properties. The different states are varying in overall X-ray luminosity, the hardness ratio of soft and hard X-rays and the strength of radio emission. The powerlaw describing the spectral shape shows different photon indices in different states. And at last the timing properties of the system

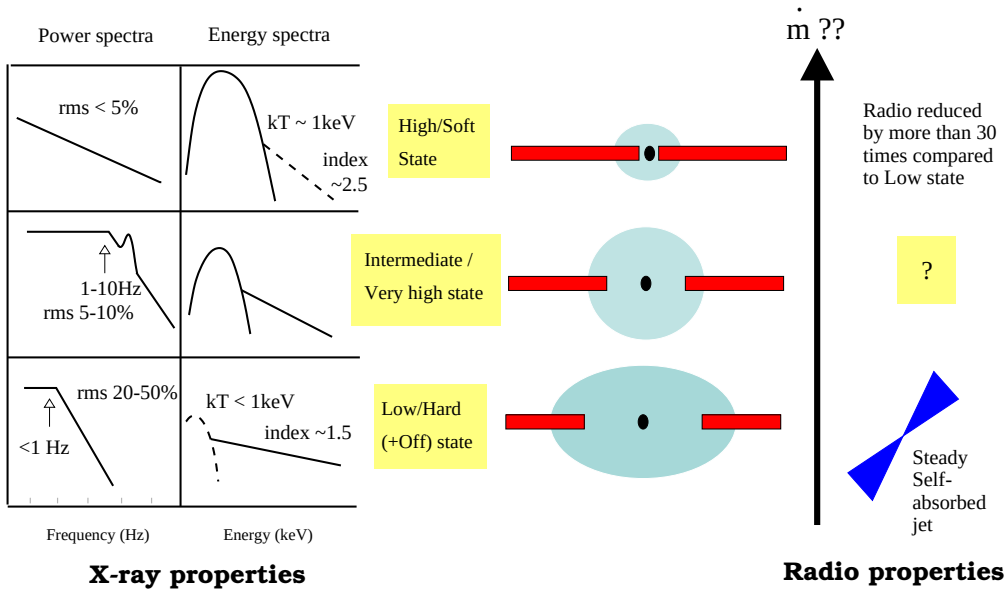

Figure 3.7: Overview of the most important states of microquasars. The states are defined by the shapes of their power spectra and energy spectra. A possible geometry of the system is shown, whereupon the accretion disk is red and the corona is colored in blue. The existence of a radio-emitting jet is indicated (Fender, 2002, Fig. 4).

changes completely when a state transition occurs. In the following the most important states are described and an overview is shown in Fig. 3.7.

In Fig. 3.8 the so called q-diagram is shown. There seems to be a typical track, most BHBs walk through. The diagram is named after the shape of the track, which look like the capital letter q. Many BHBs show state transitions in the order described in this figure. McClintock & Remillard (2003) gives an advanced summary on various black hole binaries. The q-diagram is a hardness intensity diagram. Most black hole binaries start in the bottom right corner with their movement. In this low/hard state the luminosity of the system is rather weak. The inner radius of the accretion disk is large compared to all other states and at radio wavelength a jet is observed. The dard spectrum is explained by Comptonization in a corona in vicinity of the weak thermal disk (Malzac, 2007). The power spectrum shows high variability, which is modeled best with broad noise components. This is the state Cygnus X-1 is usually found in as a persistent source. Transient sources become visible in this state, after they were inactive for a certain time.

When the transition starts, the X-ray luminosity increases and the spectrum becomes softer. The contribution of thermal disk radiation increases. The inner disk radius moves towards the innermost stable orbit and the characteristic frequencies in the power spectrum are at higher values. Radio observations of sources in this state show highly relativistic jets. When the spectral becomes more softer, the soft intermediate state is entered. The jet is no longer detected and the spectrum is dominated by the thermal disk. The rms variability of the source is much lower than in the other states and can be described with a single power law component (Churazov et al., 2001). The total luminosity of some sources reaches the Eddington limit when entering this state. The q-track is finished, when the soft state is left and the spectrum gets harder again, the luminosity is decreasing, because the inner disk radius moves out. The overall contribution of hard X-ray photons is higher and when the spectrum is near the hard state again, there are again detections of the jet. Cygnus X-1 is different in its movement through the states, as it changes its state always on the upper branch of the q-diagram (see Belloni, 2005, for further information about the q-track).

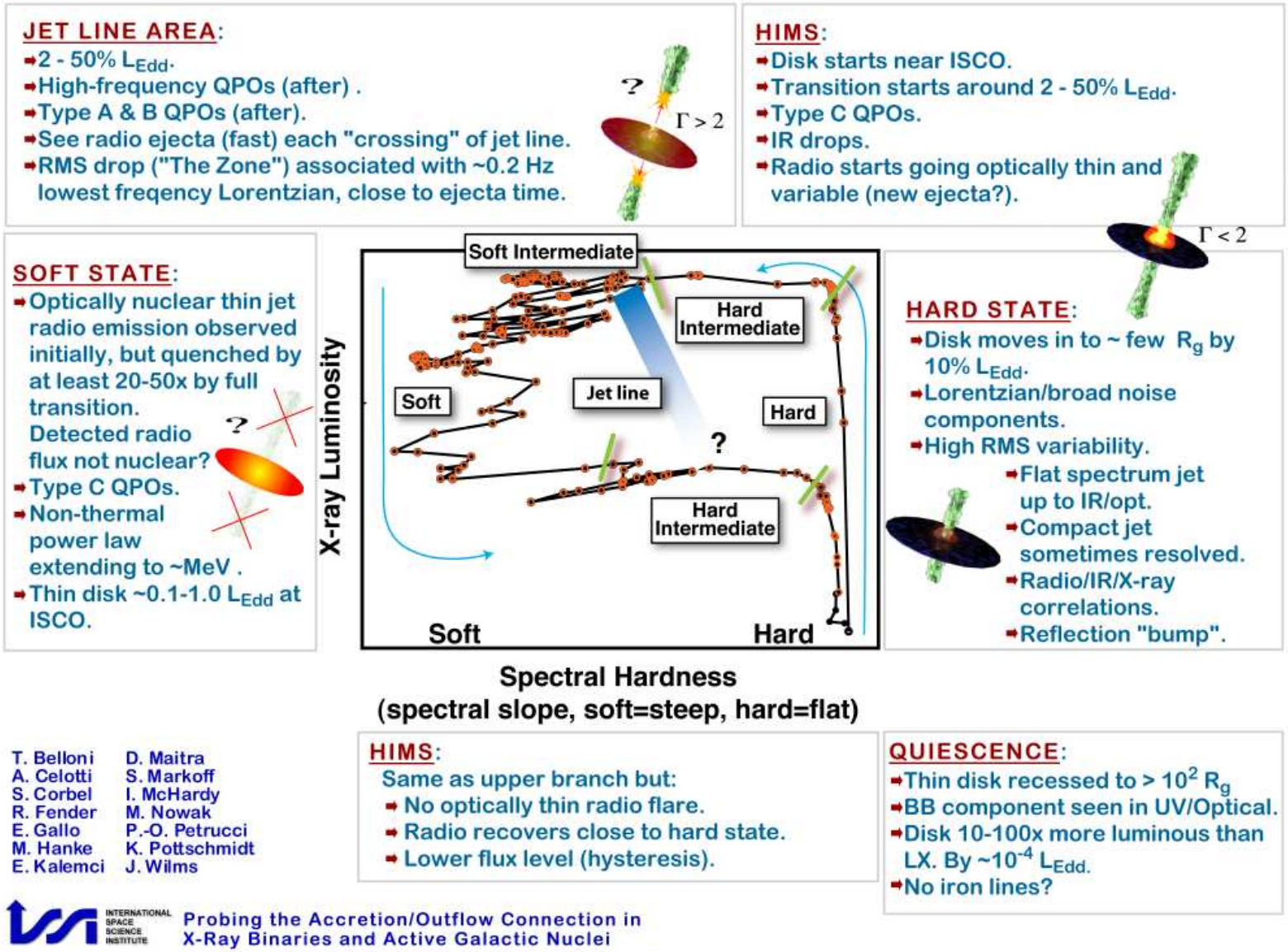

Figure 3.8: Detailed overview of the properties of the states of black hole binaries. The hardness intensity diagram indicates the typical sequence in which state transitions occur. Due to its shape it is called q-diagram. (Picture courtesy of International Space Science Institute (ISSI), see `http://www.sternwarte.uni-erlangen.de/proaccretion/`).

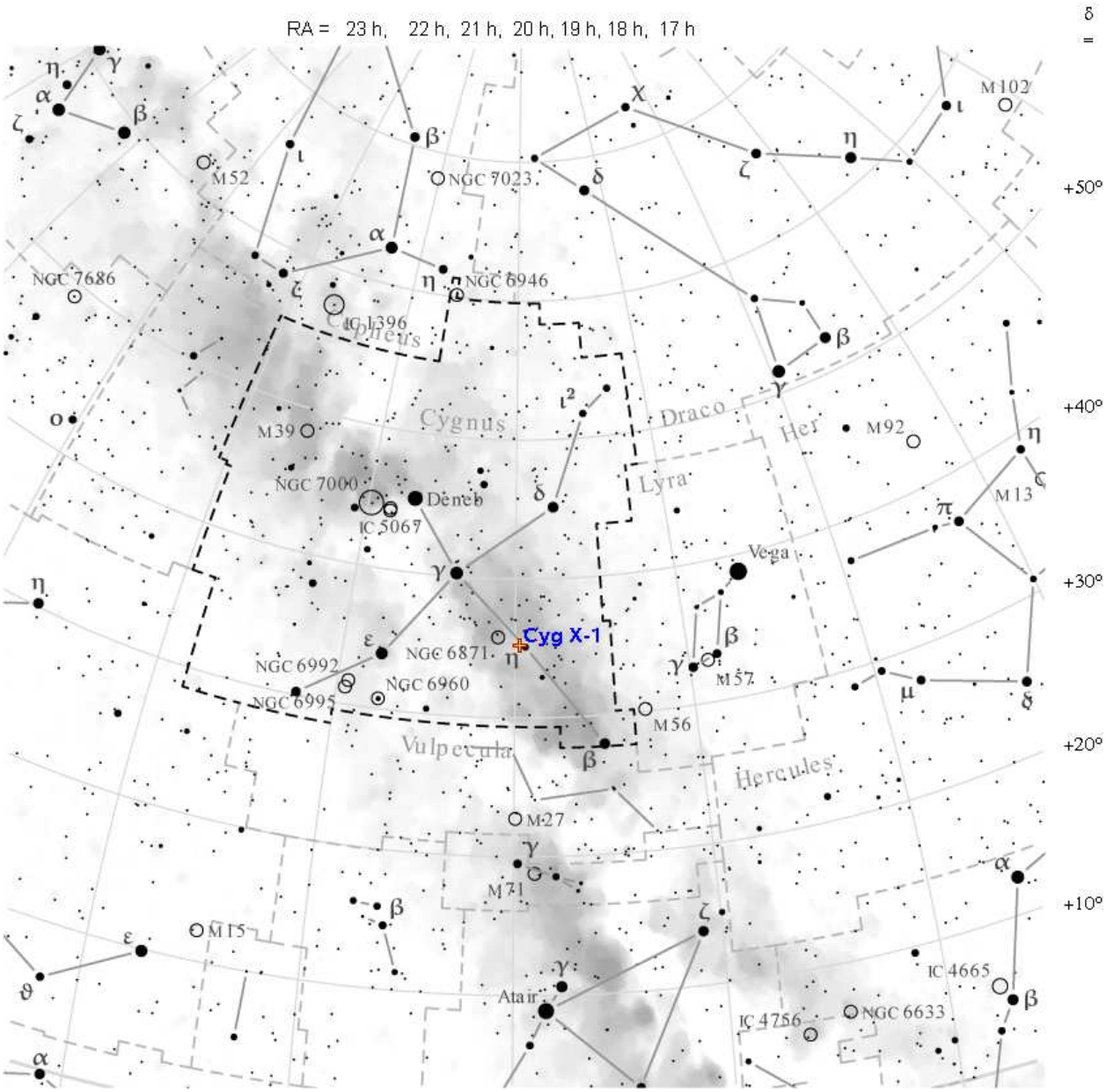

Figure 3.9: The constellation Cygnus with the position of Cyg X-1 (Hanke, 2007, Fig. 1.7)

3.6 Cygnus X-1 and HDE 226868

3.6.1 The Binary System

Cygnus X-1 (Cyg X-1) is one of the brightest X-ray sources in the sky and was discovered in 1964 (Bowyer et al., 1965). Its position on the sky is shown in figure 3.9. In 1971 a nearby radio flare was detected (Hjellming & Wade, 1971) and simultaneously a change in the spectrum of the X-ray source was detected. Its position was determined accurately and coincided with the OB-type star HDE 226868. Measurement of the radial velocity of HDE 226868 by Webster & Murdin (1972) confirmed the binary behavior of the system. The mass estimations for HDE 226868 and the compact companion spread over a quite wide range. Gies & Bolton (1986) with $M_\star \approx 33 \pm 9 M_\odot$ and Ziółkowski (2005) with $M_\star \approx 40 \pm 5 M_\odot$ obtained very high masses for HDE 226868 and corresponding higher masses for the compact object using non standard methods. Herrero et al. (1995) used unified models including the strong stellar wind. They report the most plausible mass

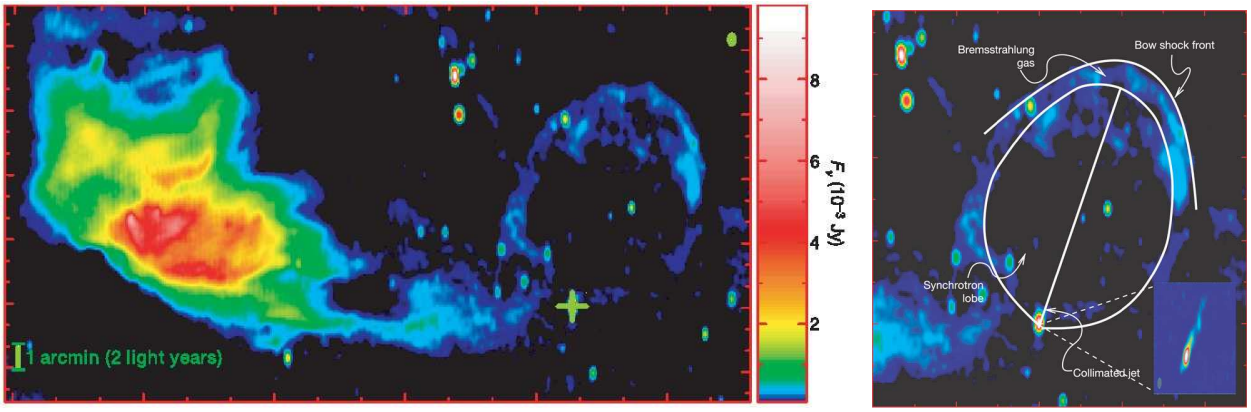

Figure 3.10: The region around Cyg X-1, observed at 1.4 GHz radio flux (left). The position of the X-ray source is marked with the green cross. The bright structure to the left is the H II emission nebula Sh2-101. The picture on the right shows a detailed view of the ring structure and its origin. A relativistic jet inflates a synchrotron-emitting lobe, which expands interacting with the interstellar medium, thus the shock-compressed gas emits bremsstrahlung (Gallo et al., 2005).

estimation of $M_\star = 17.8 M_\odot$ and $M_\mathrm{X} = 10 M_\odot$. All mass calculations for the compact object of Cyg X-1 exceed the Oppenheimer-Volkoff limit. Therefore a neutron star could be excluded and Cyg X-1 was the first galactic black hole candidate detected. HDE 226868 almost fills its Roche-lobe, but nevertheless wind accretion is dominating the accretion onto the compact object. The X-ray activity is persistent. Thus Cygnus X-1 is of three detected HMXBs with a black hole as compact object up to now. (Remillard & McClintock, 2006) classify Cyg X-1, LMC X-1 and LMC X-3 as HMXBs. There is also evidence for a relativistic jet in Cyg X-1. Radio emission from the source can be detected and is explained by synchrotron radiation of the jet. Figure 3.10 shows a picture of the region around Cyg X-1 at 1.4 GHz.

This source is one of the best studied X-ray binaries, but it shows a deviation from the usual behavior of black hole binaries. It does not follow the whole q-diagram (shown in Fig. 3.8). The state transitions of Cyg X-1 from hard to soft state and vice versa seem to proceed in the upper branch of the diagram only. A summary of the most important parameters of the binary is shown in table 3.6.1.

3.6.2 Orbital period

As this work concentrates on timing analysis on short timescales this paragraph provides a brief discussion of low-frequency variations in the lightcurves of Cyg X-1, which are not an essential part of the timing computations described below in Chap. 4.2. The most prominent frequency of a lightcurve of a binary is the Keplerian frequency. One expects a variability in the timescale of the orbital period P_orb of the system. A precise determination of the orbital period was performed by Brocksopp et al. (1999b). The measured radial velocities are shown in Fig. 3.11. The orbital period for Cyg X-1 is about 5.6 days.

X-ray and radio lightcurves of the binary are modulated with this period. The X-ray flux of the compact object is minimal, when it is in superior conjunction, which is defined as orbital phase zero. At this point the black hole is behind the optical companion. Since the inclination angle $i = 35°$ there is no eclipse in this system. The radiation has to cross a large fraction of the dense stellar wind of HDE 226868 and the radiation is partially absorbed or scattered, when the phase is near phase zero. Hanke et al. (2009) use observations at the superior conjunction to study the mechanism of the accretion of the focused wind in Cygnus X-1 and analyse the components of the wind spectroscopically. An interesting point is the modulation of the radio emission. The source of synchrotron radiation is meant for be further afar of the black hole. The mean frequency

Table 3.1: System Parameters of Cygnus X-1 / HDE 226868

Parameter	Cyg X-1	System	HDE 226868	Reference
Spectral type			O9.7 Iab	Walborn (1973)
Distance (kpc)		2.5		Ninkov et al. (1987)
Luminosity ($L_\odot$)	10^4		$10^{5.4}$	Herrero et al. (1995), Liang & Nolan (1984)
Luminosity ($erg\,s^{-1}$)	4×10^{37}		10^{39}	Herrero et al. (1995), Liang & Nolan (1984)
Inclination (°)		35		Ninkov et al. (1987)
Orbital period (d)		5.59974		Gies et al. (2003)
Major axis ($R_\odot$)	26.3		14.6	see discussion by Nowak et al. (1999a)
Mass ($M_\odot$)	10		18	see discussion by Nowak et al. (1999a)
Radius ($R_S/1\,km$ / $R_\odot$)	30		17	Herrero et al. (1995)
Separation ($R_\odot$)		41		see discussion by Nowak et al. (1999a)
Mass loss rate ($M_\odot$ / a)		3×10^{-6}		Herrero et al. (1995)

of emission decreases with the distance from the jet base. The modulation of X-ray flux can be found in the radio lightcurves, too, but the amplitude decreases with the wavelength. The lower the radio frequency is, the longer it takes until its flux gets minimal after the X-ray minimum, indicating the point of phase zero. The biggest delay can be found in the 2.25 GHz band with a phase lag of 30% of the orbit phase (Pooley et al., 1999). These phase lags can be explained by non-relativistic velocities of particles in the jet in combination with free-free absorptions in the focused wind of HDE 226868 (Szostek & Zdziarski, 2007). The modulation of the X-ray flux and three radio lightcurves is shown in Fig. 3.12.

3.6.3 Superorbital periods

In addition to the low frequency modulation caused by the orbital movement of the binary system, there are detections of variations on even longer timescales in the emission of Cygnus X-1. In data taken between 1969 and 1980 with the X-ray satellites *Vela 5b* and *Ariel 5*, Priedhorsky et al. (1983) revealed the evidence for a period of 294 ± 4 days. It was the first modulation found in Cygnus X-1 data. It was found only in data of these two satellites and several tests were performed afterwards to figure out if this feature was a source incident (Lachowicz et al., 2006, Appendix A). The results were confirmed and a similar period of ∼ 293 days was found in radio data at 15 GHz. Up to now there are no generally accepted interpretations of this modulation, which was not detected steadily from its discovery to this day. Another frequency was detected continuously in all data since 1976. The modulation has a period of 150 days and was investigated with *RXTE* observations by Benlloch et al. (2004) and confirmed as stable by Lachowicz et al. (2006) in X-ray and radio data (see Fig 3.13). The common explanation for this superorbital period is the existence of a precessing accretion disk. Precession is caused by a tilt angle δ of the disk with respect to the orbital plane. If the orbital period P_{orb} and the precession period P_p are known, one can calculate

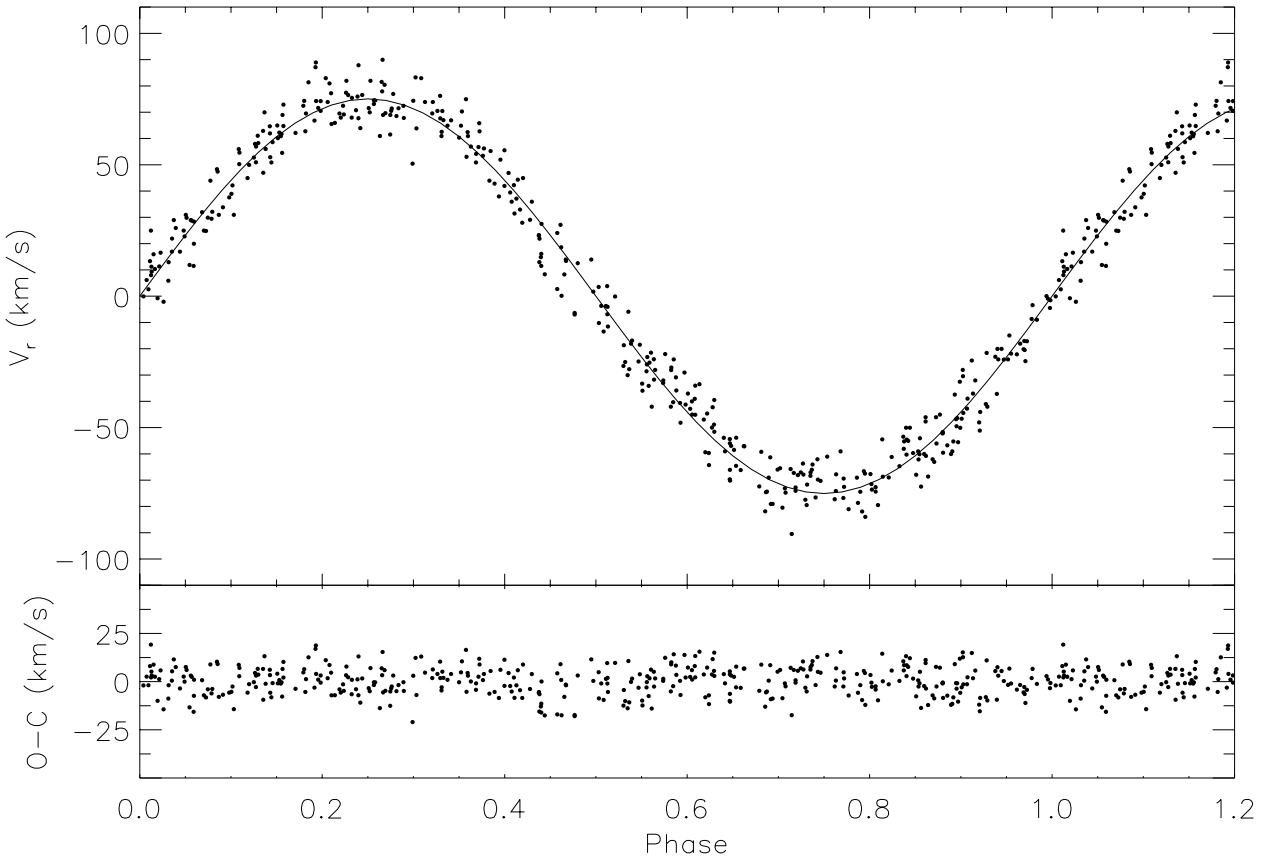

Figure 3.11: Radial velocity measurements of HDE 226868 plotted against the orbital phase. The solid curve represents the fitted theoretical model. In the bottom panel the deviations in the velocity from the best fit model are shown.(Brocksopp et al., 1999a)

a value for the angle δ using (Larwood, 1998, Eq. (4))

$$\frac{P_{\rm orb}}{P_p} = \frac{3}{7}\mu \left(\frac{1}{1+\mu}\right)^{1/2} \left(\frac{R_o}{a}\right)^{3/2} \cos\delta \tag{3.22}$$

where μ is the mass ratio between companion and the compact object, a is the orbital separation and R_o is the outer disk radius. The outer radius R_o can be written as a fraction of the Roche radius R_R, such that $R_o = \beta\, R_R$. This yields

$$\frac{P_o rb}{P_p} = \frac{3}{7}\beta_P^{3/2} \frac{\mu R^{3/2}}{\sqrt{1+\mu}} \cos\delta \tag{3.23}$$

The quantities R and $\beta_{\rm P}$, which is called Paczyński's radius, can be written as functions of μ :

$$R \simeq (\mu) = \frac{0.49}{0.6 + \mu^{2/3}\,\ln(1+\mu^{-1/3})} \text{and} \beta_P(\mu) = \frac{1.4}{1 + [\ln(1.8\mu)]^{0.24}} \tag{3.24}$$

Hence the knowledge of the mass ratio μ besides P and P_P yields a good approximation for the tilt angle δ. A discussion of these functions and their derivations can be found in Larwood (1998) in more detail. Using equation 3.22 and the ~ 150 days period Brocksopp et al. (1999a) approximate $\delta \approx 37^\circ$ for Cygnus X-1, shown in Fig. 3.14.

3.7 Short-term Variability of accreting BHB

In contrast to the low frequency variations shown in the last section (3.6.2, 3.6.3), there is a variability in the X-ray flux of BHBs with periods in the order of seconds and milliseconds, where this

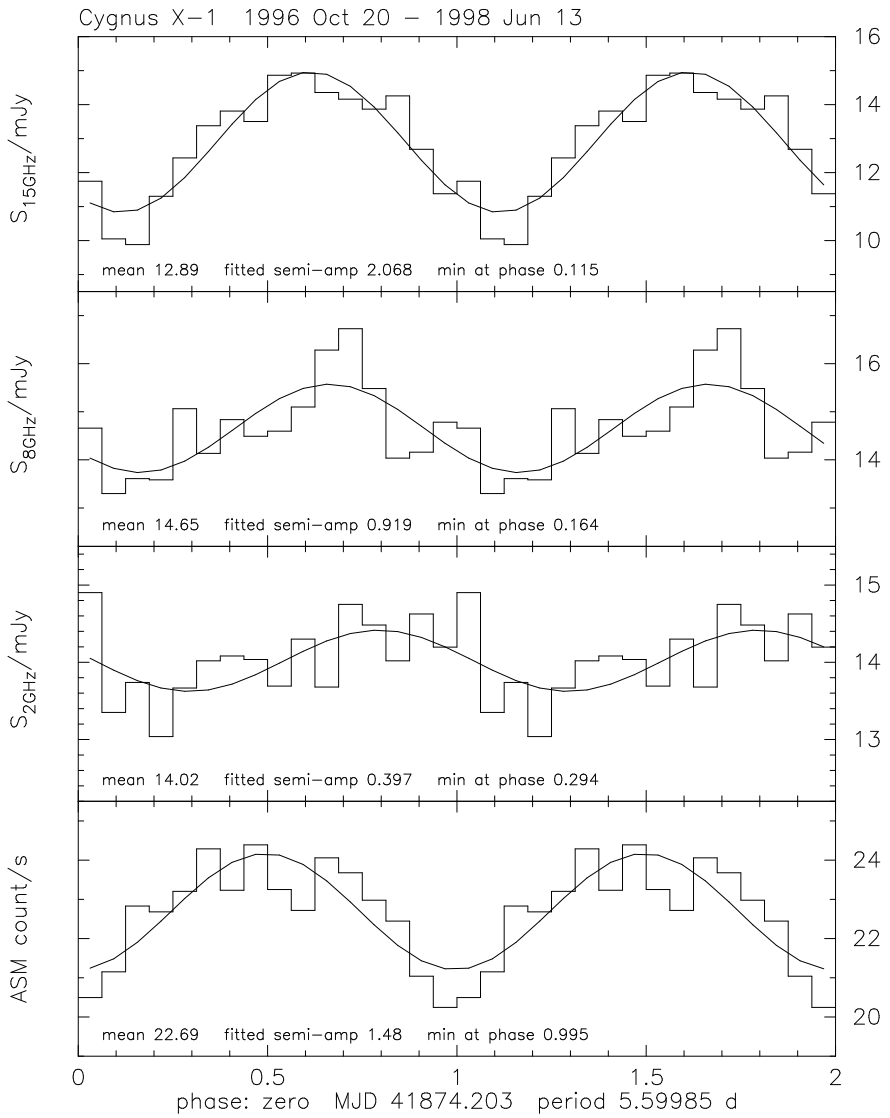

Figure 3.12: Orbital modulation of measured fluxes in different regions of the electromagnetic spectrum. The upper three panels show the radio flux, which was measured at 15, 8.3 and 2.25 GHz, the bottom panel shows the X-ray countrate of the ASM instrument in the 2–12 keV band. The plots indicate an overall decrease of the orbital modulation towards lower frequencies. There is also a phase shift indicated with decreasing photon energy. (Pooley et al., 1999, Fig. 2)

work concentrates on. The possible causes for this high frequency oscillations and the techniques of analysing them are presented here.

The main goal of this work is to analyze the short-term variability of Cyg X-1. In Sec. 3.6 the low frequency periods of Cygnus X-1 were discussed. The variability presented here occurs on time scales of seconds and milliseconds and therefore they are produced in smaller spaces. The only part of the binary system coming into consideration for this high frequencies is the vicinity of the black hole. Nowak & Lehr (1998) describe the characteristic frequencies of modulations in a this accretion disk, which are most likely the origin of high frequency variability in X-ray flux. The accretion disk can be assumed to lie in the equatorial plane of the black hole. The equatorial plane is perpendicular to the angular momentum of the compact object. The frequencies and oscillations in the disk only depend on the mass of the black hole and its angular momentum. In the following four frequencies are introduced. They are the most plausible frequencies originating from a thin

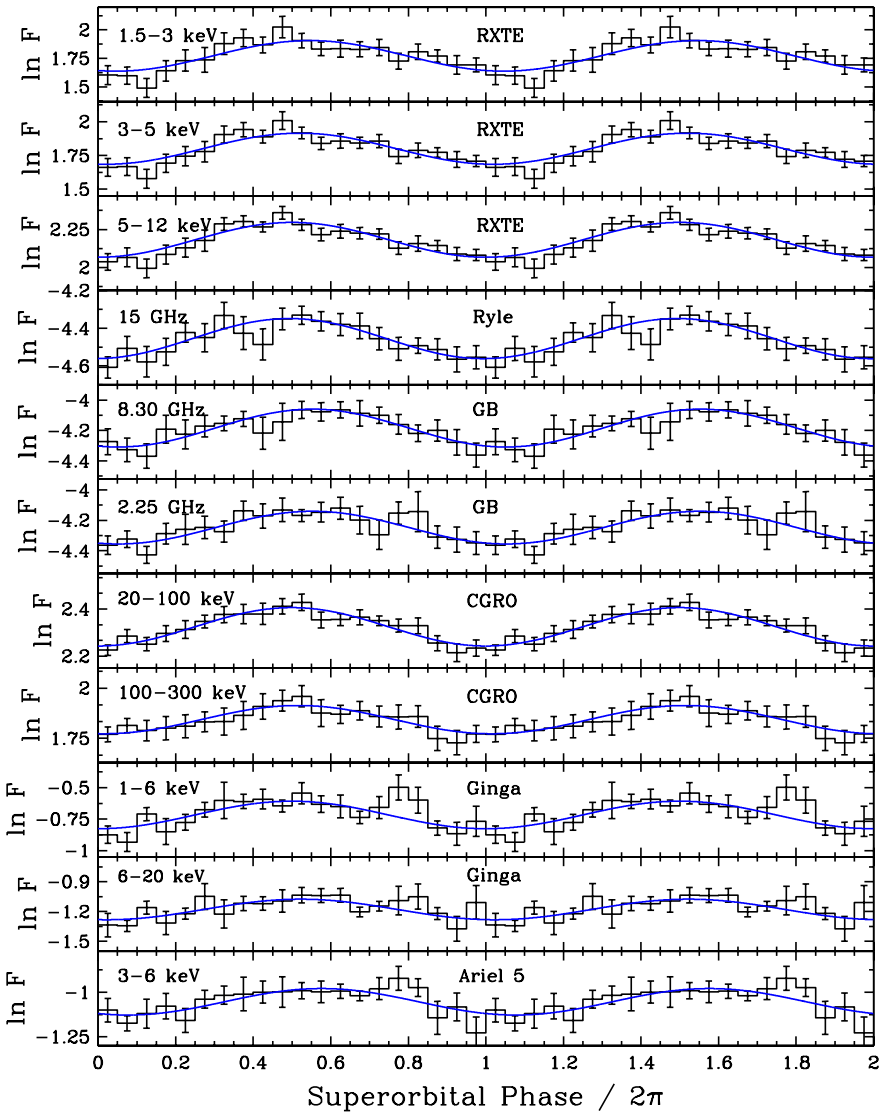

Figure 3.13: Superorbital modulation, which illustrates the modulation in all measured wavebands wiith different instruments. The amplitude of the modulation in the X-ray regime depends slightly on the energy and is highest at hardest photon energies. (Lachowicz et al., 2006, Fig. 7)

accretion disk around a black hole with its curved spacetime due to effects of General Relativity. In the formulas the distances r are given in dimensionless multiples of the gravitational radius

$$R_G = \frac{GM}{c^2} \tag{3.25}$$

and the angular momentum J of the black hole (Sec. 3.1) is described via the Kerr parameter a:

$$a = \frac{cJ}{GM^2} \tag{3.26}$$

All frequencies are those observed at infinity, that is far away from the black hole:

- One fundamental frequency is the Keplerian frequency, with that a particle in the accretion disk moves around the black hole. A modulation in X-ray flux with a period corresponding to the Keplerian frequency describes the orbital movement of an emitting area in the disk. The Keplerian frequency is given by:

$$f_k(R) = \frac{1}{R^{3/2} + a} \cdot \frac{c^3}{2\pi GM} \tag{3.27}$$

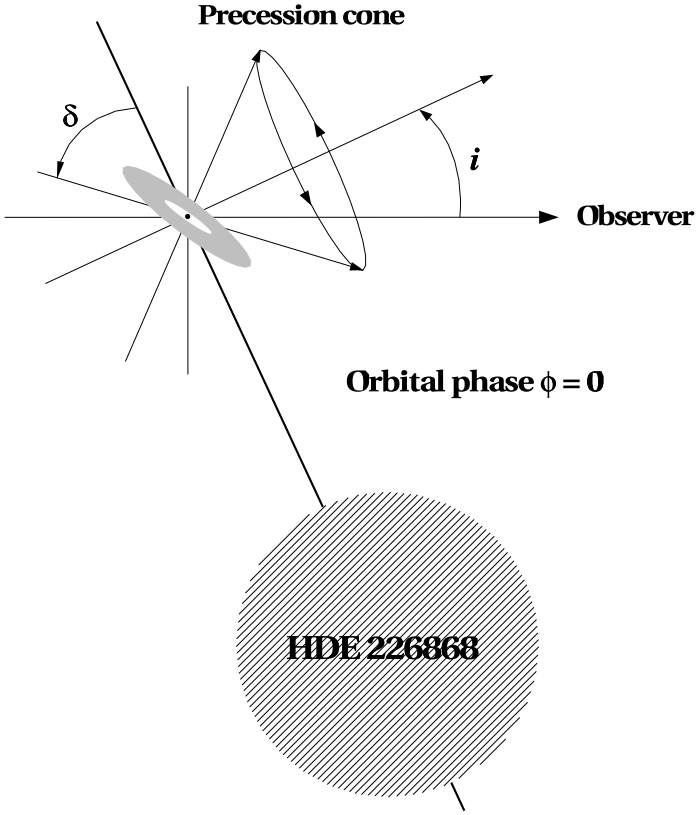

Figure 3.14: Schematic view of the system geometry of Cygnus X-1 / HDE 226868. i is the inclination angle, as seen from Earth and δ is the tilt angle between the orbital plane of the system and the disk. Precession caused by the tilted disk is meant to be responsible for the superorbital modulation of the emission. (Lachowicz et al., 2006, Fig. 9)

At the innermost stable circular orbit at $R_{\mathrm{ISCO}} = 6$ of a Schwarzschild black hole like Cyg X-1 this yields $f_{\mathrm{k}}(R_{\mathrm{ISCO}}) \approx 220\,\mathrm{Hz}$. The radius R_{ISCO} decreases with increasing a and reaches the Schwarzschild radius $R_{\mathrm{S}} = 2$ in the case of a maximal rotating Kerr black hole. For a black hole of this type the maximal Keplerian frequency is $f_k(\mathrm{ISCO}) \approx 520\mathrm{Hz}$.

- Another frequency is the radial epicyclic frequency. It describes the oscillation of a particle on a circular orbit about this orbit in radial direction, if it is perturbed. This frequency depends on the Keplerian frequency pertaining to the orbit oscillating about as follows:

$$f_r^2(R) = f_k^2(R) \cdot \left(1 - \frac{6}{R} + \frac{8a}{R^{3/2}} - \frac{3a^2}{R^2}\right) \tag{3.28}$$

  This frequency is zero at the innermost orbit. For a Schwarzschild black hole with $M = 10M\odot$ it reaches a maximum at $R = 8$, which is $\sim 71\mathrm{Hz}$.

- Just as the radial epicyclic frequency differs from the Keplerian frequency, so does the vertical epicyclic frequency, if the black hole has a spin $a \neq 0$. It is caused by a vertical perturbation of a particle on a circular orbit. It is given by:

$$f_\perp^2(R) = f_k^2(R) \cdot \left(1 - \frac{4a}{R^{3/2}} + \frac{3a^2}{R^2}\right) \tag{3.29}$$

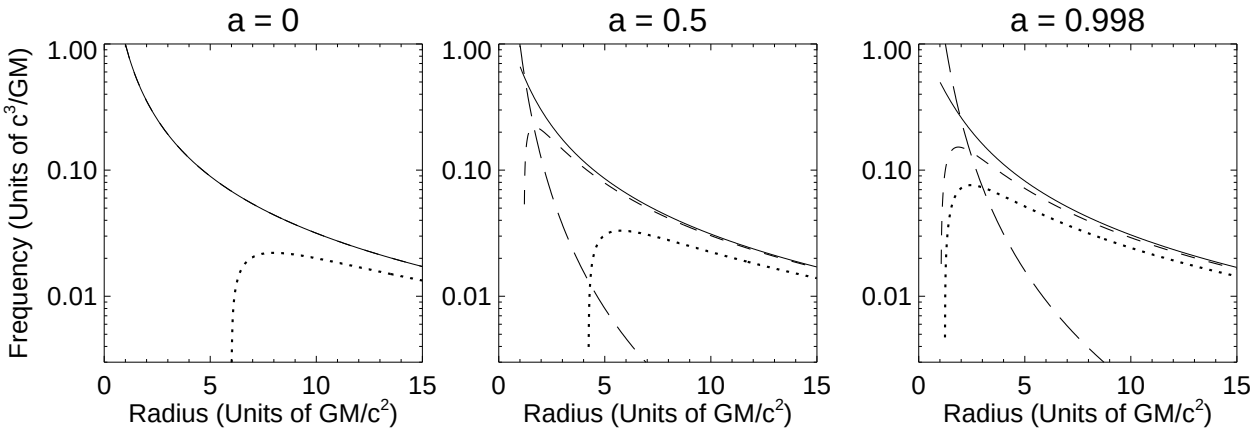

Figure 3.15: Overview of the most important frequencies, which can be observed in an accretion disk. The frequencies are calculated for different values of the angular momentum a. The radius is given in units of the gravitational radius and the frequencies are normalized to $c^3/2\pi GM$). The solid line is the Keplerian frequency $f_{\rm k}$, the dotted line is the radial epicyclic frequency $f_{\rm r}$ and the dashed line is the vertical epicyclic frequency $f_{\perp}$. The Lense-Thirring frequency $f_{\rm LT}$ is plotted with a long dashed line (Nowak & Lehr, 1998, Fig. 3)

.

- The final gravitational frequency in General Relativity is caused by the Lense-Thirring precession. The precession is caused by frame dragging effects around a rotating black hole, if the disk is tilted against the equatorial plane. The Lense-Thirring frequency is given by:

$$f_{LT}(R) = \frac{2a}{R^3} \cdot \frac{c^3}{2\pi GM} \tag{3.30}$$

An overview of the frequencies for black holes with different Kerr parameters a is shown in Fig. 3.15.

Chapter 4

Data Extraction and Computation

The X-ray data analyzed as main focus of this work were taken over a period of ten years. They are basically the result of a biweekly monitoring campaign of Cygnus X-1 with *RXTE*. The monitoring campaign is part of the satellite's core program, which consists of steady-going repetitive observations of different X-ray sources. Next to the HMXBs Cyg X-1, LMC X-1, LMC X-3 and GRS 1915+105, there are observations of LMXBs, AGN, different kind of pulsars and other celestial objects visible in X-rays part of this program. Besides the pointed observations originating from the core program, *RXTE* is able to monitor the X-ray sky with the ASM instrument (see Sec. 2.1.3). The ASM produces uninterrupted lightcurves of most of the sources to study the long-term behavior in X-ray radiation. If possible, radio data taken with the Ryle telescope (see Sec. 2.2) are added to the analysis to test the correlations between X-ray and radio flux. The Ryle telescope is an independent instrument with own research goals and therefore the additional radio data is not available at all interesting points of time. In the following sections the data obtained with these instruments are summarized. In Sec. 4.2 the programs and algorithms to perform the timing analysis are introduced, whose output are base for further characterization of Cyg X-1's behavior over ten years.

4.1 The Cyg X-1 Monitoring Campaign

The monitoring campaign of Cygnus X-1 with *RXTE* started in December 1997 with *RXTE*'s cycle AO3 and is ongoing in 2009, where it will possibly end with the shutdown of the satellite. The long-term goals of this campaign are to build-up a database of the accreting black hole binary Cygnus X-1 with its spectral and temporal evolution and to test various models of accretion and jet formation together with simultaneous radio observations. To achieve a uniform database of X-ray data is to measure the data in consistent data modes. Pottschmidt et al. (2003), Gleissner et al. (2004) and Wilms et al. (2007) used the campaign data for publications on the spectral and timing behavior of Cyg X-1.
One constraint to the quality and diversity of data taken with a spacecraft is the limited bandwidth made available to telemeter the measured data to Earth. In the case of *RXTE*, the spacecraft is moving so fast viewed from the ground, that a direct radio connection is impossible. *RXTE* is using NASA's Tracking and Data Relay Satellite System (TDRSS) system for telemetry. TDRSS consists of several satellites in geosynchronous orbits. Their function is to relay data from satellites and manned spacecrafts in lower orbits to ground stations. The limitation to ~ 20 kbits per second demands a strategy of converting the direct measurement of the detectors in the path of digitization to packets fitting this limit. In the technical appendix[1]of the *RXTE* satellite (XTE-Staff, 1995), one may find a detailed description of all available detector and data modes.

[1]Appendix F is public available at `http://heasarc.gsfc.nasa.gov/docs/xte/appendix_f.html`

4.1.1 Data

For all observations of the monitoring campaign of Cygnus X-1 the same data modes are chosen, except for those in the first year, where the time resolution of PCA differs from the latter. Among the standard modes `standard1b` and `standard2f/g` all observations were performed with `SB_250us_0_13_2s`, `SB_250us_14_35_2s`, `B_2ms_8B_0_35_Q` and `E_125us_64M_36_1s` for PCA and `E_8us_256_DX0F` for both HEXTE clusters. A detailed description of these modes can be found in XTE-Staff (1995). For the timing analysis investigated in this work only the PCA `E` and `B` modes were taken into account. Both provide a time resolution of 2^{-9}s $\simeq$ 2ms. Other PCA and HEXTE data are not analyzed here, but extracted from the raw data files for future analysis in the Cygnus X-1 workgroup at Remeis Observatory. The whole data extraction was done for the following *RXTE* observation IDs between April 1999 and September 2008:

- P40090
- P50110
- P60090
- P80110
- P80111 (not part of the campaign, but using the same data modes)
- P90104
- P90127 (not part of the campaign, but using the same data modes)
- P91096
- P92090
- P93120 (not part of the campaign, but using the same data modes)
- P93121

As result of the extractions the database for this work consists of $\sim$ 1200 lightcurves (see Sec. 4.2) and $\sim$ 1050 spectra (see Sec. 5.1).

Data from the ASM aboard *RXTE* is used, too. The lightcurves from many different sources are available via the ASM webpage without restrictions and are not proprietary. The field of view of the shadow cameras covers the whole sky in several steps. Every pointing to one direction is 90 seconds long. The image of the position sensitive detector is analyzed afterwards and the data analysis algorithm allocates the counts to a known source depending on the orientation of the instrument. The result is a lightcurve consisting of several 90 second dwells a day. An alternate lightcurve provided by the ASM team is averaged by days. Due to the statistical nature of the data analysis process the uncertainties of the lightcurve may be underestimated, but the ASM is the only instrument used in this work providing a quasi-continuous flux measurement of Cyg X-1.

Table 4.1: PCA energy bands of the monitoring campaign

E-Band	$\text{channel}_{\text{min}}$	$\text{channel}_{\text{max}}$	E_{min}	E_{max}	
1	0	10	< 2 keV	4.5 keV	starting at low threshold of PCA
2	11	13	4.5 keV	5.7 keV	
3	14	19	5.7 keV	8.2 keV	
4	20	30	8.2 keV	12.7 keV	
5	35	159	15.2 keV	69.6 keV	lowest possible limit due to event analyzer restrictions
6	160	214	69.6 keV	97.5 keV	channel is exclusively background dominated for Cyg X-1

4.2 Timing Analysis

This section describes the intended purpose of the software routines written for the timing analysis of the data. For straightforwardness they are called "*Timing Tools*" like their forerunner software suite developed by Pottschmidt (2002) in the Interactive Data Language (IDL[2]) . The X-ray group at Remeis observatory is working mainly with another programming language, so the tools were rewritten in that language. The spectral and timing analysis of Cygnus X-1 was performed with the Interactive Spectral Interpretation System (ISIS[3]) (Houck & Denicola, 2000). ISIS is based on the programming language S-Lang[4] and is primarily designed for to interpret high resolution X-ray spectra. Its programmability and the fully available S-Lang instruction set extended by some (astro)physical features makes it an adequate fundament for the timing tools. The following sections describe the functions and routines of the ISIS Timing Tools.

4.2.1 Preparation of Lightcurves

In order to perform the timing calculations, the lightcurves need to comply with some requirements. The Fourier calculations only result in meaningful data, if the lightcurve is evenly binned and is free of gaps. This stands for a lightcurve with the same bintime δt in every single bin. The PCA instrument aboard *RXTE* usually meets this claim and equally spaced lightcurves or single event data, depending on the data mode, can be extracted from the raw data archives. Nevertheless there are short SAA passages or short earth occultations possible, which are not treated as a trigger for a new lightcurve. In this cases a gap appears in the lightcurve, which needs to be cut out before the timing quantities can be calculated. Furthermore there is the possibility of changing PCU combinations during a running observation. If the results should be comparable to each other, only lightcurves with an unchanged number of activated PCUs can be taken into account. Therefore a lightcurve splits in two parts at the point of PCU switching.
As first step the lightcurves were extracted from *RXTE* raw data files in six energy bands chosen for this work. The energy bands are selected to be most comparable to former analyses of the Cyg X-1 monitoring campaign. (Pottschmidt et al., 2003, e.g) Lightcurves are extracted for the following energy ranges:
The requirement of gap free lightcurves must hold for all energy bands to make the computation of cross channel values possible. The cross power density (see Sec. 4.2.5) and the values derived from it are calculated from two lightcurves. Especially if one channel contains a gap, the corresponding time range needs to be cut out the other channels as well. After combining the extracted data from all channels to FITS files and searching them for gaps, the database for Cyg X-1 consists of

[2]for further information see http://www.ittvis.com
[3]http://space.mit.edu/CXC/ISIS/
[4]http://www.jedsoft.org/slang/

1212 6-channel lightcurve files. The remaining data after this preparation are 2482ksec ≈ 689.5h of input for the following calculation processes.

4.2.2 Power Spectral Density - PSD

The calculations of the Fourier quantities, as described in this chapter follow mainly van der Klis (1989), Vaughan & Nowak (1997), Nowak et al. (1999a) and Pottschmidt (2002). The Fourier transform is the base of Fourier analysis, where real functions can be described analytically by series of trigonometric functions. Technical applications are frequency analysis tools, like sound processing or lots of frequency transformations in science, like the application used here for the analysis of X-ray lightcurves. The basis of the computation of power spectral densities is this transformation. The Fourier transform, $F(\omega)$, can be described as a transformation of an integrable function $f : \mathbb{R} \to \mathbb{C}$ and is defined by

$$F(\omega) = \frac{1}{\sqrt{2\pi}} \int_{-\infty}^{\infty} f(t)\, e^{-i\omega t}\, dt \tag{4.1}$$

The Fourier transformed function $F(\omega)$ can be interpreted as a function defined on the frequency-domain, whereas $f(t)$ is defined on the time-domain. The original function $f(x)$ can be reconstructed from $F(\omega)$ by the inverse transform

$$f(t) = \frac{1}{\sqrt{2\pi}} \int_{-\infty}^{\infty} F(\omega) e^{i\omega t}\, d\omega \tag{4.2}$$

As the lightcurves of the X-ray satellite is a evenly spaced time series and no continuous mathematic function one can use the Discrete Fourier Transform (DFT). In the case of a time series, which consists of $a = a_1, \ldots, a_N$ with N elements and a bintime of Δt the integral is converted to a finite sum

$$A_k = \frac{1}{2\pi} \sum_{j=1}^{N} a_j e^{2\pi i j k/N} \tag{4.3}$$

with the corresponding inverse transformation. The values A_k depend on the Fourier frequencies

$$f_k = \frac{k}{N\Delta t} \tag{4.4}$$

The frequencies which can be obtained depend on the value of $j \in [-N/2, N/2]$. The time resolution Δt yields the maximum observable frequency $f_{\max} = 1/(2\Delta t)$, called the Nyquist frequency. The minimal frequency depends on the length of the time series $T = N\Delta t$ of the Fourier transformed segment: $f_{\min} = 1/(N\Delta t) = 1/T$.
The DFT is implemented in many programming languages via the Fast Fourier Transform (FFT) algorithm (see Press et al., 1992, and references therein). The FFT is a typical divide and conquer algorithm, which breaks down the problem of $2n$ parameters to two calculations of n and reconstructs the result afterwards. Therefore the implementation works fastest on a time series with a length of 2^n on a time scale of $\mathcal{O}(\mathcal{N} \log \mathcal{N})$. For that reason all lightcurves in this work are cut into segments of $2^{12} = 4096$, $2^{15} = 32768$ and $2^{18} = 262144$ bins. The three different segment sizes yield different thresholds for the lowest frequencies analyzable at constant Nyquist frequencies. Shorter segments are used for better statistics as described below.
Another characteristic of measured X-ray time series is counting noise. The noise usually consists of Poisson noise and hence the lightcurve can be split in a component of intrinsic source signal s_j and a noise component n_j

$$a_j = s_j + n_j \tag{4.5}$$

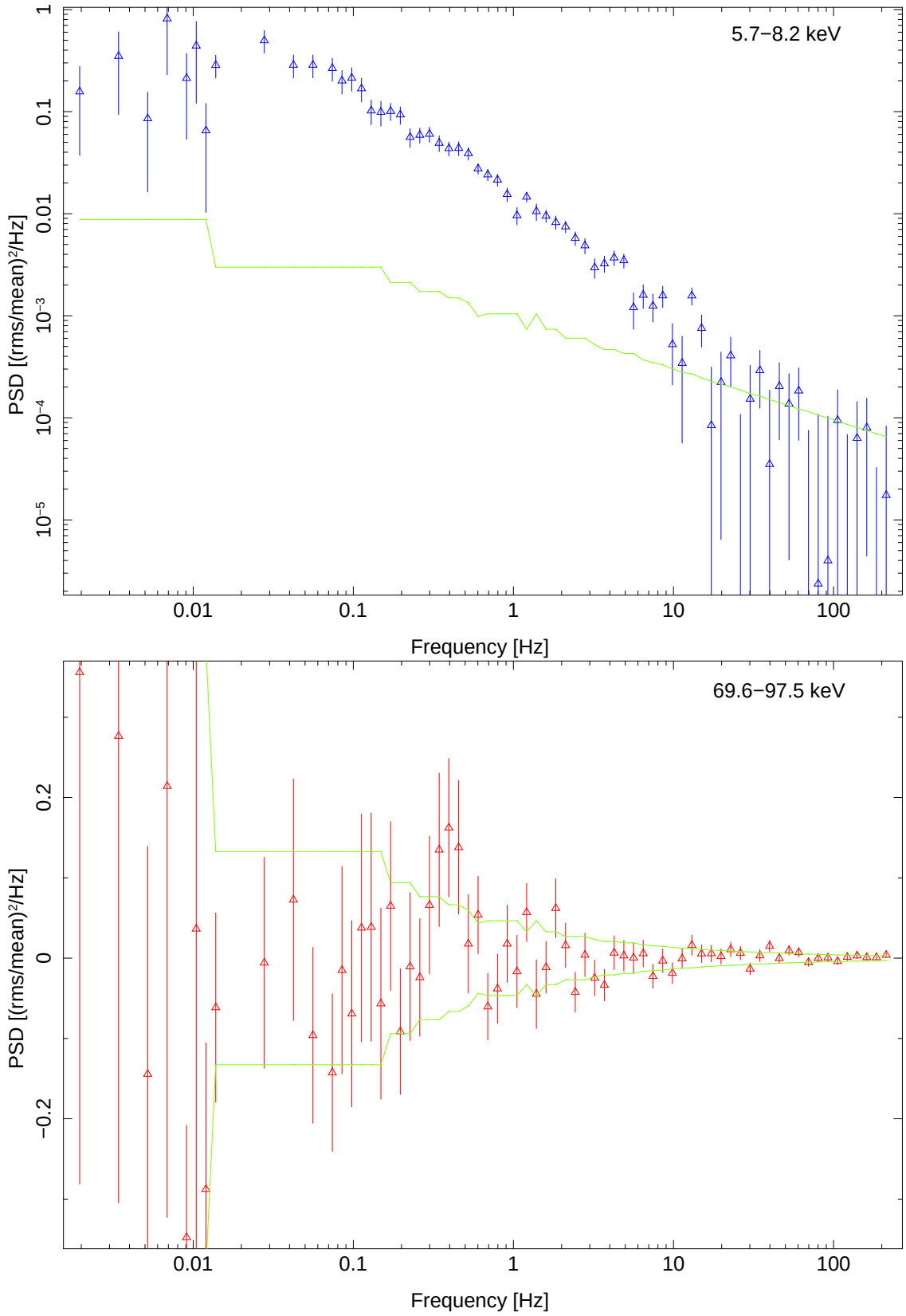

Figure 4.1: The calculated PSDs of a low/hard state observation of Cyg X-1 in energy bands 3 and 6. The corresponding energies are noted in the plots. The blue triangles in the upper panel are the noise-subtracted values with error bars after rebinning to a logarithmic grid. These PSDs are fitted for analysis. The green line marks the effective noise level. In the bottom panel the noise-subtracted PSD of the background dominated energy band is shown (red triangles). The values fluctuate below the effective noise level (again a green line) and are therefore not source characteristic.

This is also true for their Fourier transform

$$A_j = S_j + N_j \tag{4.6}$$

The power spectral density (PSD) is a real-value quantity constructed by multiplying the discrete Fourier transform of a lightcurve with its complex conjugated value. In other words the PSD is proportional to the squared absolute value of the DFT, a value which will be normalized later (Sect. 4.2.3)

$$P_j \propto A_j^* A_j = |A_j|^2 \tag{4.7}$$

After Parseval's theorem the PSD is directly related to the variance of the lightcurve (Schlittgen, 1995). P_j gives the fraction of the total lightcurve variance due to its variability with frequency f_j. A periodic sinusoidal variability $a_j = \sin 2\pi f' j\Delta t$ yields a narrow peak at the frequency bin f' in the PSD. The PSD fits well to search time series for periodic variability, e.g. orbital frequencies of binaries or pulse periods of pulsars. Furthermore one can use a PSD to analyze variability characterized by a continuous distribution of frequencies, what is the case for the examination of X-ray fluxes from black hole binaries.
The measured timeseries a_j is assumed to be normally distributed for a large number of bins, which holds for the bintime of $2^{-9}s$ and an average observation time of a few ksec. van der Klis (1989) shows, that the corresponding PSD values are χ^2-distributed with two degrees of freedom. The statistic uncertainty of a single PSD is of the order of the PSD value itself, but in the case of averaging the uncertainty will scale with the square root of averages bins. Therefore the lightcurve is cut in a number of shorter segments. For each the $M_m athrmseg$ segments a PSD value is calculated and the results are averaged. Another improvement to the signal-to-noise ratio of PSDs can be done by rebinning the values to a wider frequency grid. After rebinning, $M_{\mathrm{freq},i}$ old frequency bins contribute to the new one of the logarithmic grid. Both cases are applied to the calculated PSDs in this work, so

$$M = M_{\mathrm{freq}} \times M_{\mathrm{seg}} \tag{4.8}$$

PSD values contribute to the final frequency bin. van der Klis (1989) have also demonstrated, that the 1σ uncertainty of an individual unrebinned PSD is in the order of the intrinsic Poisson noise PSD itself. The same arguments hold for the signal part of the PSD, allowing to express the uncertainty of the averaged and rebinned PSD as

$$\sigma \langle P_j \rangle = \frac{\langle P \rangle}{\sqrt{M}} \tag{4.9}$$

Even though the rebinning lowers the frequency resolution of the PSD and cutting the lightcurve to segments worsens the lowest accessible frequency of the DFT, this technique is the only way to achieve good signal-to-noise ratios to analyze the PSDs correctly. As mentioned above there are three sizes of segments used for calculations. The short segments contribute to good statistics at high frequencies, where a larger number of segments M_{seg} are averaged. On the other hand using long segments extends the frequency bandwidth to lower values at the cost of bigger uncertainties. For the broad band PSD studies in this work a logarithmic frequency rebinning ($\Delta f/f = 0.15$) was chosen here as proposed by Pottschmidt (2002). More detailed discussions of the Fourier calculations used for this work can be found in Pottschmidt (2002) and Nowak et al. (1999a). In Fig. 4.2 a segment of a Cyg X-1 hard state lightcurve is shown in the upper plots. The lightcurve is shown in the two common time resolutions, which are used in this work. The corresponding PSD of the whole observation is depicted in the lower plots of this figure in the most common versions.

4.2.3 Normalization of the PSD

The raw value of a PSD is unusable for comparison with other ones. In X-ray astrophysics there are several normalizations of a PSD that are useful for different applications. The normalization is

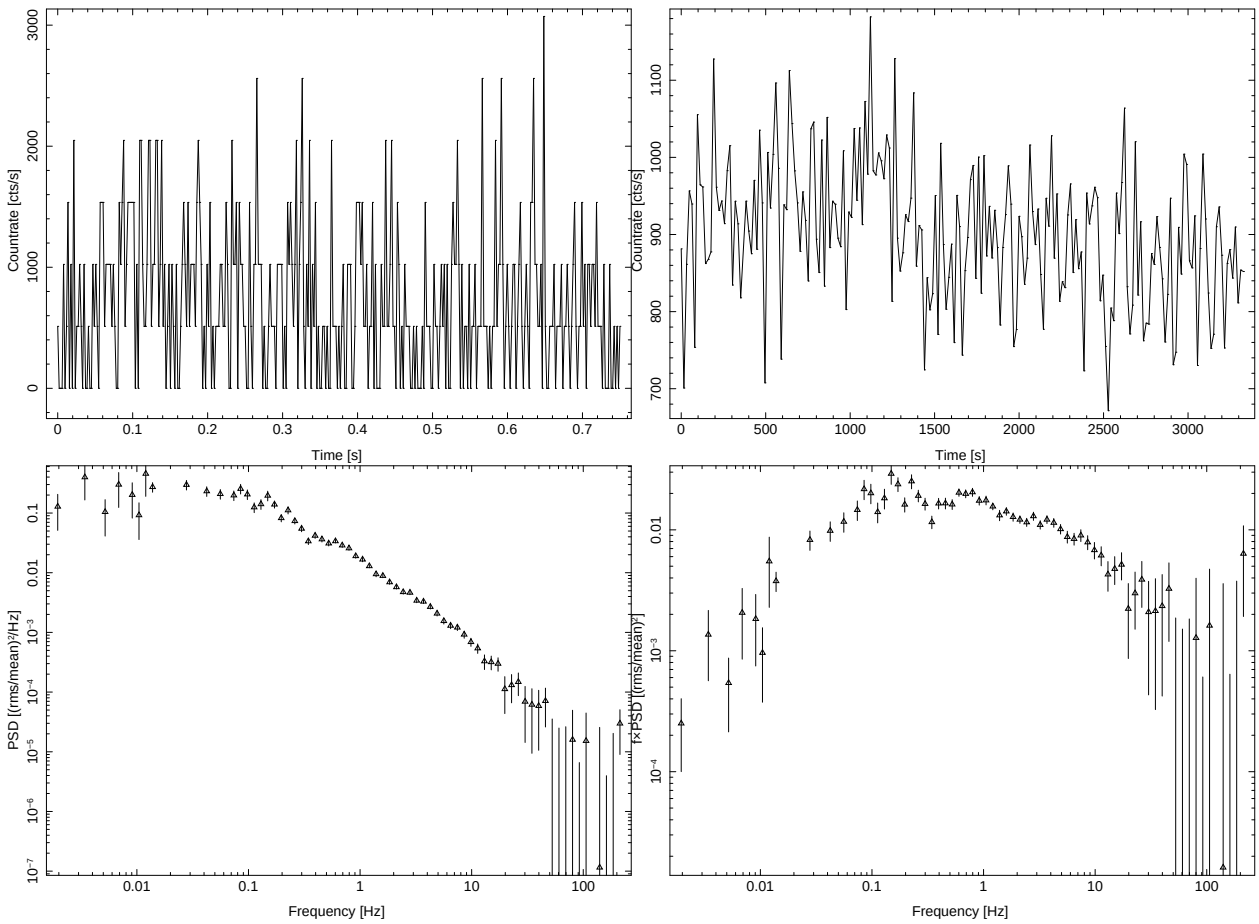

Figure 4.2: The upper two plots are examples for the lightcurves, which are used in this work. The left one is a short cutout of 0.8 s duration of a high time resolution lightcurve. The right plot is a standard2f lightcurve over the full duration of the same observation. It illustrates the variability in the time of an *RXTE* orbit. The lower to panels introduce the common diplays of a power spectra. The PSD is plotted against the Fourier frequency in the bottom left plot, whereas $f \times$ PSD is plotted right of it. The shape of the PSD is reflected with the PSD version, the typical humps in the power spectrum can be seen more clearly in the right $f \times$ PSD depiction.

applied by multiplying the PSD with a normalization factor A

$$\langle P_{\mathrm{norm}} \rangle = A \langle P \rangle \tag{4.10}$$

The PSD array calculated with the ISIS timing tools is at the beginning unnormalized. The value is stored for later computations of cross power density values (see Sec. 4.2.5 ff.). The two important normalization types are "Leahy" and "Miyamoto". The latter is the only which takes the background into account. Furthermore the "Miyamoto" normalization provides a method to state the PSD in an instrument independent way. Using this normalization, the integral over positive frequencies yields the fractional variance of the lightcurve. A normalization routine provides three different types of normalization factors, which can be applied to the raw PSD

$$A = \begin{cases} 1 & \text{Schlittgen (1995)} \\ \frac{2}{T\,R} & \text{Leahy et al. (1983)} \\ \frac{2}{T\,R_{\mathrm{sig}}^2} & \text{Miyamoto et al. (1992)} \end{cases} \tag{4.11}$$

where $R = \langle a_j \rangle$ is the mean count rate of a lightcurve and $R_{\mathrm{sig}} = R - R_{\mathrm{bkg}}$ is the background corrected signal count rate. The background spectra can be extracted from *RXTE*'s raw data files

and an estimation for the background counts is done by summing up the spectral channels and dividing them by the exposure time. In this work the Miyamoto normalization (Miyamoto et al., 1992) was applied with and without background correction, whereas only the uncorrected PSDs were used since PCU 0 aboard *RXTE* is damaged and is producing enhanced background counts that are difficult to correct for.
The factor 2 in the numerator allows to ignore $|A_{-j}|^2$, which is equal to $|A_j|^2$. The raw, not squared values A_j and A_{-j} differ, as they are complex conjugated quantities. The result is the square of the root mean square (rms) divided by the average count rate given in $(\mathrm{rms}/R_{\mathrm{sig}})^2/\mathrm{Hz}$:

$$\frac{\mathrm{rms}^2}{R^2} = \frac{\left\langle a_j^2 \right\rangle - \langle a_j \rangle^2}{R^2} \tag{4.12}$$

On the other hand, the "Leahy" normalization (Leahy et al., 1983) is a good method to study noise and deadtime effects on the PSD. It delivers the lightcurve variance per frequency interval given in $\mathrm{rms}^2/\mathrm{Hz}$. The Poisson noise level can be found at value of 2 in this normalization, independent of the incident detector count rate.
In addition to the calculation of raw PSDs, all of them were normalized to "Leahy", background corrected "Miyamoto" and uncorrected "Miyamoto" normalizations and stored for further analysis. The PSDs discussed in Chap. 6 are usually given in "Miyamoto" normalization, if nothing else is stated there.

4.2.4 Noise and Deadtime Influence on the PSD

As mentioned in Sect. 4.2.2 the measured timeseries consist of a Poisson counting noise part and a signal part of the source. In order to analyze the measured PSD, a noise estimation with detector deadtime influence has to be calculated and subtracted. From Eq. 4.6 follows for the unnormalized signal component of the PSD

$$\left\langle |S|^2 \right\rangle = \langle P \rangle - \left\langle |N|^2 \right\rangle \tag{4.13}$$

van der Klis (1989) shows that A_j and N_j are uncorrelated and the cross terms will approximately average out to zero, The noise estimation can be normalized like every other PSD. The theoretically calculated noise component has still statistic uncertainties. The difference between measured PSD and the noise calculation still shows deviations from the signal component. Because the expectation value of these deviations is the signal component, the uncertainty can be calculated as follows

$$E = \frac{1}{\sqrt{M}} \left\langle |N|^2 \right\rangle \tag{4.14}$$

E is called the effective noise level. The value of the effective noise level depends on the number of averaged values and tends to be high, if the observation time is short. If the signal PSD has a significant higher value than this level the values can be trusted. In regions about the effective noise level and below, a structure in the PSD tends to be from statistical errors and is not source related. A PSD with a good noise level is shown in Fig. 4.3

However, the noise component of the PSD is modified by effects of detector deadtime. If a X-ray photon triggers a detector, there is a short time period during which the detector cannot register any further photons. In the case of *RXTE*'s PCA this is the time where the electrons generated by the incident photon are transported to the anodes and the detector gas becomes neutral again. Pottschmidt (2002, and references therein) describe and test the different types of deadtime influence on a PSD. There is a paralyzable type, where every incident photon causes deadtime, a non-paralyzable type, where only detected photons cause the deadtime and a general deadtime caused by very large events (VLE), as described by Zhang et al. (1995). Very large events are cosmic ray detections which deposit a large energy amount in the detector. The VLE rate can be extracted from PCA raw data files for each observation. The influence of deadtime on the

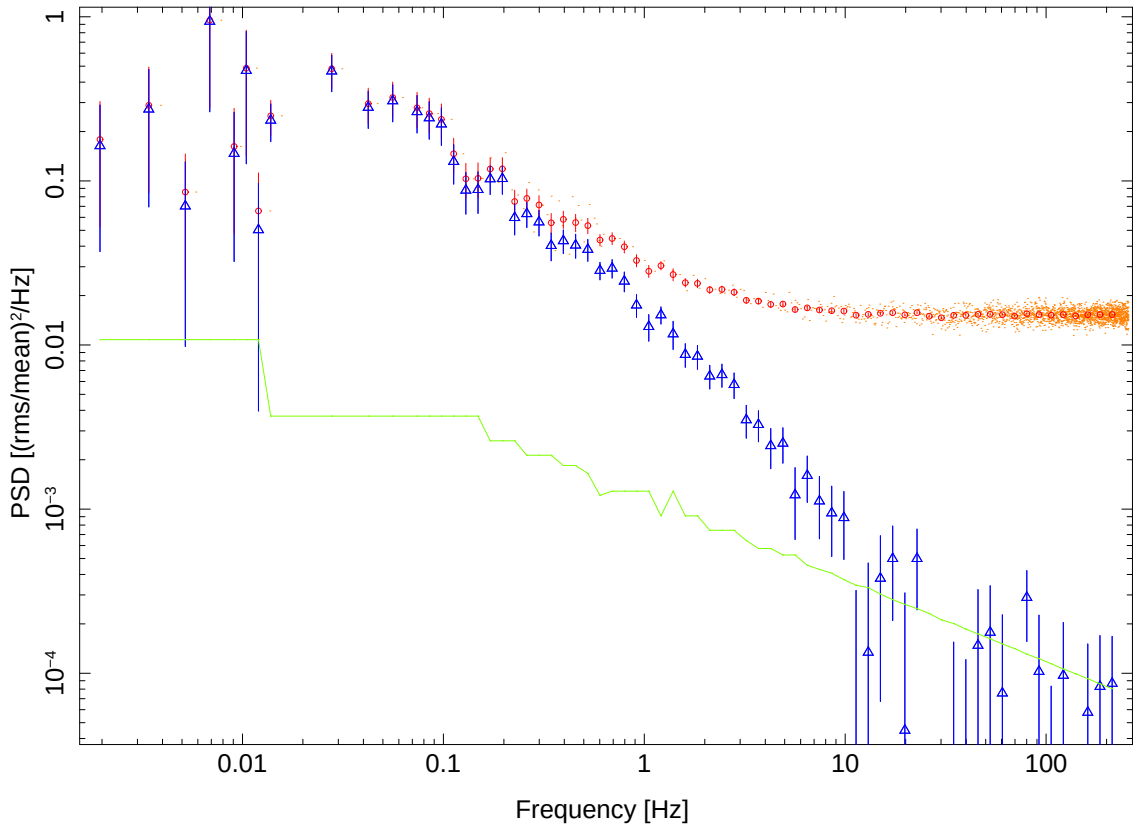

Figure 4.3: Effects of rebinning and noise-correction (with deadtime influence) on the PSD. The orange dots are the computed PSD values in full Fourier frequency resolution. Error bars are left out for clarity. Red circles mark the values after rebinning to a logarithmic grid. Blue triangles show the PSD after noise subtraction is performed. The green line again shows the effective noise level.

counting noise is frequency dependent. For an individual noise measurement the corrected noise component $|N_j|^2$ can be written as

$$|N_j|^2 = |N_{\text{Poisson}}|^2 \cdot (1 + k_{\text{dead},j} + k_{\text{inst},j}) \tag{4.15}$$

The deadtime influence is split in two parts. For PCA observations the instrument dependent deadtime k_{inst} is mainly caused by very large events. These detections are identified aboard the spacecraft and are filtered out. The resulting lightcurve does not contain these events. Therefore the deadtime correction only has to be applied for instrument-independent effects k_{dead}. An extensive study of deadtime effects on the Poisson noise contribution to a PSD was performed by Zhang et al. (1995). For PCA observation of Cyg X-1 and similar observations, it shows, that a paralyzable deadtime correction is suitable. The following equation describes the deadtime for one PCU

$$k_{\text{dead},j} = 2R_{\text{PCU}} \left[\frac{\sin(2\pi\tau_{\text{Det}} f_j)}{2\pi f_j} \right] \tag{4.16}$$

Here R_{PCU} is the count rate per PCU and τ_{Det} is the detector deadtime. For PCA the deadtime τ_{Det} is about $10\mu s$. Considering different numbers of activated PCUs, one can figure out, that deadtime is only influencing the PCU, what measured the photon, while the other PCUs activated remain in the state of being able to detect another event. Fig. 4.4 shows a the noise estimation for different number of PCUs.

The results of this work have undergone all steps described in the sections above. The final PSD is calculated from several segments and rebinned to a logarithmic grid. The data are normalized to

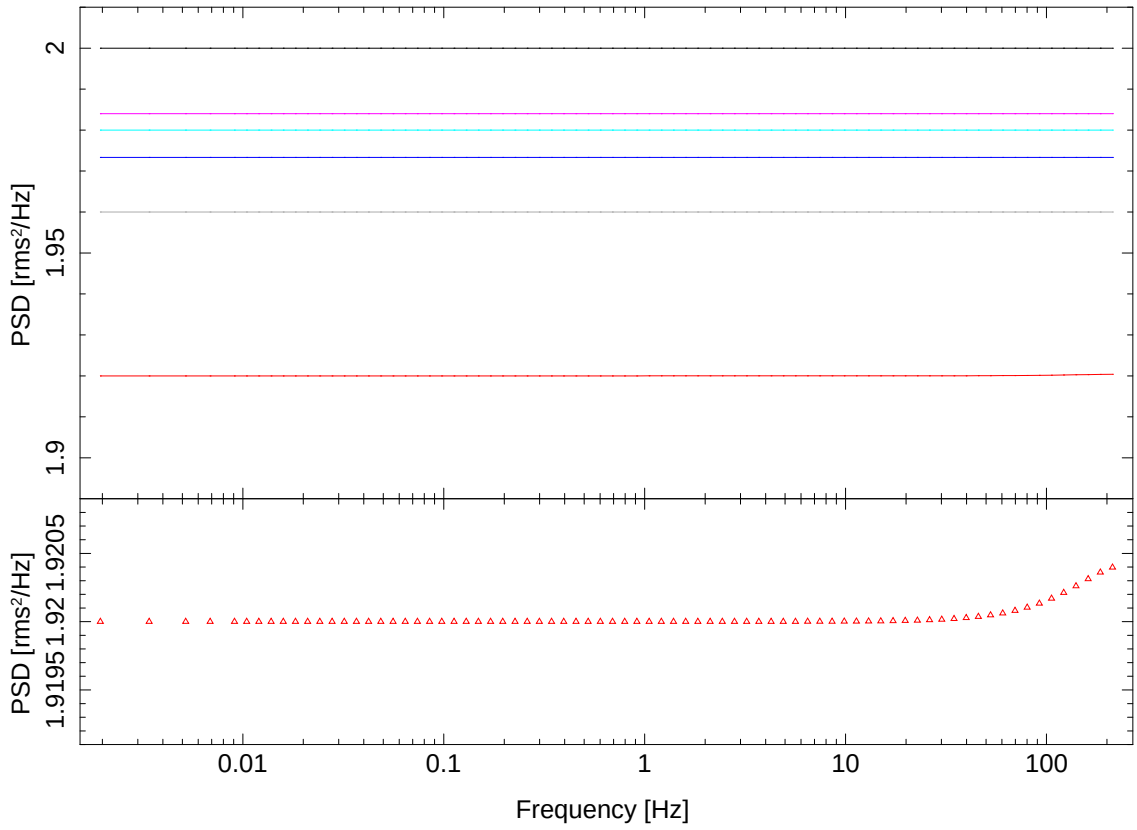

Figure 4.4: Display of the noise estimation in Leahy normalization. The calculated noise levels are shown in the top panel for different settings: The black line is the Poisson noise estimation without deadtime effects. From top to bottom the noise estimation with a instrument deadtime of 10 μs is plotted for 5 (pink), 4 (teal), 3 (blue), 2 (grey) and 1 (red) activated detectors. The bottom panel is a magnification of the red line above. The deadtime influence changes at higher Fourier frequencies.

"Miyamotos"'s norm and afterwards the computed noise estimation is subtracted. For each PSD the effective noise level is calculated, too.

4.2.5 Cross Power Density - CPD

The cross power density (CPD) is a complex quantity obtained from the Fourier transforms of two different time series $a_{1,j}$ and $a_{2,j}$, e.g., the lightcurves of two different energy bands of one observation (see Pottschmidt, 2002, Sect. 3.3). The CPD is calculated by multiplying the Fourier transforms $A_{1,j}$ and $A_{2,j}$ of both time series:

$$C_j = A^*_{1,j} A_{2,j} \tag{4.17}$$

As in the case of PSDs, an average over segments and over frequencies is calculated to improve signal-to-noise ratio. In contrast to the PSD, the CPD is a complex quantity. To illustrate the meaning of this value it can be represented by a complex vector as shown in Fig. 4.5. The CPD itself is not used for analysis. Instead its magnitude and complex phase are used to derive further quantities. The coherence function is a value derived from the magnitude, whereas the phase of the complex values leads to the time lag spectrum. Both quantities are suitable for comparisons betweens different energy bands to perform spectro-timing analysis.

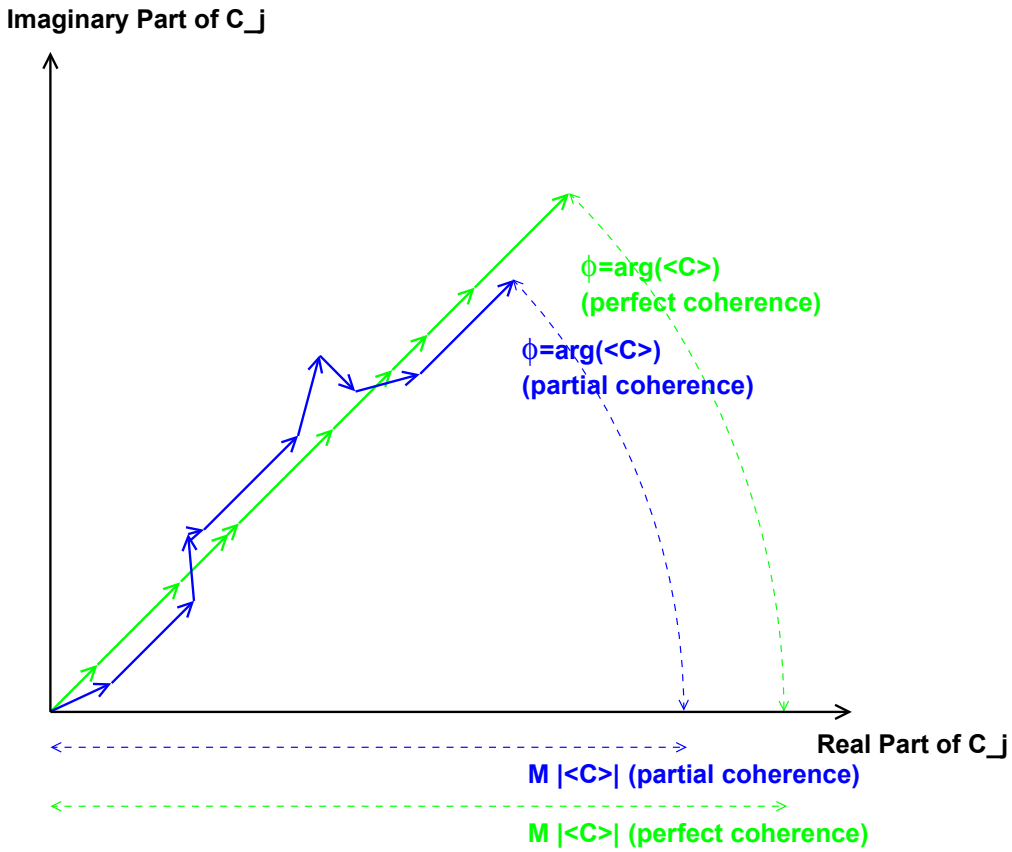

Figure 4.5: Vector representation of the cross power density. The average CPD is calculated by averaging over different segments, represented by the single vectors. The vector sum represents the averaged CPD multiplied by the number of segments $M \cdot |\langle C \rangle|$. In the case of perfect coherence (green), the alignment of the vectors is strictly parallel. Whereas the blue vectors depict partial coherence. A uncertainty in the phase and a lower magnitude of the summed vector can be seen, which leads to uncertainties of the time lag. (Pottschmidt, 2002, Fig. 3.2)

4.2.6 The Coherence Function

The coherence (Vaughan & Nowak, 1997) is a quantity calculated for two simultaneous lightcurves from different energy bands, in the following $s(t)$ and $h(t)$. Their discrete Fourier transforms are denoted as $S(f)$ and $H(f)$, respectively. There exists a transfer function t_r between the two lightcurves, from which the coherence function can be deduced:

$$h(t) = \int_{-\infty}^{\infty} t_r(t-\tau)s(\tau)\,d\tau \tag{4.18}$$

The same holds for the Fourier transformed quantities, where $T_r(f)$ is the Fourier transform of the transfer function:

$$H(f) = T_r(f)\,S(f) \tag{4.19}$$

If $T_r(f)$ is constant for an ensemble of measurements, the fundamental processes are called coherent at frequency f. In this case the average over a set of calculated cross power densities (CPD) can be predicted from one lightcurve, if the transfer function is known:

$$|\langle C(f)\rangle|^2 = |T_r(f)|^2 \left\langle |S(f)|^2 \right\rangle^2 = \left\langle |S(f)|^2 \right\rangle \left\langle |H(f)|^2 \right\rangle \tag{4.20}$$

as defined above (Eq. 4.17). In this equations angle brackets stand for an average over an infinite set of measurements of the same process. The coherence function γ is then defined after Vaughan

& Nowak (1997, Eq. 2)

$$\gamma^2(f) = \frac{|\langle C(f)\rangle|^2}{\langle |S(f)|^2\rangle \langle |H(f)|^2\rangle} \tag{4.21}$$

which is the squared magnitude of the average CPD divided by the signal PSDs of both light curves. The coherence is a measure of the degree of linear correlation between two time series at a Fourier frequency f. A complete mathematical description can be found in Vaughan & Nowak (1997) and references therein. The values considered up to now are noiseless measurements. Poisson noise causes a larger squared magnitude of the CPD $|C(f)|^2$ and therefore values of $\gamma > 1$ are possible. If the PSDs in the denominator of Eq. 4.21 are not noise-corrected, too, the coherence function is again $\gamma(f) \in [0, 1]$. In the case of raw values without noise-correction, γ is called raw coherence function.
Both measured PSDs consist of a signal and a noise component, the squared magnitude of the CPD can be written as

$$\begin{aligned} |\langle C\rangle|^2 &= |\langle S^* H\rangle|^2 = |\left\langle (S^*_{\rm sig} + S^*_{\rm noi})(H_{\rm sig} + H_{\rm noi})\right\rangle|^2 \\ &= |\left\langle (S^*_{\rm sig} H_{\rm sig})\right\rangle + \left\langle (S^*_{\rm sig} H_{\rm noi})\right\rangle + \langle (S^*_{\rm noi} H_{\rm sig})\rangle + \langle (S^*_{\rm noi} H_{\rm noi})\rangle|^2 \end{aligned} \tag{4.22}$$

From this equation a quantity can be defined, which can be interpreted as the noise component of the measured CPD:

$$C_N^2 = \frac{1}{N}\left\langle |S_{\rm sig}|^2\right\rangle \left\langle |H_{\rm noi}|^2\right\rangle + \left\langle |S_{\rm noi}|^2\right\rangle \left\langle |H_{\rm sig}|^2\right\rangle + \left\langle |S_{\rm noi}|^2\right\rangle \left\langle |H_{\rm noi}|^2\right\rangle \tag{4.23}$$

For high powers and high measured coherence, as appropriate for Cyg X-1, what means a higher signal level than the noise level contributing to the CPD (Pottschmidt, 2002, Eq. 3.25, 3.26), Eq. 4.22 can be separated and the noise-corrected signal coherence is given by

$$\gamma^2_{\rm sig} = \frac{|\langle C\rangle|^2}{\langle |S_{\rm sig}|^2\rangle \langle |H_{\rm sig}|^2\rangle} - \frac{|\left\langle C_N^2\right\rangle|^2}{\langle |S_{\rm sig}|^2\rangle \langle |H_{\rm sig}|^2\rangle} = \frac{|\langle C\rangle|^2 - C_N^2}{\langle |S_{\rm sig}|^2\rangle \langle |H_{\rm sig}|^2\rangle} \tag{4.24}$$

The statistical uncertainty of the noise corrected coherence can be calculated following Bendat & Piersol (2000); Vaughan & Nowak (1997). To illustrate how the coherence function measures the degree of linear correlation, consider the CPD as a vector in the complex plane as shown in Fig. 4.5

$$C = S^* H = |S| \cdot |H| \cdot e^{i(\Phi_H - \Phi_S)} \tag{4.25}$$

In the case of perfect coherence the vector resulting from summing up the single CPD measurements (shown as a single vectors) has the largest value. Partial coherence shortens the resulting vector. An example for a coherence spectrum of Cyg X-1 is depicted in Fig. 4.6.

A consideration about physical models and their influence on the coherence function is given in Nowak & Vaughan (1996). The quantities of the coherence function, measured and noise-corrected, as well as their uncertainties are calculated with ISIS. The signal coherence is part of the timing analysis later on and all values are stored for the computation of the time lags.

4.2.7 Phase and Time Lags

For the calculation of time lags again the lightcurves $s(t)$ and $h(t)$ with their Fourier transforms $S(f)$ and $H(f)$ from two different energy bands are considered. The calculation follows Nowak et al. (1999a) and Pottschmidt (2002, Sect. 3.5). As mentioned in the description of the coherence function (Sect. 4.2.6), the cross power density is a complex quantity, which can be stated as a vector in the complex plane. The argument of this vector is to be interpreted as the phase difference between intensity fluctuations of corresponding time series:

$$\Phi(f) = \arg(\langle C(f)\rangle) = \arg(\langle S^*(f) H(f)\rangle) = \Phi_H(f) - \Phi_S(f) \tag{4.26}$$

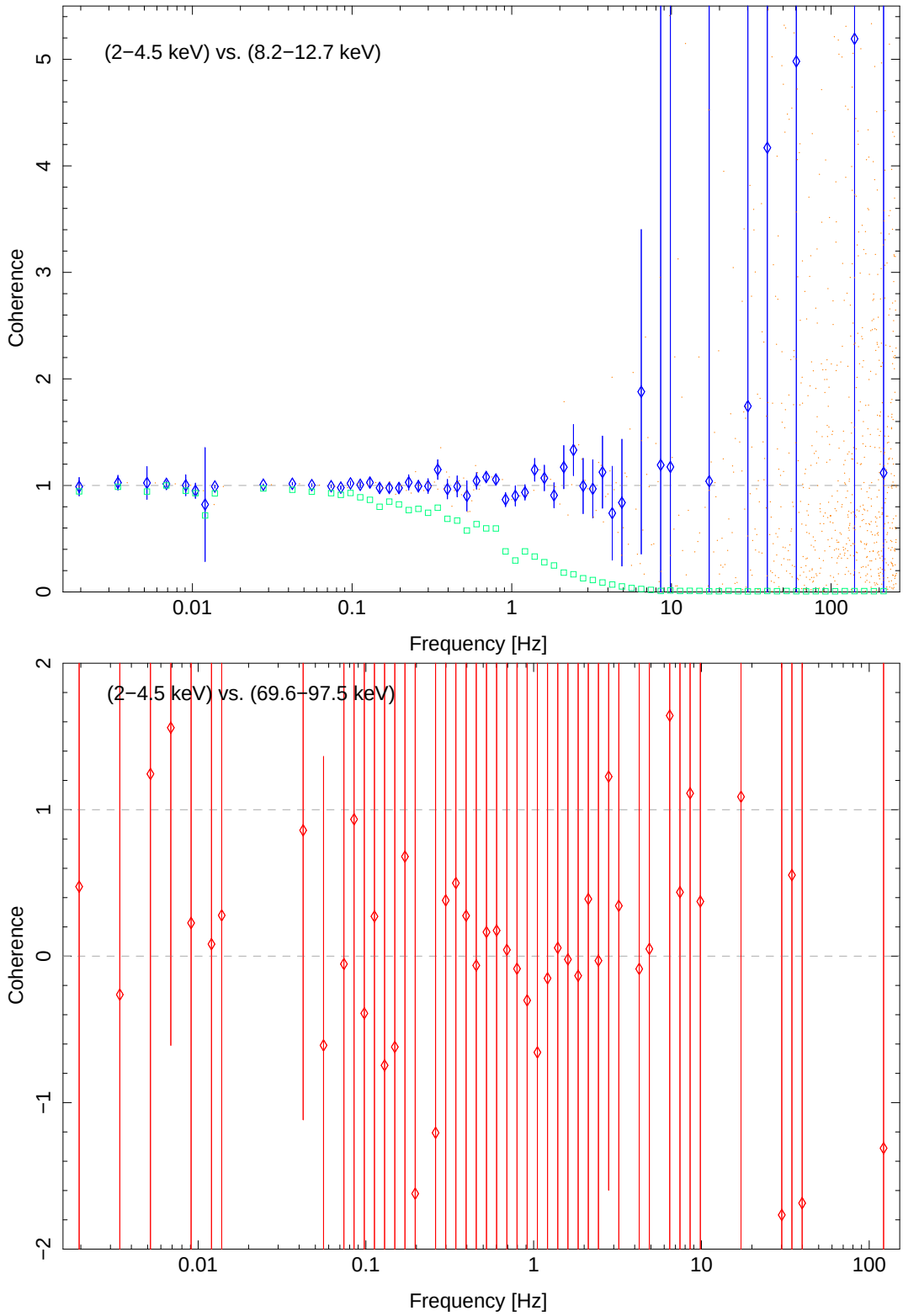

Figure 4.6: Typical coherence functions of Cyg X-1 in its low/hard state. The upper panel shows the coherence between energy band 1 and 4. The logarithmically rebinned coherence of the raw data is plotted with green boxes. Uncertainties for this value are not computed. The blue diamonds depict the noise-corrected coherence of the signals in both energy bands with the associated uncertainties. Orange dots are the same data before rebinning. Their errors are left out for clarity as they are too large to get a clearly represented plot. The noise corrected coherence between the lowest and the highest back ground dominated energy band is shown in the bottom plot to illustrate the lack of comparable signals in at high energies.

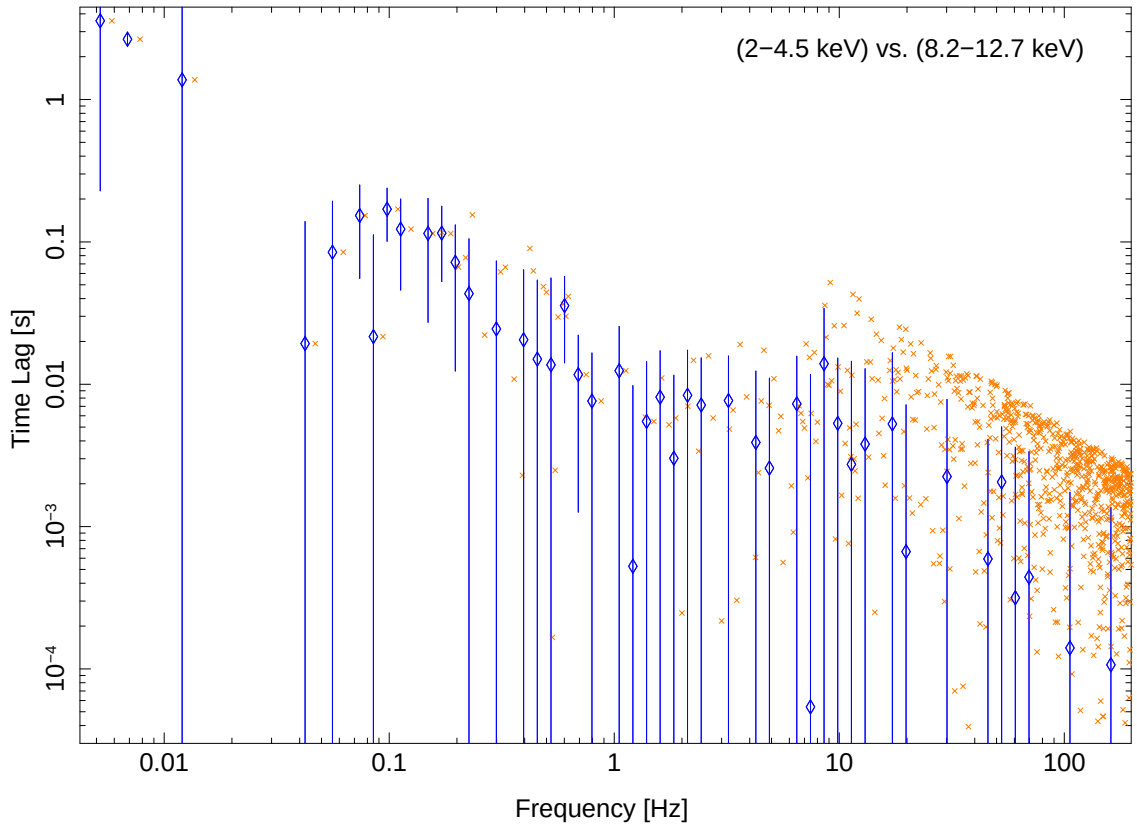

Figure 4.7: A typical time lag spectrum of Cygnus X-1 between the energy bands uses in the upper panel of Fig 4.6. The blue diamonds represent the rebinned data with their uncertainties, orange dots mark the unbinned data, which is calculated at full frequency resolution. Errors bars of the unbinned data are left out for clearness.

Dividing these values with their corresponding angular frequencies yields the time lag $\delta_t(f)$

$$\delta_t(f) = \frac{\arg(\langle C(f)\rangle)}{2\pi f} = \frac{\Delta\Phi}{2\pi f} \tag{4.27}$$

By the definition above a positive time lag is measured, if the signal from the hard energy band is delayed to the measurement of the soft band. As counting noise changes the values of the coherence function and the power spectra with normal distributed uncertainties, the contribution to the phase measured here is completely random. The expectation value of the phase shift is not affected, but its uncertainty is enhanced (Pottschmidt, 2002, and references therein). Nowak et al. (1999a) developed a model for the uncertainties due to Poisson noise and estimated for their 20 ksec observations a Fourier frequency range from 0.1–30 Hz, where the time lags are trustable. The observations analyzed in this work are on a quite short timescale compared to 20 ksec, what leads to a narrower frequency range of usable time lags. The statistical deviations in CPD and PSD constitute uncertainties in the coherence function and in the phase shifts. Pottschmidt (2002, Sect. 3.5.3) explains a short summary on the errors of the timelags. In Fig. 4.7 a typical time lag spectrum of Cyg X-1 is depicted. If the term “time lag” is used in the following, usually an averaged range of this lag spectrum is named. Like the coherence, the time lag is calculated for Fourier frequency regions where a markable contribution of the total rms of the PSD can be found.

Chapter 5

Modelling the Data

The spectra and computed PSDs, covering 10 years of X-ray observations of Cyg X-1, need to be fitted with models in order to compare the parameters in the different states of the source. All fit functions and the fitting process itself were done in ISIS, which is designed for fitting spectra. The following sections describe the different approach of spectral and timing fitting and introduce the models used to fit the data. In the case of power spectral densities a couple of models were fitted, some describe the data better in hard states, the other work well with intermediate and soft state data. In order to determine the right model, the fit statistics were checked with a F-test algorithm for their significance.

5.1 Spectral Fitting

In contrast to optical astronomy, X-ray flux spectra cannot be measured directly. The X-ray photons interact with matter and the resulting effects are read out. Hanke (2007, Sec. 2.2.1) describes the different effects which lead to a change of the real photon energies to measured ones. The detectors have usually digital read-out electronics, which produce no continuous but binned output data, e.g., the voltage caused by a incident X-ray photon in the proportional counters of *RXTE*'s PCA is given to a pulse height analyzer (PHA), which determined the energy channel of the event. On the one hand the binning of the spectral data lowers the amount of data telemetered to earth, on the other hand the energy resolution of the detector does not demand a narrower grid of channels. Another effect on the shape of the spectrum measured by the detector is its energy response behavior. Wilms (1998, Sec. 4.1) gives a detailed description of PCA's response. To understand the effects of binning and response, one considers the following equation (Böck, 2008, Eq. 3,2):

$$C_{\mathrm{D}}(i) = C_{\mathrm{B}}(i) + t_{\mathrm{exp}} \int_0^\infty R(i,E) \cdot A(E) \cdot F(E)\, dE \tag{5.1}$$

Here $C_{\mathrm{D}}(i)$ are the counts in the ith channel of the detector. The measuredcount rate is the sum of background counts $C_{\mathrm{B}}(i)$ and the real source flux $F(E)$ in the exposure time t_{exp} modified by the response matrix. This matrix is split into two parts in this equation:

- The redistribution matrix function (RMF) which is noted as $R(i,E)$ gives the probability that a photon with the energy E causes an event in the ith detector bin. An ideal detector with continuous spectral resolution would have a δ-function $\delta(E_i,E)$ as RMF for each energy E. In a real detector the RMF describes several effect, e.g., that a photon ionizes the detector's atoms and is therefore measured as a photon of lower energy. The photon emitted by recombination of such events is measured, too, what changes the spectrum.
- $A(E)$ describes the ancillary response function (ARF), which is mainly the effective area of the detector modified by variations due to the used material.

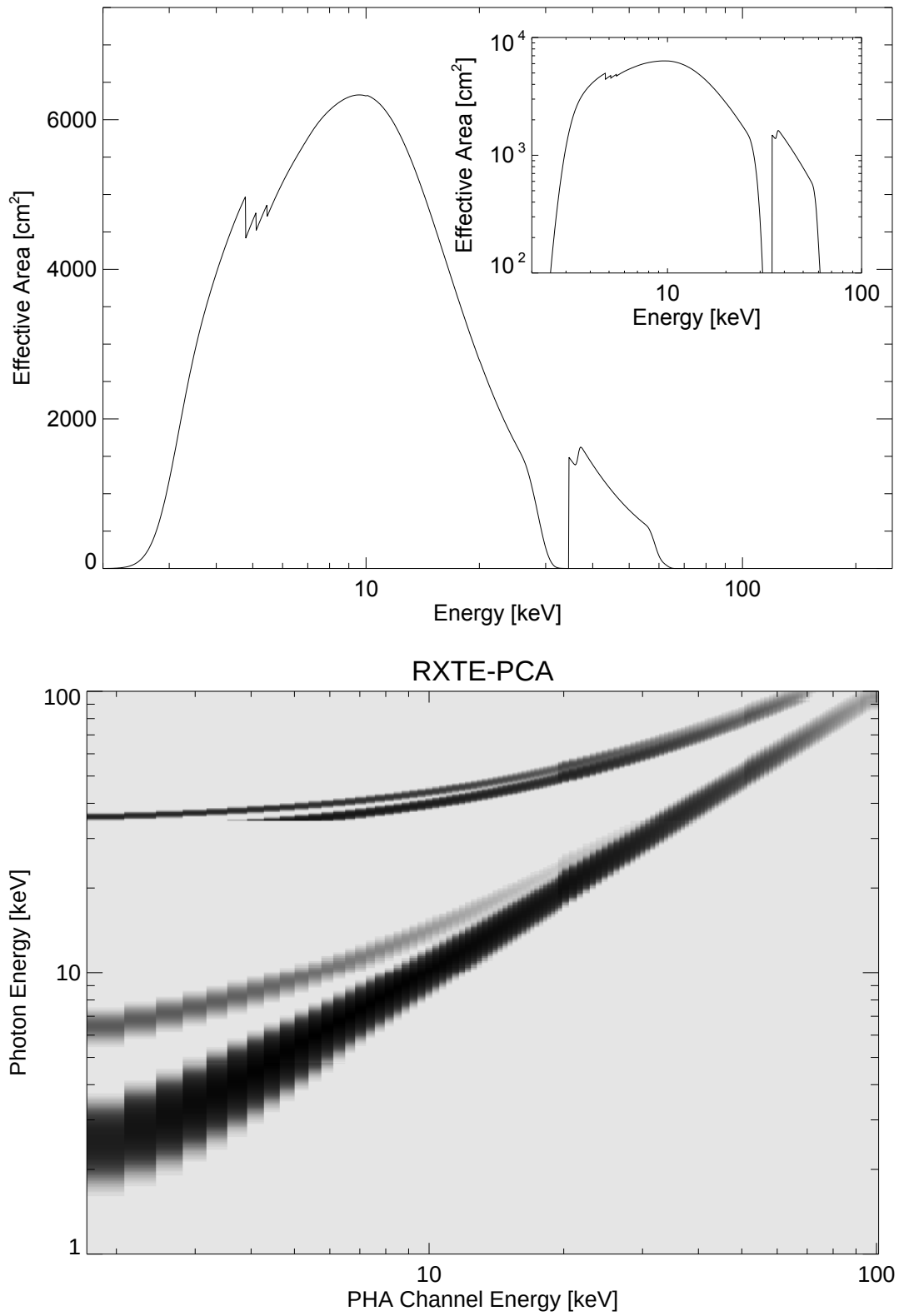

Figure 5.1: The top panel shows the PCA effective area as a function of energy. In the inset, the same data are plotted in logarithmic form. The effective area is the main component of the ARF. (Wilms, 1998, Fig. 4.3) The bottom panel contains PCA's response matrix. The gray scale illustrates the probability, that a photon of a given energy is registered in a certain PHA-channel. (Ingo Kreykenbohm, priv. comm.)

The components of the response matrix of *RXTE*'s PCA are shown in Fig. 5.1.

The Interactive Spectral Interpretation System (`ISIS`) is designed for work with spectral datasets (Houck & Denicola, 2000). There are several routines provided for loading and analyzing a spectrum. The PHA data and the associated RMF and ARF, which are provided by the instrument's calibration team and extracted together with the spectrum from the raw satellite data, can be loaded into ISIS easily. However, the flux spectrum originating from the X-ray source $F_S(E)$ cannot be obtained in a simple way as it depends on the response of the detector. The deconvolution of $F_S(E)$ from $C_D(i)$ is generally not possible, even if the response of the detector is well known. In order to get the right source spectrum a model flux $F_M(E)$ is created and the count rates are calculated as the detector would measure it:

$$C_M(i) = t_{\exp} \int_0^\infty R(i,E) \cdot A(E) \cdot F_M(E)\, dE \tag{5.2}$$

The count rates of the model spectrum are now compared with the background corrected counts of the source $C_S(i) = C_D(i) - C_B(i)$. The parameters of the model can now be varied until the the difference between both is minimal. The value derived from this comparison, χ^2, is defined as the squared deviation of the count rates divided by the statistical Poisson error $\sigma = \sqrt{C_\mathrm{D}(i) + C_\mathrm{B}(i)}$ summed over the whole model:

$$\chi^2 = \left(\frac{C_S(i) - C_M(i)}{\sigma} \right)^2 \tag{5.3}$$

The approach to find the right model is to minimize the value of χ^2. In this work the subplex algorithm (Rowan, 1990), which turned out to be the best but slowest solution to find a global minimum of χ^2, was used for all fits. The basics of χ^2-minimization are summarized in Hanke (2007, Sec. 2.2.2) and the references therein.

In former spectral evaluations of Cyg X-1, several physical models were employed. Wilms et al. (2006) studied the long-term spectral evolution from 1999 to 2004 and used several models of the source. In the last decades several physical models were developed, which describe the X-ray emission of black hole binaries suitable. The X-ray spectrum from Comptonization is described by the `compTT` model (Titarchuk, 1994) or by the `eqpair` model (Coppi, 1999), which assumes a mixed thermal / non-thermal distribution of the Compton-scattering electrons. The reflection and downscattering of the photons from a Comptonization model at the surface of the accretion disk can be modelled with the `reflect` fit function by Magdziarz & Zdziarski (1995). Another approach is the `agnjet` model of Markoff (2005), which assumes the X-ray spectrum originating from a jet ejected from the blackhole. All these models are implemented in ISIS and can be fitted in this way. A short summary of these physical models is given by Böck (2008) and a comparison of all was done by Wilms et al. (2006). For this work a rather simpler approach was chosen as the focus is on the spectral-temporal correlations in the X-ray measurements. The PCA data were loaded to ISIS and the determination of the spectral parameters was limited to the energy range of 5 to 20 keV. The fit function used for the long-term campaign data is based on the phenomenological model of a broken power law, which describes no physical radiation process. The fit function `bknpower` only describes the shape of the recorded spectrum in the following way:

$$P_\mathrm{bknpower}(E) = \begin{cases} K \cdot (E/1\mathrm{keV})^{-\Gamma_1} & for \quad E \le E_\mathrm{break} \\ K \cdot (E_\mathrm{break})^{\Gamma_2-\Gamma_1} \cdot (E/1\mathrm{keV})^{-\Gamma_2} & for \quad E \ge E_\mathrm{break} \end{cases} \tag{5.4}$$

where K is the flux at 1 keV and Γ_1 and Γ_2 are the photon indices below and above the break energy E_break, respectively.

To improve the quality of the fit, two or three components are added depending on base of a first and foremost fit with the `bknpower` model only. In hard state observation with $\Gamma_1 < 2.4$ two

models were added. At first a Gaussian profile (`egauss`) was combined to the broken power law. The Gaussian line with a center energy tied to a small energy range around 6.4 keV is intended to describe the relativistic broadened iron K α line, found in the X-ray emission of black hole binaries. In the case of PCA, the limited energy resolution of about 0.4 keV at this energy allows to use the simple Gaussian line profile for this feature:

$$G(E) = \frac{A}{\sigma\sqrt{2\pi}} \exp\left[-\frac{E - E_0)^2}{2\sigma^2}\right] \tag{5.5}$$

On the other hand a fit function considering the interstellar absorption of X-rays was multiplied to the model. The `phabs` fit function for photoelectric absorption can be written in the following form:

$$A(E) = \exp(-N_H \cdot \sigma(E)) \tag{5.6}$$

The hydrogen column N_H is the only parameter fitted by this function. The cross-section $\sigma(E)$ does not take Thompson scattering into account. This can be done by modifying the relative abundances. A more sophisticated and upgraded model is `tbabs` (Wilms et al., 2000), in which the abundances are free fitable and the standard setting gives a better description of the observed interstellar medium. In opposite to the fit functions `bknpower` and `egauss`, which are additive models, the photo absorption is a multiplicative model. Thus the function is multiplied to those describing the emission. As shown in Fig 5.2, photo absorption is a process appearing mainly at low photon energies. The reason is the decreasing cross-section for the photo electric absorption processes with higher energies. Therefore the column density cannot be modelled well with PCA data above 4 keV. Typical values for Cygnus X-1 are about $0.6 \cdot 10^{22}$atoms/cm^2.
In soft state observations the contribution of a thermal disk is high enough to add a model for its blackbody radiation. The `diskbb` fit function is a simple model for the thermal component of the spectrum (Mitsuda et al., 1984; Makishima et al., 1986). The model is defined by two parameters, namely the temperature of the accretion disk at the inner radius T_{in} given in keV and the normalization parameter K, which is evaluated by the distance of the source d, the inner disk radius R_{in} and the inclination angle θ of the disk.

$$K = \left(\frac{R_{\mathrm{in}}/\mathrm{km}}{d/10\,\mathrm{kpc}}\right)^2 \cdot \cos(\theta) \tag{5.7}$$

In principle it is possible to determine these parameters from the spectrum. Similar to the `phabs` model, the `diskbb` is affected by the limitations of PCA observations. A typical value for T_{in} is below ≈ 1 keV for Cyg X-1. The black body emitting with a maximum of $E = 3kT$ is radiating mostly below PCA's low energy threshold and is therefore not well detected in observations with this instrument. Only the high energy part of the disk emission is detected and it can only be fitted, if the contribution of the disk is most prominent in the spectrum, e.g. in distinct soft states of Cyg X-1. Both models, `phabs` and `diskbb`, tend to be problematic during the fitting process as they can are correlated to each other in the progress of χ^2-minimization. An increase of the N_H column in `phabs` is balanced by a colder and smaller disk of `diskbb` in many cases of PCA data and therefore the fit results are not unique.

In summary the following models were used to fit the 5 – 20 keV spectra:

- `phabs(1) * ( bknpower(1) + egauss(1) )` for hard states with $\Gamma_1 < 2.5$
- `phabs(1) * ( bknpower(1) + egauss(1) + diskbb(1) )` for soft states with $\Gamma_1 \geq 2.5$

5.2 Timing Models

The fitting process of the the power spectra was also done with ISIS. On the the one hand the fits turned out to be faster than those with spectra. Computation time could be saved, because the data was loaded directly in ISIS and no RMF and ARF had to be taken into account. On the other

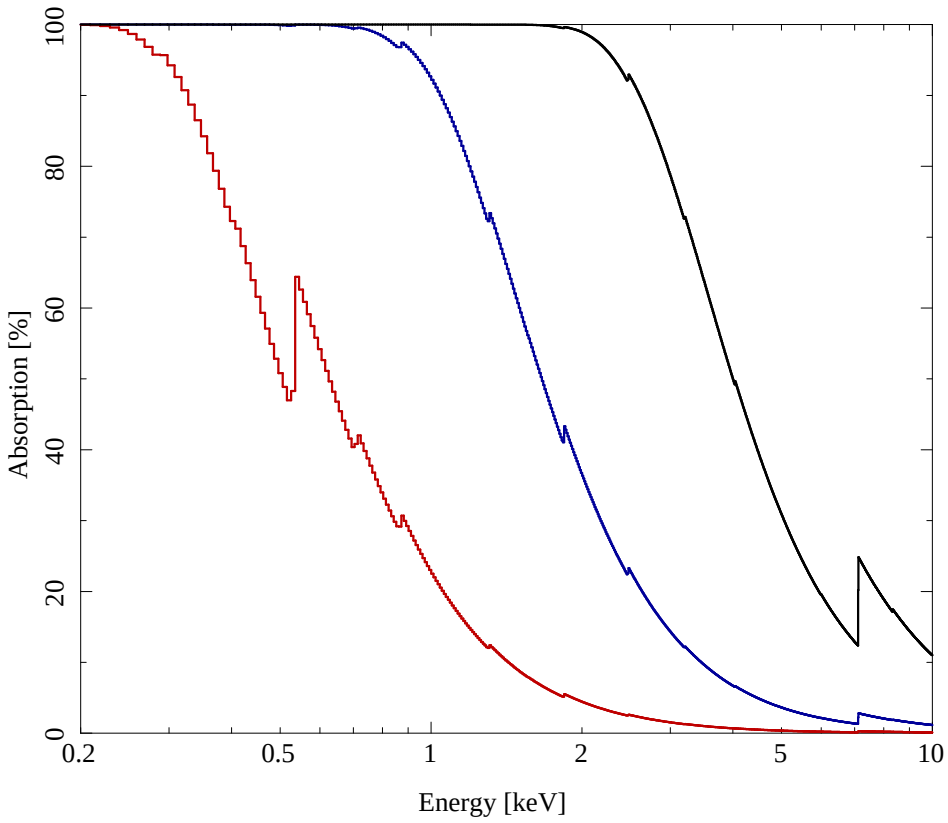

Figure 5.2: Plot of the photoelectric absorption modeled with the `phabs` function. The colors stand for different values of the equivalent hydrogen column N_{H} in units of 10^{22} atoms/cm^2.For the red graph a N_{H} of 0.1 was used, 1 for the blue one, and 10 for the black one. Values for Cy X-1 lie between 0.1 and 1. Therefore, one can see, that the PCA data above 5 keV, which was used for spectral fitting, is only marginally affected.

hand, ISIS is designed for fitting spectra, which consist of energy bins and an absolute number of counts in these bins. A spectrum is therefore called a bin-integrated value. However, the PSDs are bin-density values, what means, that ISIS cannot fit the results directly. The power spectra have to be transformed to bin-integrated values before the fit function can be calculated. This is done by simply multiplying the value with the width of the bin. Afterwards ISIS can treat the PSDs like spectra and the fit routines of ISIS can be used on it.
The power spectra are modeled with two different functions. To model the PSDs properly in soft and intermediate states a power law with exponential cutoff $P_{\mathrm{cut}}(f)$ was used:

$$P_{\mathrm{cut}}(f) = k f^{\alpha} \exp(-f/f_{\mathrm{cut}}) \tag{5.8}$$

The function has three free parameters, namely the norm k, the powerlaw index α and the cutoff frequency f_{cut}. The function `cutoffpl` implemented in XSPEC[1] revealed a strange behavior at low frequencies. ISIS is partially using ported XSPEC modules and therefore this problem affects the ISIS fit routines. This bug is caused by numerical problems in connection with the calculation incomplete Γ-functions[2]. The defect was discussed elaborately by Böck (2008, Sec. 5.2.2). He developed the `cutoffpl2` function, which is free of this strong deviation at low frequencies and works well for the modeling of power spectra. In the softest observations of Cyg X-1 ($\Gamma_1 \gtrsim 2.8$) the `cutoffpl2` is the only function required to model the PSD properly. In all other observations

[1] `http://heasarc.gsfc.nasa.gov/docs/xanadu/xspec/`
[2] The bug is probably already fixed, see `http://xspector.blogspot.com/2008/08/latest-xspec-patches.html`

the power spectrum is dominated by broad noise components. These broad noise components are modeled with two to four Lorentzian profiles. A Lorentzian is the Fourier transform of a damped harmonic oscillation and given by:

$$L_i(f) = \frac{\nu_i R_i^2}{\pi Q_i \left(\nu_i^2 - \frac{4\nu_i Q_i}{\sqrt{1+4Q_i^2}} f + f^2 \right)} \tag{5.9}$$

where R is the normalization factor, $Q_i = f_i/\Delta f_{i,\mathrm{FWHM}}$ the quality factor and ν_i is the peak frequency of the Lorentzian, where $f \times L_i(f)$ reaches its maximum. Pottschmidt et al. (2003) use the same, but functionally different definition of the Lorentzian: they express the peak frequency ν_i in terms of a resonance frequency f_i:

$$L_i(f) = \pi^{-1} \frac{2R_i^2 Q_i f_i}{f_i^2 + 4Q_i^2 (f - f_i)^2} \tag{5.10}$$

where the relation between the peak frequency ν_i and the resonance frequency f_i is substituted:

$$\nu_i = f_i \cdot \sqrt{1 + \frac{1}{4Q_i^2}} \tag{5.11}$$

The Lorentzian can also be used to model quasi periodic oscillations (QPOs). The noise components modeled in this work show a low value Q_i, what yields a broad profile. If the quality gets higher, the Lorentzian profile becomes narrower. QPOs, discussed by Casella et al. (2004) and Remillard & McClintock (2006), are narrow peaks in the power spectrum and are to be fitted with narrow Lorentzians. However, the rather short observations on timescales of *RXTE* orbits and below, do not have good enough data points to average. Therefore the statistic uncertainties are too high to detect to detect the QPOs, if they are present in the PSD at all. Only in a few cases of long uninterrupted observations an evidence for a small peak on top of the PSD could be assumed. But it has not been tested with fit calculations, because there are lots of deviations on many other PSDs which brings ISIS to model statistic uncertainties with narrow Lorentzians.
To calculate the contribution of one Lorentzian to the total rms of the power spectrum, one has to choose Miyamoto normalization. The rms amplitude of L_i is calculated as:

$$\mathrm{rms}_i^2 = \int_0^\infty L_i(f)\, df = R_i^2 \left(\frac{1}{2} + \frac{\arctan(2Q_i)}{\pi} \right) \tag{5.12}$$

The Lorentzian fit function `lorentzmb` was implemented by Böck (2008) and is available in the ISIS function library `isisscripts` at Remeis observatory.

All 6060 power spectra of all five energy bands were fitted with different models consisting of the components discussed above. Böck (2008, Sec. 5.2.3) found problems in the fitting process regarding the position of the Lorentzians. It must be taken into account that the positions of the components are in the same order in every model. An interchange of L_1 and L_2 within 2 fits makes them incomparable to each other. The problem was solved in his work with a `dummy` function, adding a value larger than zero to the the peak frequencies of each Lorentzian profile,so they are fitted in the same order in each power spectrum. Knowing his correlations between the peak frequency and the spectral hardness, i.e., the Γ_1 of the spectral fits, and the correlations found by Pottschmidt et al. (2003, Fig.7 b), for this work a slightly different strategy was applied. Each Lorentzian's peak frequency was tied to a frequency range, which is defined by the known correlations and the assumed positions of the lower or higher Lorentzians, respectively. This works well on almost all power spectra analyzed in this work, although some fit parameters ran against their defined borders. This problem could be solved by adding a function, which loosens the restrictions to the

Table 5.1: Table of all fit models for PSDs

Spectral state[3]	Component combination
soft	`cutoffpl2(1)`
both	`cutoffpl2(1) + lorentzmb(1) + lorentzmb(2)`
hard	`lorentzmb(1) + lorentzmb(2)`
hard	`cutoffpl2(1) + lorentzmb(1) + lorentzmb(2) + lorentzmb(3)`
hard	`lorentzmb(1) + lorentzmb(2) + lorentzmb(3)`
hard	`cutoffpl2(1) + lorentzmb(1) + lorentzmb(2) + lorentzmb(3) + lorentzmb(4)`

parameter, if it gets near the limit. Another issue with fitting some PSDs is the low signal-to-noise ratio in observations with a small number of PCUs activated, besides a short exposure time of the lightcurve. In those cases the power spectra contains one or more frequency bins in the regime, where only one raw value is averaged over. In the logarithmic grid chosen for the analysis of Cyg X-1, the first seven bins are taken from the lightcurve segments of 262.144 bins $\approx$ 0.5 ksec. There is no statistical average in Fourier frequencies below 0.0125 Hz and in some cases the FFT calculates a bin with a strong deviation from the others, which has no physical meaning and thus cannot be fitted with the used models. Fig. 5.3 a shows a failed fit of this type. On the other end of the calculated Fourier frequency range there is a occurrence of a similar issue, that induces the fitting process to fail. If the X-ray flux of the source is high and the count rates exceed a certain limit, what is the case in some soft/high states, the background estimation of PCA turns out to wrong. The $f \times$ PSD plot in Fig. 5.3 b shows the diverging behavior of the power spectrum, what leads to unusable fit parameters. In order not to waste the data in these observations, they ware filtered out and treated with a different frequency range, in which the fit algorithm works. By setting the limits to [0.0125Hz; 80Hz] all the mentioned datasets could be inserted to the overall analysis.

5.3 Determining the right model

In the course of this work different models were applied to the power spectra. Both components described in the last section (5.2) were tested in different combinations. Table 5.3 lists all used fit models.

Considering Table 5.3, one can figure out, that the models are stacked. There is always a model nested in another, except for the models with the most free parameters, `cutoffpl2(1) + lorentzmb(1) + lorentzmb(2)` for soft states and `cutoffpl2(1) + lorentzmb(1) + lorentzmb(2) + lorentzmb(3) + lorentzmb(4)` for hard states. Beginning at the fit results of the smallest model, one can apply a statistical test to confirm if there is a model which describes the data more precisely. Adding a fit function to an established one raises the number of free parameters, what usually leads to a better value χ^2, since the new model can adjust the measured data points more precisely. Whether the new fit result is a significant improvement to the total χ^2, can be tested with a maximum likelihood procedure. Roe (2001, Chap. 14) give an extensive explanation of those methods relating to curve fitting. In the case of fitting the values of power spectra, one is looking for a model to describe data points with approximately normal distributed errors. The modeling of those datasets allows to define the χ^2-value as defined in Sect. 5.1. For testing two χ-distributions of fit results for their significance, the F-Test was chosen in this work. Following Bevington & Robinson (1992, Chap. 11.4) the F-Test distinguishes between two methods determining the χ^2-statistics for their significance, e.g., the two models applied in the given case. There is no absolute estimate, if the better result is the truth. There is still an error chance, that

[3]The distinction between hard and soft state was done at $\Gamma_1 = 2.5$ for the power spectra analysis

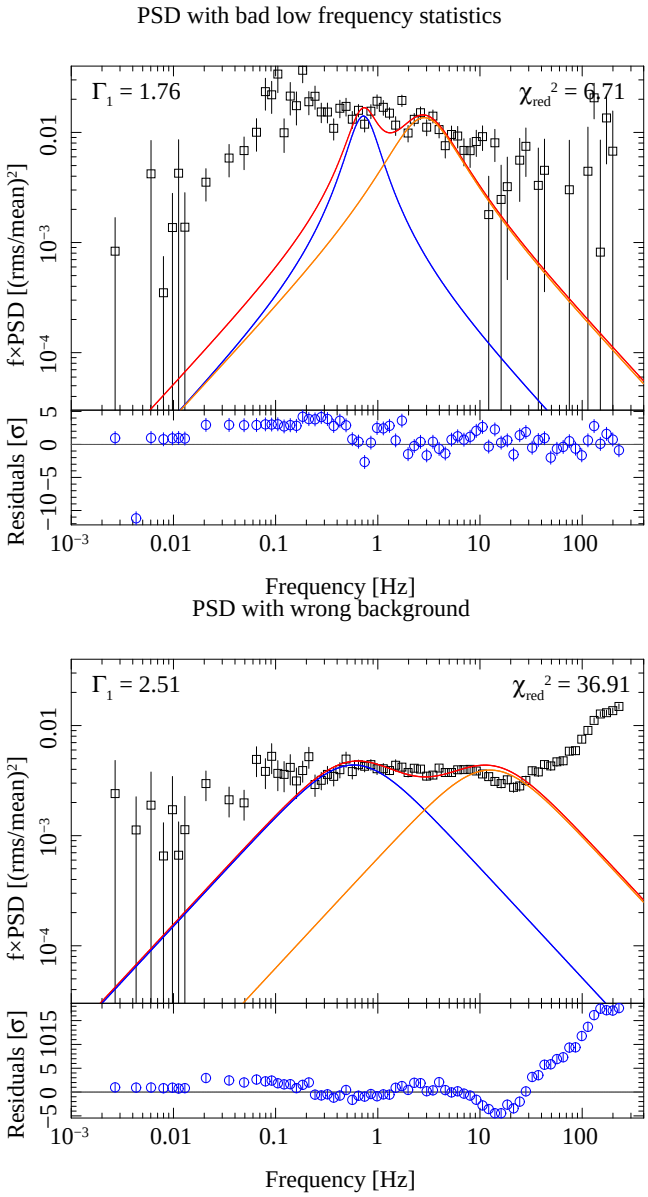

Figure 5.3: The figure shows two PSD fit results of bad data. The top panel PSD is calculated of a rather short lightcurve. Within the first seven bins, which are taken from the FFT of 262144 bin long lightcurves, there is no averaging over segments. The second bin is negative after noise correction. Thus the fit routine fails in χ^2-minimization. A PSD of a high/soft state observation is shown below. In some cases, the background estimation of PCA fails, if the count rate is too high. The consequence is a wrong background subtraction, which affects the high frequency bins. The diverging bins above $\sim 20\,\mathrm{Hz}$ make a meaningful fit impossible. In both cases, the frequency range has to be limited, to achieve reasonable results.

the hypothesis that the chosen fit result is the correct interpretation of the data, is not true. These tests are therefore called likelihood tests, because the statistical nature of the result is still defective by a certain chance. The error probability for this work was chosen to 5%. In many applications one tends to take a error probability of 1%, but the results here still show a good accordance with known results for Cyg X-1. The F-Test used in this work is given by

$$F_\chi = \frac{\chi_1^2 - \chi_2^2}{n_2 - n_1} \Big/ \frac{\chi_2^2}{N - n_2} \tag{5.13}$$

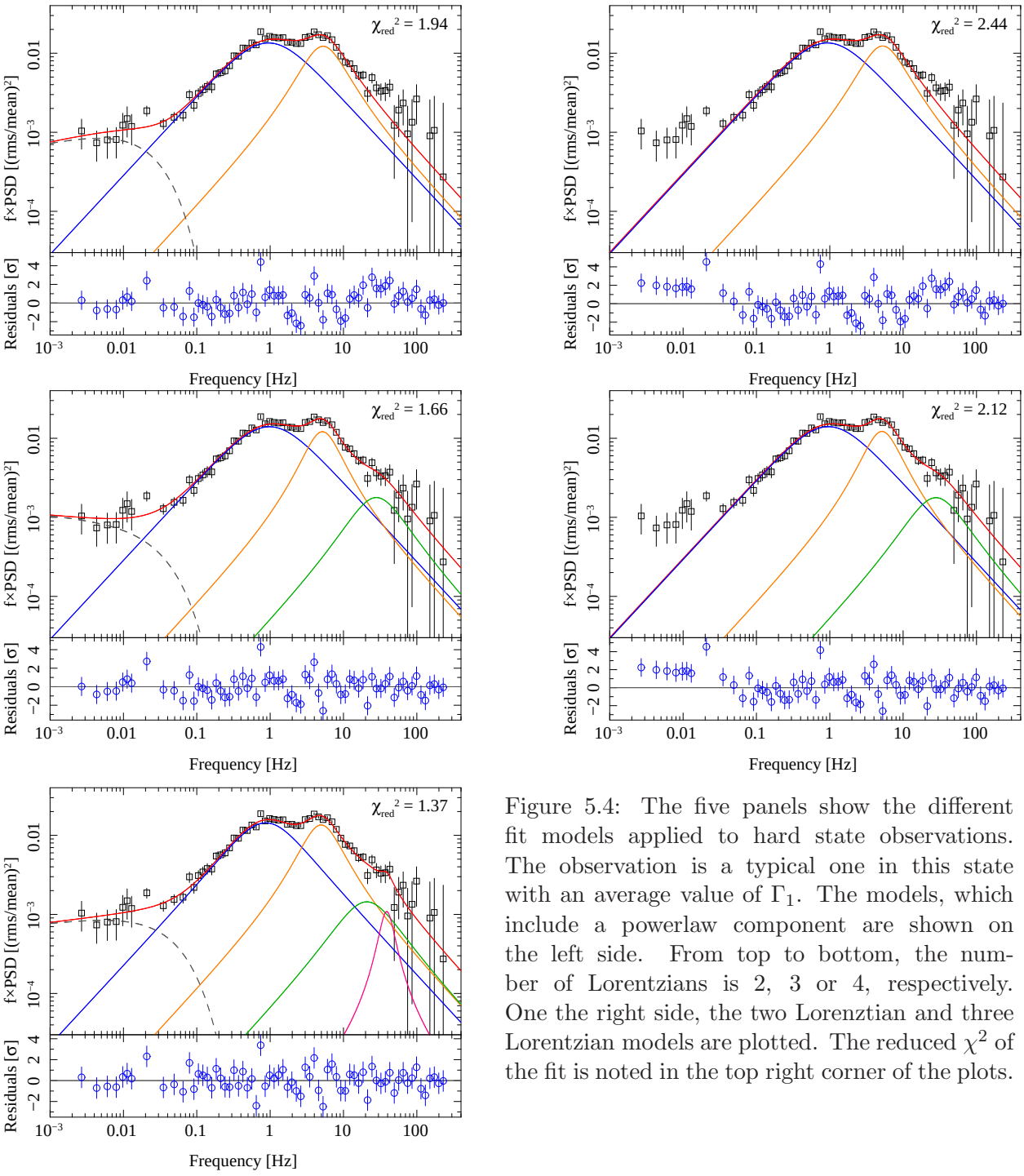

Figure 5.4: The five panels show the different fit models applied to hard state observations. The observation is a typical one in this state with an average value of Γ_1. The models, which include a powerlaw component are shown on the left side. From top to bottom, the number of Lorentzians is 2, 3 or 4, respectively. One the right side, the two Lorenztian and three Lorentzian models are plotted. The reduced χ^2 of the fit is noted in the top right corner of the plots.

derived from Bevington & Robinson (1992, Eq. 11.50). χ_1^2 and χ_1^2 are the residual sum of squares of the two models, n_1 and n_2 their parameters of the fit functions and N is the number of data points of the measurement. The value F_χ can be calculated via the F-distribution formula for the desired error probability or it can be looked up in F-value tables for the given degrees of freedom and error chance (Bevington & Robinson, 1992, Appendix C).

In soft state observation, where only two models are fitted to the data this is a single calculation done in ISIS, whereas in hard states a computation tree was formed. Beginning with the search for a model, that is significant better than the two Lorentzians, the result, if it exists, has to be tested against the fit functions with even more parameters. Fig. 5.3 one hard state observation with all possible fits is shown.

Chapter 6

Results for Cygnus X-1

In this chapter the results of the data analysis of X-ray and radio observation of Cygnus X-1 over almost ten years are presented. The data used here are acquired by the techniques described in Chapters 4 and 5. The spectral analysis focuses on the empirical broken powerlaw model fitted to the X-ray spectra of the PCA instrument. These observations are repeated every two weeks over the last ten years. To get an overview of the long-term spectral and flux evolution, data of the ASM aboard *RXTE* are taken into account, too. ASM data are nearly uninterrupted and may reveal what happened in between two PCA pointings, if the parameters changed from one observation to the next. The spectral evolution from 1999 to 2004 is described by Wilms et al. (2006, and references therein) and the data of this work are tested against results from there. Nevertheless, the spectral parameters are only a basis for the classification of Cyg X-1 states. The outcomes of Fourier calculations, i.e, the power spectra, lag spectra, and coherence characteristics, of Cyg X-1 are correlated with spectral properties and the timing characteristics themselves are examined for systematics. The work of Pottschmidt (2002) is taken as a guideline for these calculations and analysis techniques. Many publications over the last 15 years include timing analyses of X-ray binaries and the connection between spectral parameters and timing quantities are better understood (Nowak et al., 1999a; Pottschmidt et al., 2003; Axelsson et al., 2006, among many others). The evolution of the power spectral densities and time lags is discussed in Sects. 6.2.3 and 6.2.4.

6.1 Spectral Evolution

6.1.1 Spectral Classification

The classification of Cyg X-1 into states is done according to Wilms et al. (2006) and Remillard (2005). The most important parameters of the spectral fits for this purpose are the photon indices Γ_1 and Γ_2 of the broken power law described in Eq. 5.4. Γ_1 is a measure for the steepness of the spectral shape below the the break energy E_{break}, which is situated slightly above 10 keV in all fits done with this work. The steepness of the hard X-ray spectrum with energies higher than E_{break} is described by the second photon index Γ_2. The resulting plots of these fits are presented in Fig. 6.1. Cyg X-1 can be found in the hard state for the larger fraction of the observed time. The hard spectrum is explained by Comptonization within the accretion disk corona (Dove et al., 1997, 1998). In hard states, the total count rate in the energy band $2-4$ keV is the lowest compared to the other states. Additionally to the X-rays from the source, there is a steady detection of radio emission. For Cyg X-1, as well as for other sources, a jet outflow with mildly relativistic velocities is detected, which meant to be responsible for the radio emission (Stirling et al., 2001; Gallo et al., 2003, 2005). If the photon index exceeds a limit of $\Gamma_1 > 2.1$ the source leaves the defined hard state and enters its intermediate state. The intermediate state is described by a softening of the spectrum and increasing X-ray fluxes. Intermediate states have been observed in different cases. On the one

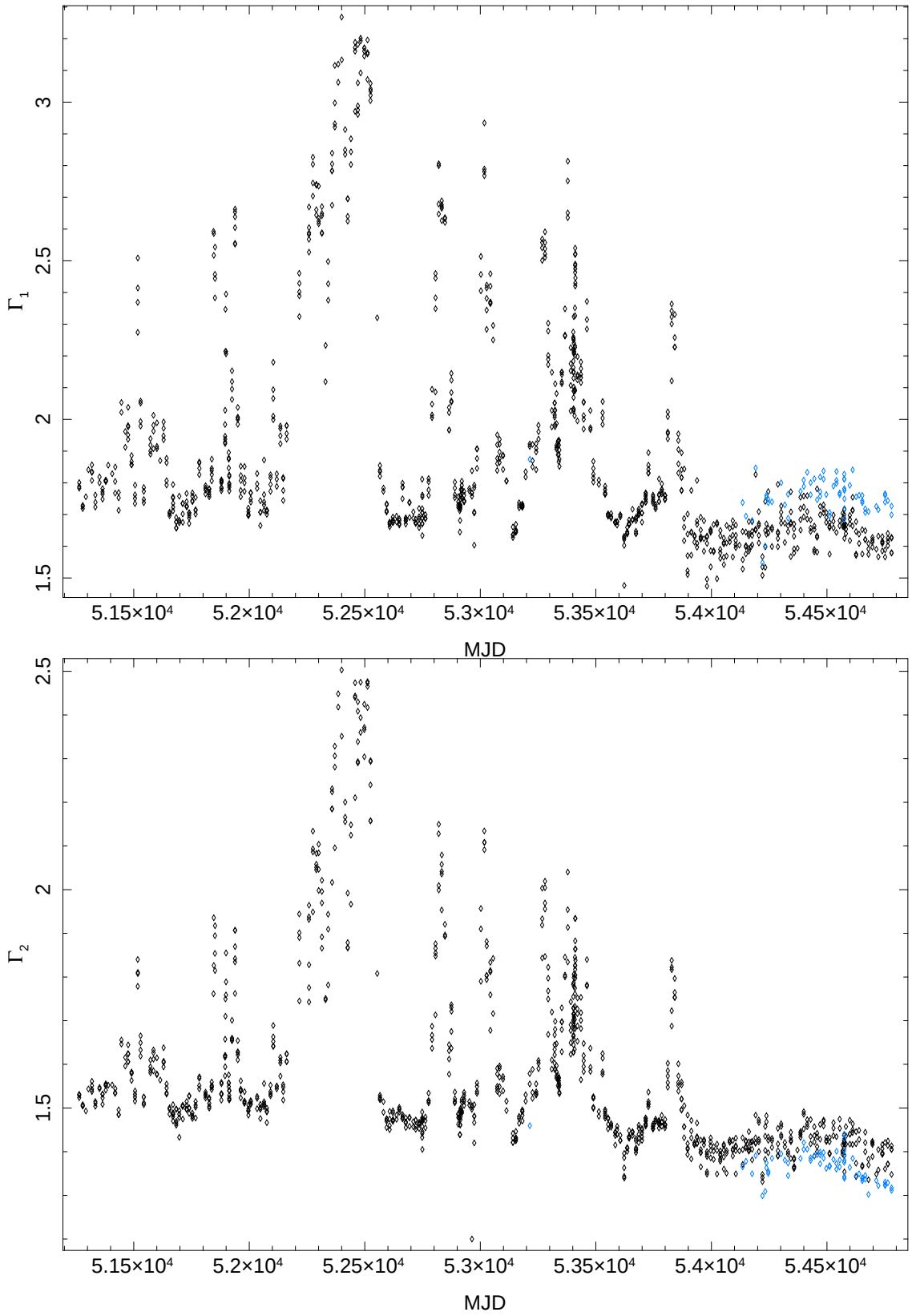

Figure 6.1: Temporal evolution of the photon indices of the broken power law fits. Blue triangles indicate the observations with a noticeable deviation in the Γ_2/Γ_1 correlation (see Text and Fig. 6.3 for further information.)

hand the intermediate state is passed through if the source does a complete state transition on its way from the hard to the soft state and vice versa (one of these transitions is the main topic of Böck, 2008). On the other hand there are so called "Failed State Transitions", where Cyg X-1's spectrum softens, but the transition to the soft/high state does not appear. Insted of the state transition the source can later be found again in the hard state. This failed state transitions go along with radio and X-ray flares in the most cases and show a different behavior in their timing properties with a drop in coherence and increasing time lags (Pottschmidt, 2002; Pottschmidt et al., 2003). A possible scenario for those flares is described by Wilms et al. (2007). The X-ray flare is caused by the ejection of a synchrotron-radiation emitting electron bubble from the jet base or the accretion disk area. While the blob is propagating outwards in the jet, it is expanding adiabatically and cooling down in the jet outflow. The peak of emission is more and more redshifted, what is proven by broadband measurements (Pooley & Fender, 1997). The time delay relating to the X-ray flare is increasing with the measured wavelength peak. The X-ray flare of Cyg X-1 was followed by a radio flare with ~ 7 minutes delay (Wilms et al., 2007).
In the soft/high state the spectrum is the steepest. The soft state is defined with $\Gamma_1 > 2.4$, but there are soft states in the data analyzed, where the photon index Γ_1 exceeds a value of 3. To achieve a good fit in the sense of a low χ^2-value, a thermal disk component (`diskbb`, see Sect. 5.1) has to be added to the total model. In the soft states with $\Gamma_1 > 2.8$ the values derived from the fit describe a multi-color disk with physically meaningful parameters at low photon energies. In observations of soft intermediate states and soft states with lower Γ_1 the spectral coverage of the PCA prevents from getting significant results. The accretion geometry and the radiative processes are different in the soft state (Gierliński et al., 1999). The soft states of Cyg X-1 are also characterized by a very weak or missing radio detection.
Another measure for the different states of black hole binaries is the correlation of the total X-ray luminosity with the spectral shape, what gives the states their alternate names: soft/high state and hard/low state. The X-ray luminosities of soft states exceed those of hard states by several times. It is helpful to consider hardness intensity diagrams (HID) to visualize this correlation. An example for a HID is the "q-diagram" shown in Sect. 3.5. HIDs are the X-ray analog of color magnitude diagrams, like the Hertzsprung-Russell-diagram, of optical astronomy. Instead of color or surface temperature, respectively, and absolute magnitude, the hardness intensity diagram is a plot of X-ray luminosity against spectral hardness ratio. The hardness ratio can be interpreted as the color of the X-ray source and is calculated with the count rates of different energy bands. The are two different ways to calculate the hardness in literature. In some cases it is written as the quotient of the high energy count rate divided by the low energy count rate, $\mathrm{cps_H}/\mathrm{cps_L}$. The convention used in this work is:

$$H = \frac{\mathrm{cps_H} - \mathrm{cps_L}}{\mathrm{cps_H} + \mathrm{cps_L}} \tag{6.1}$$

H is larger than 0, if there are more counts in the high energy band than in the low, and less than 0, if there are more counts in the low energy band, normalized by the sum of both bands. HIDs, calculated from two instruments, are presented in the course of this chapter. For PCA the spectral hardness ratio is derived from the count rates in the energy channels 2 (4.5–5.7 keV) and 4 (8.5–12.7 keV), the intensity is the sum of both energy bands' counts. A hardness ratio is also calculated for ASM data, which is included in Fig. 6.5. Here the energy ranges are 1.5–3 keV and 5–12 keV. A hardness intensity diagram of the whole ten-year-database of PCA observations is shown in Fig. 6.2. The color indicates the spectral state classification derived from the photon index Γ_1 of the broken powerlaw fits. This is actually a kind of double definition of the spectral state. The Γ_1-parameter of the broken power law fit and the calculation of the hardness describe both the steepness of the spectrum, but with a different approach. It would be ideally to see the color gradient of Γ_1 increasing straight with the hardness. The problem of color mixing in this plot is suspected to originate from the splitting of the lightcurves from one observation. There is one spectral model for a whole observation of a duration of several ksec, whereas the hardness is calculated for every

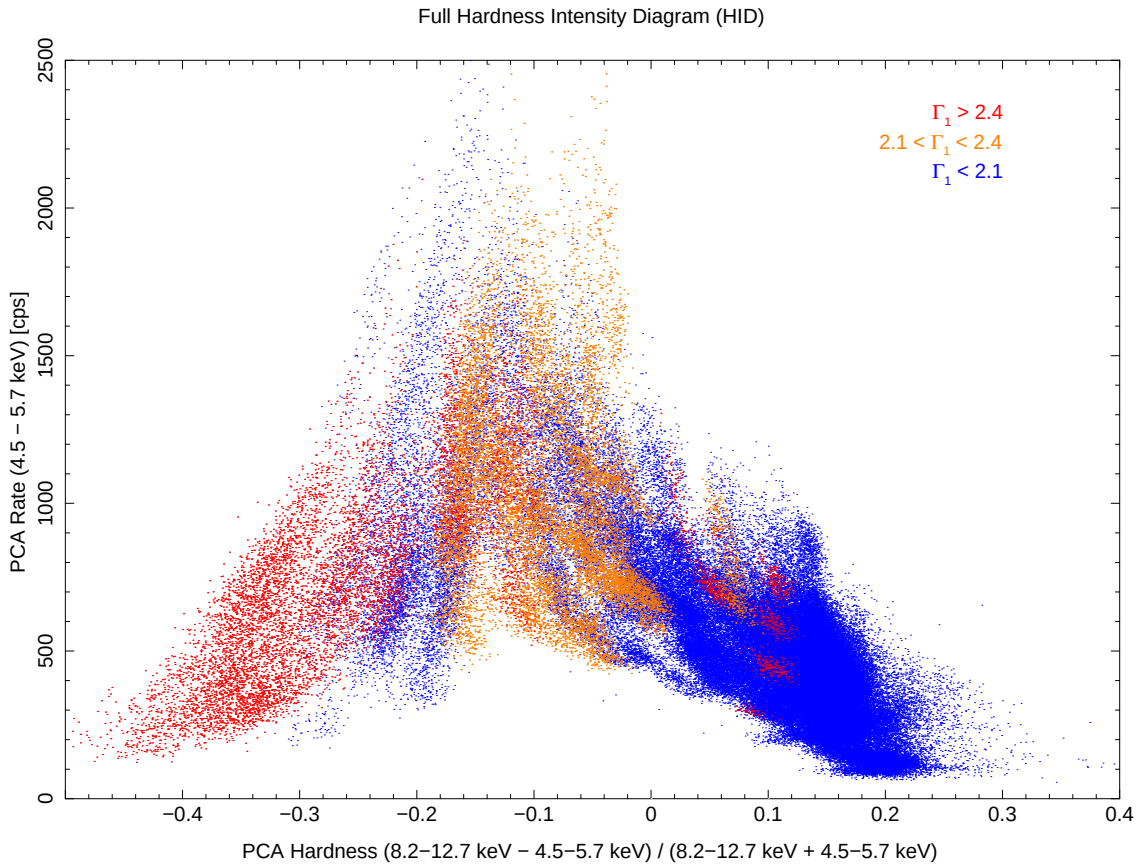

Figure 6.2: A full hardness intensity diagram of the Cyg X-1 data, which was used in this work is shown. The color code indicates a separate measure of the spectral state derived from the powerlaw fits. The expected color shift from red to blue is disturbed (see text).

16 s bin of the standard2f lightcurves. If the hardness changes during an observation, the same Γ_1 is used to colorize the different dots. The red regions at a hardness level of ~ 0.1 may be a sign of undiscovered state transitions on short timescale, which occur during a *RXTE* observation. The same holds for the blue area at a hardness of –0.2, where spectral fitting yields a hard spectrum at a position in the HID, where soft intermediate and soft states are located. An examination of spectra with shorter exposure times during this observations may solve this question.

6.1.2 Correlations of the Broken Powerlaw

There is a correlation between the two photon indices of the broken power law, shown by Wilms et al. (2006, Fig. 3.). The ratio Γ_1/Γ_2 is nearly constant over the whole spectral range. Fig. 6.3 shows, that this behavior can be reconstructed with the data of this work. The same holds for the correlation between the spectral hardening at the break energy $\Delta\Gamma = \Gamma_1 - \Gamma_2$ and the lower steepness parameter Γ_1. The correlation coefficients of these apparent linear correlations are summarized in Table 6.1.2. ρ_{linear} is computed with the ISIS function `correlation_coefficient`, which is part of the `isisscripts`. ρ_{Spearman} is Spearman's rank correlation coefficient (Keeping, 1995, Eq. 11.14.1). A similar correlation is seen by Zdziarski et al. (1999) with a single power law and Compton reflection model. Concerns about the independence of the fit parameters as stated therein, do not affect the correlation of the powerlaw indices used in this work as they are part of a phenomenological description of the spectral shape and are not linked in any way.

The plots presented in Fig. 6.3 reveals some data points deviating from the linear correlation in hard states with $\Gamma_1 < 1.9$. After the first spectral fitting, done within an energy range of 4–20

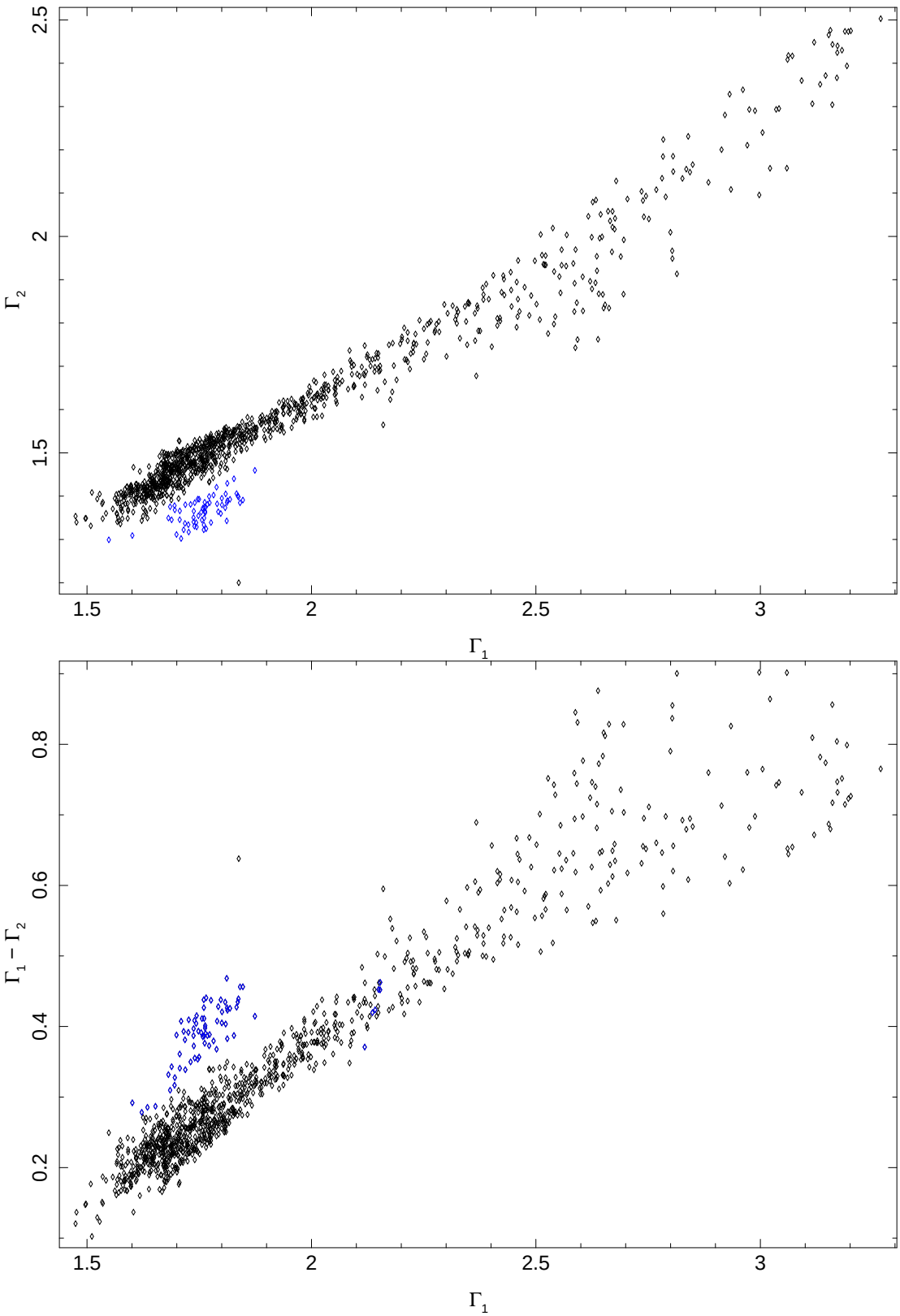

Figure 6.3: Top panel: Correlation between the soft power law index, Γ_1 , and the hard power law index, Γ_2, for the broken power law ts. Bottom panel: Correlation between the soft power law index, Γ_1 , and the difference of both photon indices, $\Gamma_1 - \Gamma_2$, which is a measure for the strength of the break in the spectrum. There are suspicious observations marked with blue diamonds in both plots, which deviate from the known relation. Undergoing a first analysis, these data points were found only in observations in the last two years (see 6.1, what indicates a possible change in the spectral behavior of Cyg X-1.)

Table 6.1: Correlation coefficients of the `bknpower` model parameters

	ρ_{linear}	ρ_{Spearman}
Γ_2 vs. Γ_1	0.9720	0.9067
$\Gamma_1 - \Gamma_2$ vs. Γ_1	0.9435	0.9132

keV, they were suspected to be artifacts of bad χ^2-statistics in observation with high photoelectric absorption in the interstellar and circumsource medium and for this reason the χ^2-minimization failed due to problems with the `phabs` model. To improve the spectral results in the course of this work, all spectral data were refitted with a low energy threshold of 5 keV to avoid $\chi^2_{\text{red}} \gtrsim 2$-values in some observations. The data points marked in blue color in Fig. 6.1 and Fig. 6.3 are those of these observations. It is notable that all of them (except one) are from observations in 2007 and 2008. Cyg X-1 was in a soft/high state for the last time in spring 2006 and is in a hard state since then. This new hard state is characterized by lower values of Γ_1 than in the earlier eight years of this dataset used herein. That spectrum seems to be flat over a wider energy range than in earlier hard states. An indication of the same behavior is to be found in *Suzaku* data, which is currently being analyzed by Nowak (2008, and priv. comm.). The possible new spectral properties will be subject of future work about Cyg X-1 in the work group at Remeis observatory.

6.1.3 The Iron Line Complex

Another part of a spectral fit is the iron Kα fluorescence line, modeled here with a Gaussian profile. Diagnostics on the shape of the iron line are not possible to the full extent with *RXTE* data. The low spectral resolution of PCA cannot reveal any details of the shape of the iron line. But, some diagnostics of the line flux and the position of the line are still possible. At the beginning of the fitting process, the position of the iron line was fixed at 6.4 keV. The three parameters of the Gaussian were thawed after a first identification of the broken powerlaw parameters. The position of the line still has to be confined within a certain limit of ± 0.4 keV, as the line energy was affected by fitting problems in the lowest energy bins of PCA. If the fit routines have problems with the photoabsorption or accretion disk parameters, the iron line tends to move to lower energies during χ^2-minimization. The area under the Gaussian profile was a complete free parameter. It is a measure for the total flux within the K α line. An increasing flux of the iron line with increasing Γ_1 can be interpreted as a brightening of the Kα emitting region in softer states. For this purpose a plot is shown in Fig. 6.4. The hard states with $\Gamma_1 < 2.0$ concentrate at a line flux of ~ 0.1 photons/(s cm^2). With increasing softness, there is a tendency of a linear increase of the iron line flux. The larger fraction of X-rays from the thermal disk causes more photons at 6.4 keV, due to the fluorescence of the iron in and surrounding the disk.
The overall spectral evolution is depicted in Fig. 6.5 on page 62. The plot shows the X-ray count rates of the PCA and ASM instruments aboard *RXTE* together with the fit results of the broken power law fits. The radio flux is plotted in the uppermost panel for comparison.

6.2 Spectro-Timing Analysis

6.2.1 PSD Overview

The basics of the timing analysis of Cyg X-1 are the quantities, which are calculated with ISIS (see Sect. 4.2. The power spectra and their correlation with the spectra of the source are in the main focus of this section. The values of coherence and time lag, which are calculated of cross power densities of different energy bands, are taken into account later. Section 4.2.2 explains the computation of the power spectral density and the basic shape of the PSD is depicted. Section 5.2 describes the main components of the fit model. To get an idea of the behavior of the power spectra's

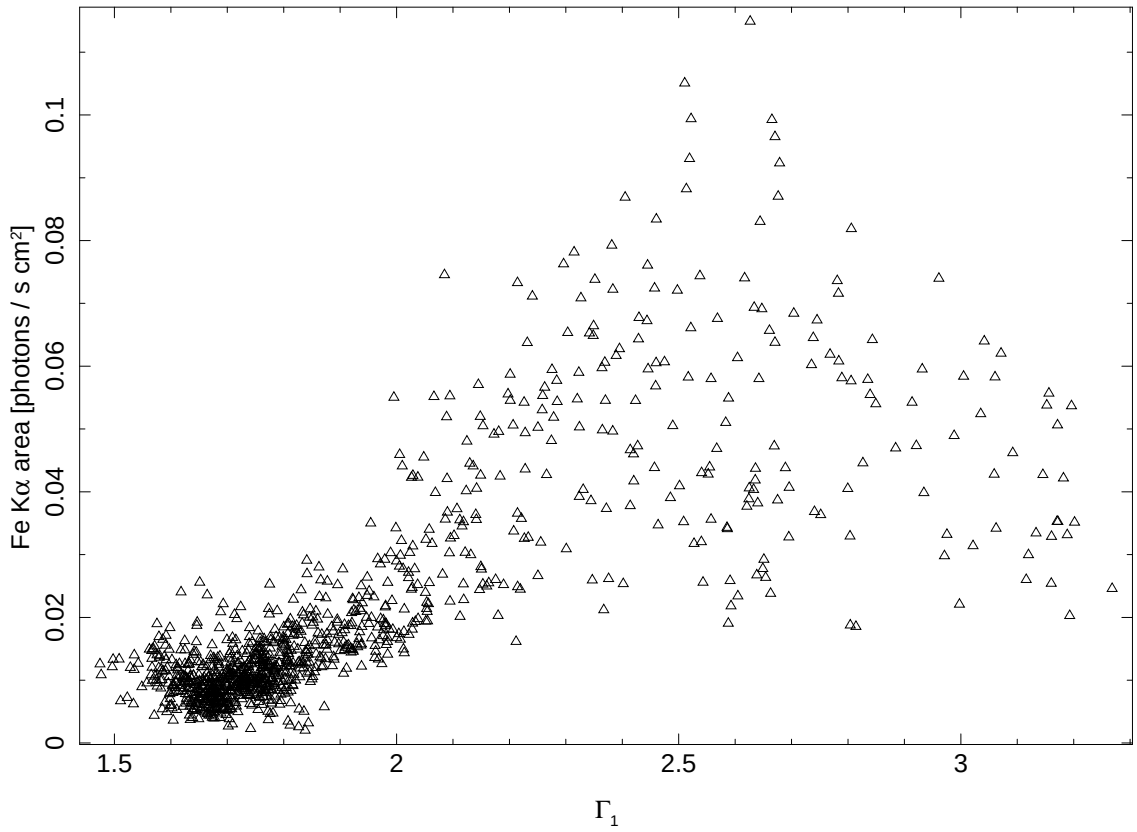

Figure 6.4: A noticeable brightening of the iron Kα line can be observed with increasing softness of the spectrum.

shape in respect to the spectral emission states of Cyg X-1, one can take a look at Fig. 6.6. The figure shows a "landscape" plot, which was created by M. Hanke (priv. comm.) with the Cyg X-1 campaign data of this work. The picture has to be interpreted as follows: The x-axis covers the the range of $\Gamma_1 = 1.5 - 3.2$. The y-axis is the Fourier frequency. A weighted average of all PSDs is plotted as a color-scale with its frequencies on the y-axis. The weight factor is a Gaussian function of Γ_1. PSDs with the exact values of the picture's column are weighted higher, than those with with differences to a column. This acts as a diffusor. The color depicts the rms-contribution of the power spectra at a certain frequency. In hard states there are three peaks, the frequencies of which are increasing with decreasing hardness. The third peak, which can be identified with the third Lorentzian of the PSD fits, is fading out at $\Gamma_1 < 2$. The other peaks remain, with rising frequency to $\Gamma_1 \approx 2.5$. At this point the state transition to the soft state occurs and a rather flat contribution of the powerlaw with exponential cutoff starts to dominate the power spectra. This picture can be taken as a general overview of the power spectra's behavior in all spectral states. In the following this behavour will be investigated in detail.

6.2.2 PSD Fit Results

The selection method of the best fits was the F-Test, which is described in Sect. 5.3. The hard state observations of Cyg X-1 are modeled best with two to four Lorentzian profiles (Pottschmidt et al., 2003; Nowak, 2000). Each Lorentzian has three free fit parameters, namely the peak frequency ν_i, the quality Q_i and the total rms contribution in Miyamoto normalization rms_i. No parameter boundaries were set for the rms, whereas the two other parameters were limited. The peak frequencies for all Lorentzians were set to a start value, which follows the correlation identified by Pottschmidt et al. (2003, Fig. 7 b). The upper or lower limit of the peak frequency, respectively,

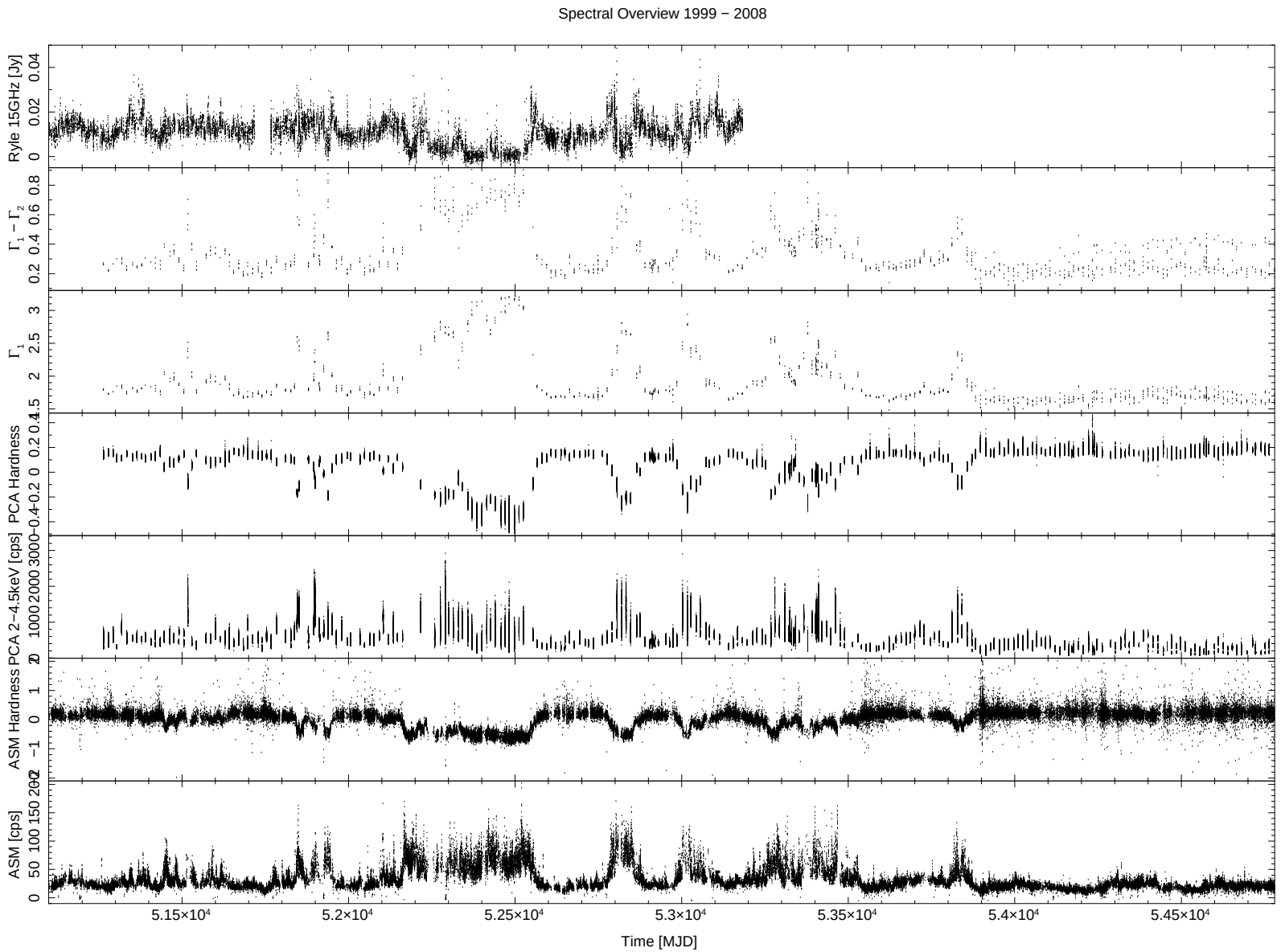

Figure 6.5: An overview of the spectral evolution of Cyg X-1 is depicted in this plot. The panels show from top to bottom: The measured radio flux of the Ryle telescope at 15 GHz, the power law break $\Gamma_1 - \Gamma_2$, the low energy photon index Γ_1 of the spectral fits, the hardness ratio calculated from PCA data, the PCA countrate in the lowest energy band, the hardness ratio calculated from ASM data between 1,5–3 keV and 5–12 keV and the total ASM flux of Cyg X-1.

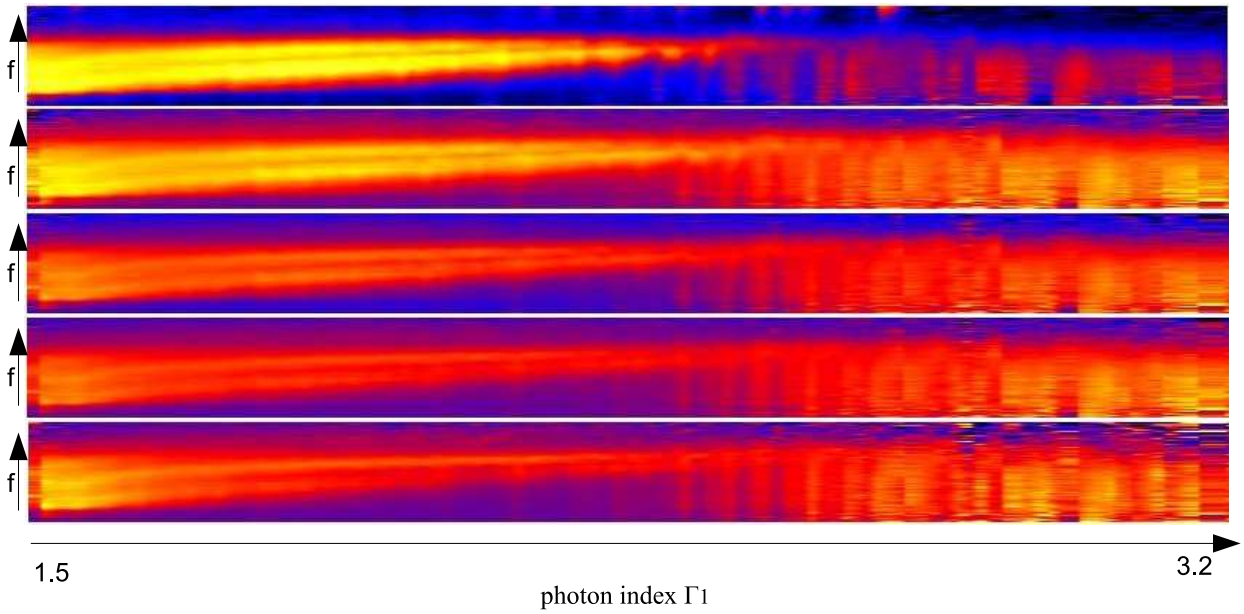

Figure 6.6: Landscape plots of the PSDs of all five energy bands. The PSDs of observations within a certain range of the photon index Γ_1 are plotted in vertical orientation. The y-axis is the logarithmic frequency. The color of each pixel depicts the rms-variability of the PSD in Miyamoto-normalization.

were fixed at a value, where none of the frequencies for two peaks were expected. In most cases the fit routines found a χ^2-minimum in this range without getting in contact with the borders. With this strategy the Lorentzians are prevented from changing their positions. The limits for the quality of the Lorentzians were between 0 and 2. A quality value of zero yields a maximum broad component, higher values of Q produce narrower peaks. As the main aim of this analysis is the evolution of broad noise components in the power spectra, narrower peaks, as commonly seen with QPOs, should not be modeled. After the first fitting cycle, a strong correlation between the rms and the quality of the first Lorentzian could be identified. Figure 6.7 shows a plot of rms_1 against Q_1. The colored contour map is the χ^2-confidence interval map (Hanke, 2007, Sect. 2.2.2) of those two parameters. A value within one of the ellipses is at 99%, 90% or 68.3% level caused by statistical fluctuations and is therefore not an intrinsic property of the sources. Shape and size of the confidence interval justifies connection between the two parameters. As the rms-parameter is of more physical interest, the quality parameter is frozen to a reasonable average. The quality of the first Lorentzian was tied to $Q_1 = 0.25$ as recommended by Pottschmidt et al. (2003).

The picture, which is created with help of the landscape plot, is approved by the fit results in all five energy bands. Figure 6.2.2 shows five exemplary plots of power spectra in different spectral states of the source. The selection of the best fit by the F-test shows a accumulation of models with three Lorentzians at low Γ_1 values. In hard states with higher Γ_1 the third Lorentzian is partially not needed to describe the power spectrum well. In intermediate states and in the region of the state transition the concentration of fits with a powerlaw component increases, whereas the number of Lorentzians is variable. In soft state observations of Cygnus X-1 the power law with exponential cutoff is part of every best fit. In some cases, which are accumulated in observations with the highest values of Γ_1, the powerlaw without additional components describes the PSD best. The peak frequencies of the three Lorentzians are getting higher with decreasing hardness. Plotting the peak position of the Lorentzians against the photon index of the spectral broken powerlaw fit yields the correlation, which was established by Pottschmidt et al. (2003, Fig. 7 b), for the whole ten years of Cyg X-1 monitoring (Fig. 6.9). The peak frequency of the third Lorentzian ν_3 is correlating only in the hardest observations (Nowak, 2000). At the transition to the intermediate

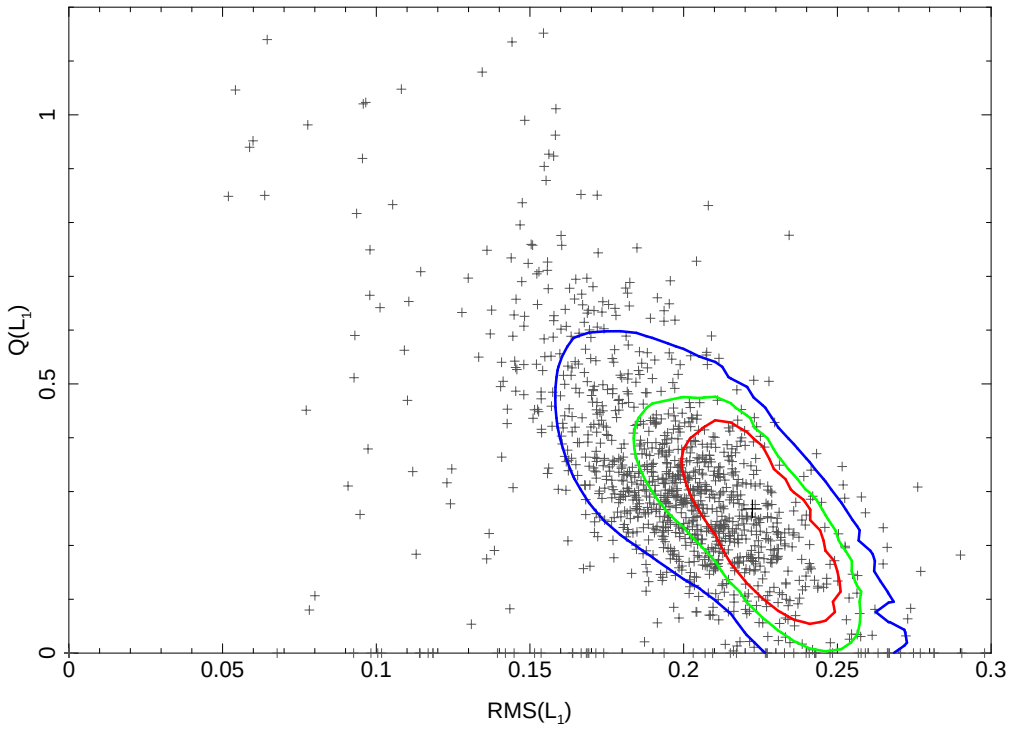

Figure 6.7: The confidence contour map of the parameters rms and Q. The datapoints of one energy band are shown in gray. Size and shape of the χ^2 confidence interval agree with the distribution of the fit results. The red line marks a 99% confidence interval, the blue line 90% and the green line 68.3%.

state at $\Gamma_1 \lesssim 2.1$, the third one disappears from the best models. In figure 6.10 the Lorentzian's peak frequencies $\nu_{1,2}$ of all five energy bands are plotted. The distribution of the points allows to conclude that there is no, or at least no distinctive, correlation between the peak frequency and the energy. The plot contains the whole set of more than 6000 PSDs from all states of the source. The fitting strategy in soft states was slightly different from that in the hard state. At low Γ_1 the borders of the peak frequency were set, as described above. In some cases, at lowest frequencies and in the region of the state transition, the parameters tended to run against the borders. The line shaped accumulations of data points, which can mainly be observed with the second Lorentzian, demark this constraint. Nevertheless, this is only a small fraction of the dataset, but the results have to be confirmed without this border crash. In soft states the fitting strategy of Böck (2008) was adopted. Here the frequency the second peak was $\nu_2 = \nu_1 + \delta\nu$, where $\delta\nu$ was fitted with the help of the `dummy` function to ensure the right order of the Lorentzians. As in this case no strong limitation to the frequency range was used, the range of frequencies appear wider than in the hard states. It can be noted, that although the peak frequencies change with the softening of the spectrum, their ratio is constant in all hard and intermediate state observation (Fig. 6.11).
Another correlation between spectral and timing properties is discussed by Belloni & Hasinger (1990). Especially in intermediate states, a connection between the break energy E_{break} of the spectrum and the rms of the power spectrum is discussed. This correlation could not be tested in this work, because the parameter space of E_{break} was choosen too narrow.

6.2.3 RMS–Frequency Correlation of the PSD

If one takes the rms of the Lorentzians into account, another connection between the parameters can be observed. The total rms of a power spectrum is the addition of three Lorentzian rms, if no powerlaw contributes to the fit. Gleissner et al. (2004) shows a correlation between the total rms

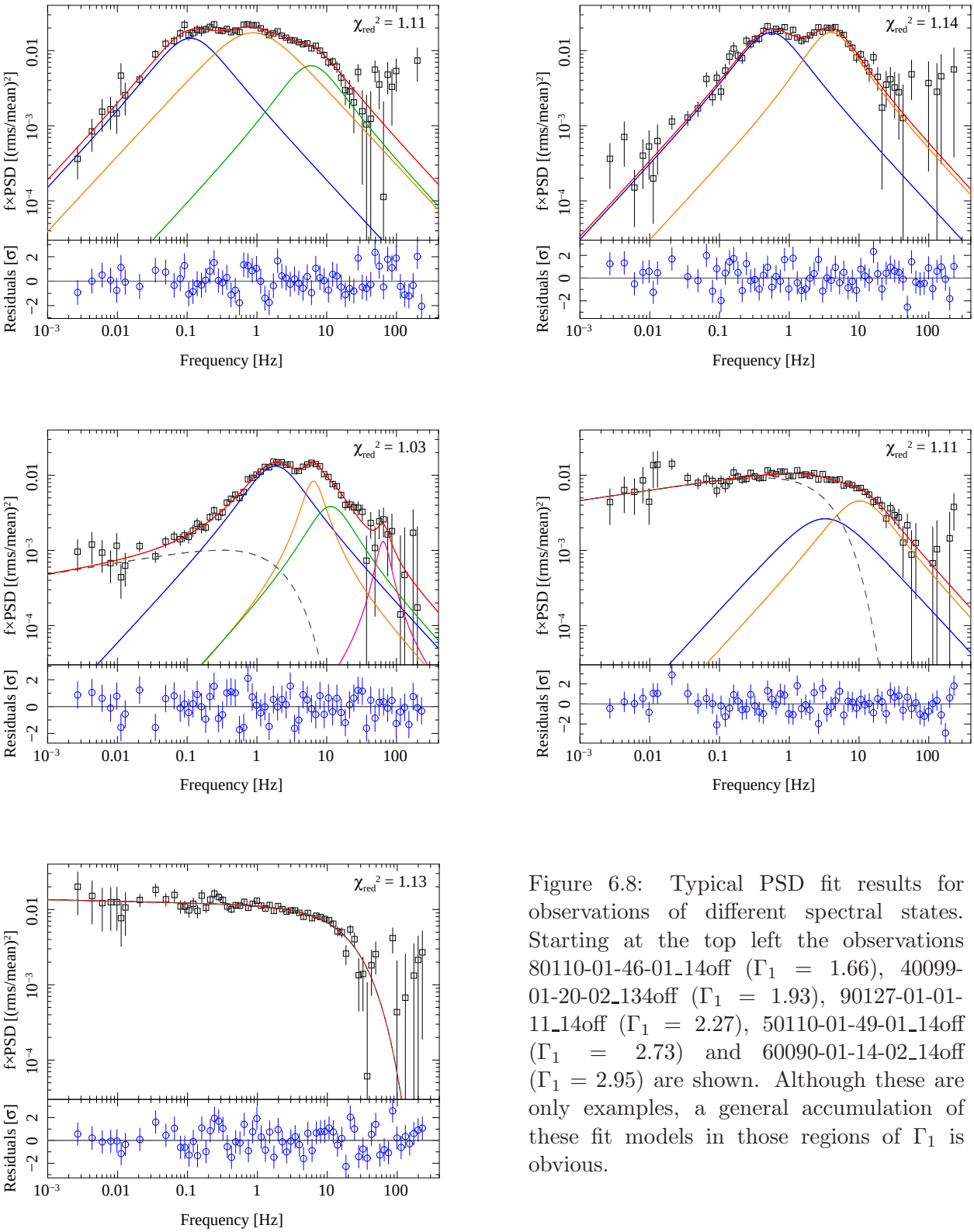

Figure 6.8: Typical PSD fit results for observations of different spectral states. Starting at the top left the observations 80110-01-46-01_14off ($\Gamma_1 = 1.66$), 40099-01-20-02_134off ($\Gamma_1 = 1.93$), 90127-01-01-11_14off ($\Gamma_1 = 2.27$), 50110-01-49-01_14off ($\Gamma_1 = 2.73$) and 60090-01-14-02_14off ($\Gamma_1 = 2.95$) are shown. Although these are only examples, a general accumulation of these fit models in those regions of Γ_1 is obvious.

variability of the power spectrum and the overall flux of the source. For all three Lorentzians, the rms normalization correlates with the peak frequency (see Fig. 6.2.3). Pottschmidt et al. (2003, Fig. 6) present a connection between the peak frequency and the rms of the Lorentzians. An interesting point is that this correlation is independent for all Lorentzians. In the Fourier frequency range, where two broad noise peaks can reside at different spectral hardnesses, the correlation is kept by both. This property was found by Pottschmidt et al. (2003) for the years from 1998

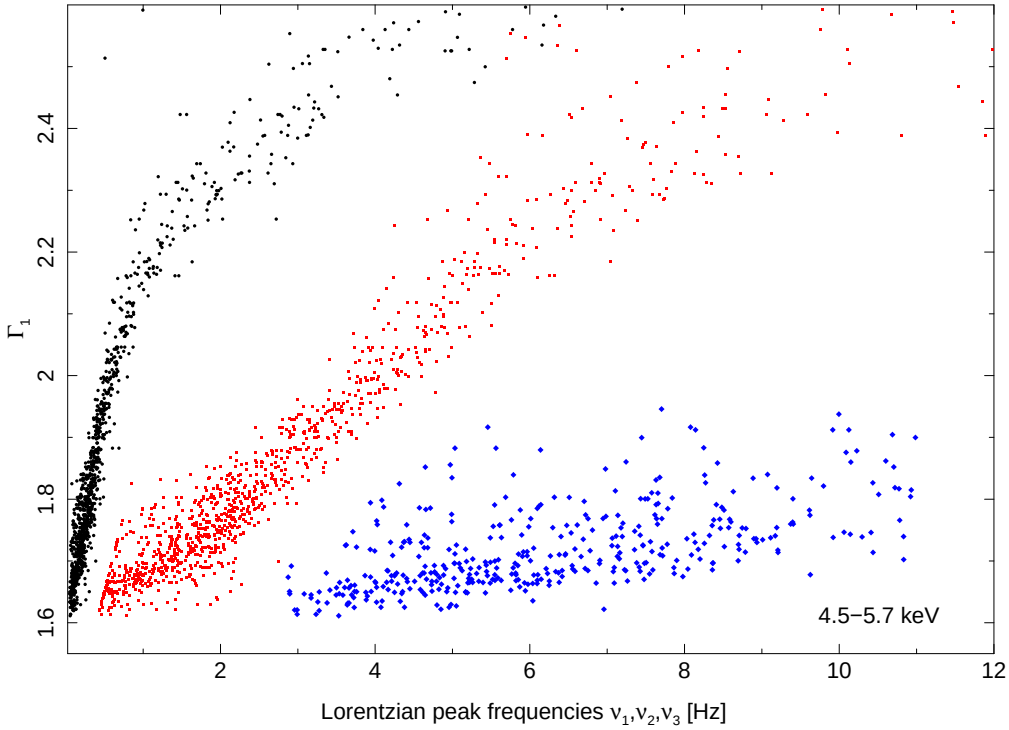

Figure 6.9: The correlation of three Lorentzian peak frequencies with the photon index Γ_1 in the second energy band for hard state observations. Black color indicates ν_1, red is for ν_2 and blue indicates ν_3

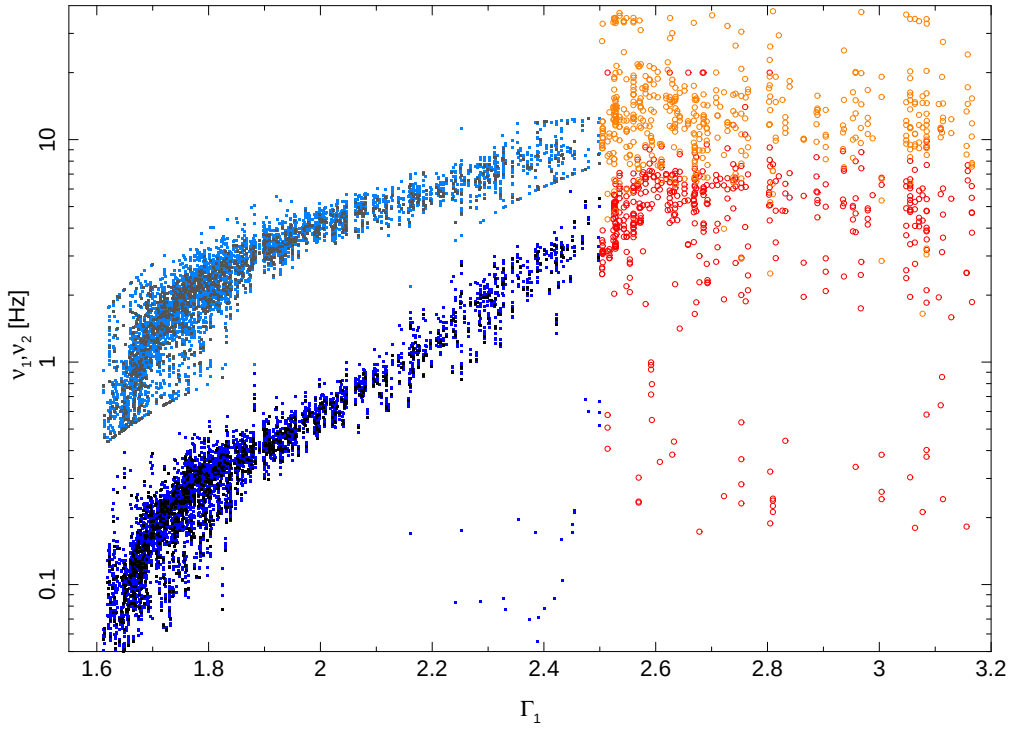

Figure 6.10: The position of the peak frequencies of the first two Lorentzians in all energy bands, which were part of all fit models, except those in soft states, where no Lorentzians were needed. The data of the first Lorentzian are colored in dark blue and red, those of the second in bright blue and orange. The black and gray dots are overplotted data of the second energy band. It shows at a first glance, that no energy dependency of the peak frequency has to be anticipated. See text for information about the fitting process and its problems.

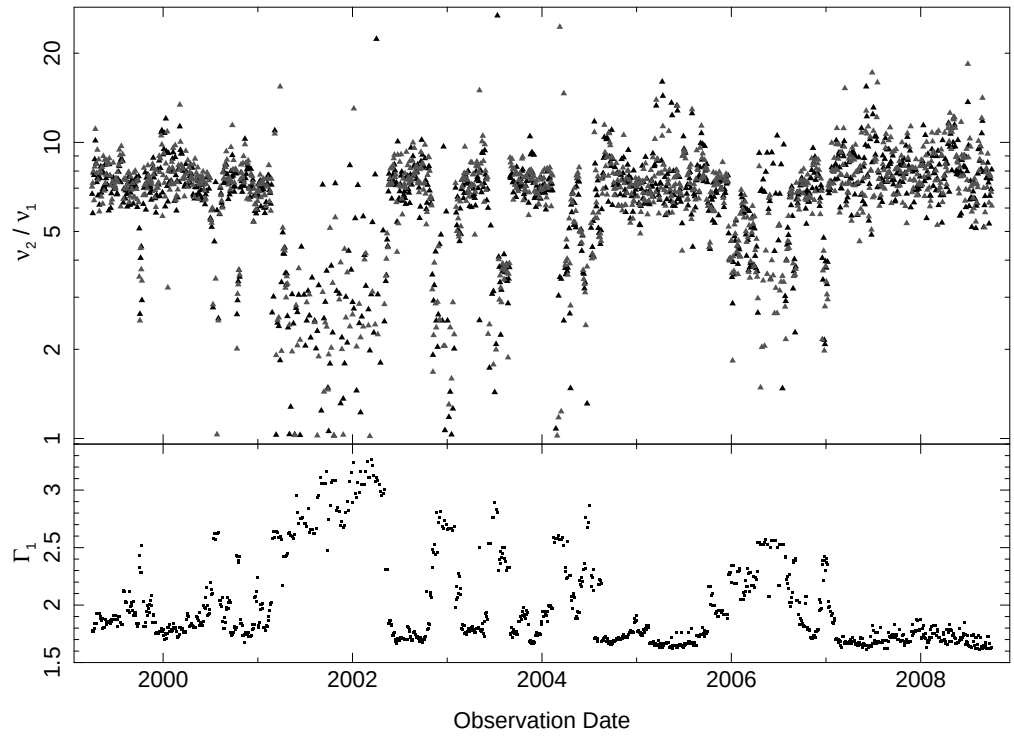

Figure 6.11: Ratio of the peak frequencies ν_2/ν_1 of the first two broad noise components plotted against time. The bottom panel depicts the photon index of the observations. In hard state observations the ratio is nearly constant, whereas in soft states there is no correlation between the Lorentzians.

to 2001. If this analysis is done by taking different energy bands into account, one observes a energy dependency of the shape of the plot. This is caused mainly by the first Lorentzian. misinterpretation of the overlap region due to permutation of two Lorentzians is again not possible, because of the parameter's upper and lower limits, respectively. The five plots of figure 6.2.3 confirm this assumption. Another hint for the rather strong energy dependency of the first Lorentzian's rms contribution was found by M. Böck (priv. comm.) in the course of simultaneous fitting of all five energy bands with one model. A similar, but smaller examination of the normalization parameter of the powerlaw can be done with soft state observation. The integral over the `cutoffpl2`-function yields the total rms contribution of the powerlaw in Miyamoto normalization. The powerlaw is fitted in all soft state observations and in ~ 100 hard states a model with a powerlaw was the best fit for the power spectrum. Figure 6.13 depicts, that the powerlaw has only a small contribution to the rms in the 100 hard states. Soft intermediate observations with $2.4 \lesssim \Gamma_1 \lesssim 2.7$ show a nearly linear correlation of the rms with increasing Γ_1. This value saturates in the very soft observations at 30 % for the `cutoffpl2` A complete compilation of the most important spectro-timing parameters can be found in Sect. 6.2.5. The temporal evolution of these values within ten years is there plotted.

6.2.4 Time Lag Spectra

The time lag spectra of Cyg X-1 were computed for all 1200 observations and all possible combinations of signal dominated energy bands. The time lag spectra show larger uncertainties than those calculated in previous attempts, due to the short observations. The uncertainties of the lag depend highly on the number of averaged segments, which is rather low, if the *RXTE* orbits are not combined to longer lightcurves. The shape of a single power spectrum is often quoted as proportional to $f^{-0.7}$. In the course of this work, the attempt to fit the lag spectra with a simple powerlaw, but

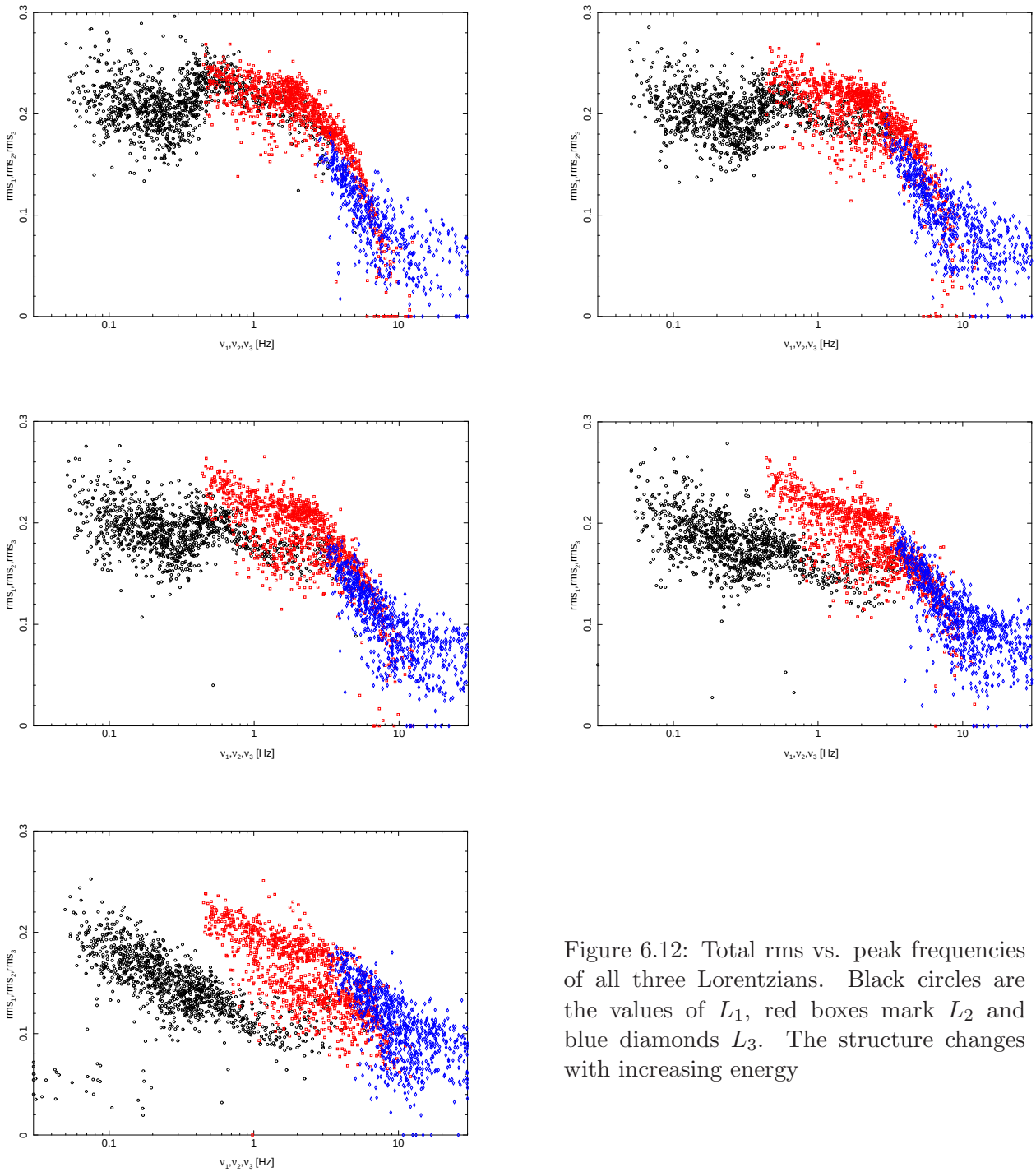

Figure 6.12: Total rms vs. peak frequencies of all three Lorentzians. Black circles are the values of L_1, red boxes mark L_2 and blue diamonds L_3. The structure changes with increasing energy

it turned out, that the uncertainties are too large, to obtain reasonable fit results. The steepness varied from -0.4 to -1.0 and it was obvious that the fit had problems to determine the shape of the lag spectrum. The values of the time lag are only calculated correctly if the underlying physical process is coherent. The coherence function of a typical hard state observation of Cyg X-1 and the corresponding time lag spectrum are shown in Fig. 6.14. The powerlaw, which is overplotted, was fitted by hand for demonstration of this correlation. Even if the attempt to fit the lag spectra failed, the calculated quantities could still be used for the timing analysis. Sections of the lag spectrum are rebinned to a broad logarithmic grid of 0.1–0.3 Hz, 0.3–1.0 Hz, 1.0–3.2 Hz and 3.2–10 Hz bins. These values show a strong energy dependency. The time lag increases with the difference of the energy bands. Körding & Falcke (2004) and Nowak et al. (1999b) explain the time lags between

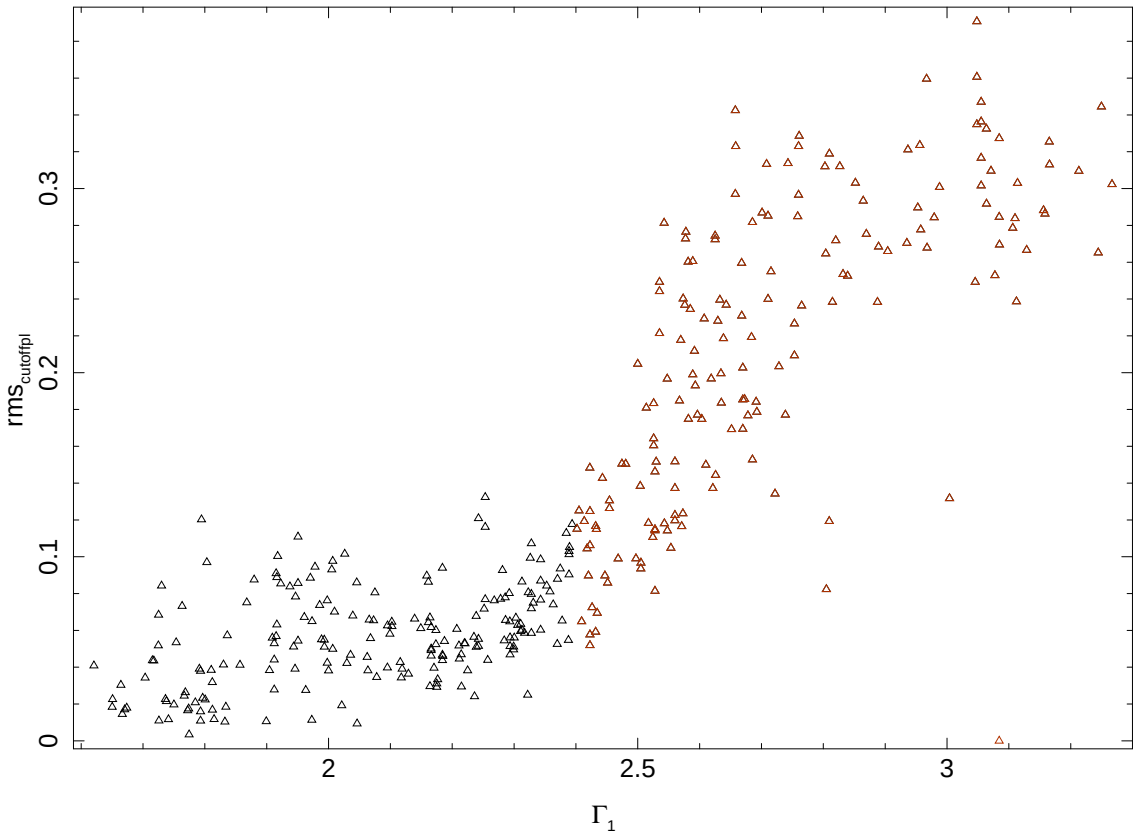

Figure 6.13: The contribution of the `cutoffpl2` function to the total rms of the PSD. The powerlaw starts to get interesting in soft intermediate states and dominates the power spectrum in soft states.

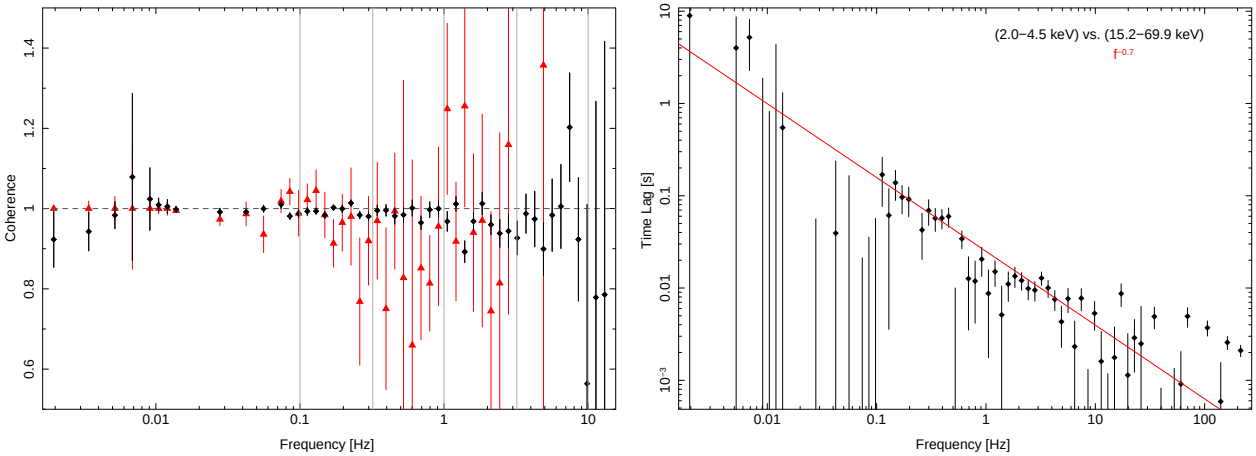

Figure 6.14: A typical hard state observation of Cygnus X-1. The processing and upscattering of photons in the comptonization medium seems to be a coherent process (left panel). The lag spectrum is modeled best with a f^{-7} powerlaw as depicted in the right panel. The uncertainties of the values are too high to compute the fit values for all observation automatically.

energy bands by the time Comptonization needs to upscatter the photons to higher energies. The models are applicable to the scenario of a Comptonization corona, as well as to a jet region, where the upscattering takes place. The thermal photons of the disk are reprocessed by a hot electron gas and gain energy by a certain number of inverse Compton scatterings. To achieve the energies, which are observed in the highest band, the number of interactions is much larger than for photons with energies slightly greater than those of the black body emission. Considering an average rate

of interactions per time interval explains the increasing time lag at higher energies. Fig. 6.15 shows the averaged time lags at a Fourier frequency of 1.0–3.2 Hz and 3.2–10 Hz, respectively, between three different energy bands over the whole ten years of Cyg X-1 campaign. The time lag is constant over large timescales in hard states and soft states as well. The bottom panel shows the ASM count rate and there are increases in the time lag together with X-ray flares. The third property of the time lags, next to their energy and Fourier frequency dependencies, is the rapid increase, when flaring events occur. As depicted in the long-term plots of Sect. 6.2.5, there is a correlation between the coherence and the lag. At state transitions the coherence drops and the lags increases to a multiple of the values in hard states. A change in the accretion geometry in this transition is a possible explanation for the higher timelags and low coherence in this period. Böck (2008) created color-coded HIDs, which show that the lag drops to a low value, when the source has entered the soft state and is dominated by the thermal disk.

6.2.5 Overview of ten years CygX-1 Observations

The plots shown here act as an overview of the most important spectral and timing parameters and their temporal evolution. The plots are made with slightly overlapping time arrays of about 20 days. One of them covers about 2.5 years of the Cyg X-1 monitoring campaign. The plots show the properties and correlations described above. The timing properties of soft states, which are marked with red diamonds in the topmost panel of the photon index, are remarkable. In most cases, the are coincident with unsual coherence and lag values. The state transition of Böck (2008) can be found in the third plot. It is covered with a higher density of observation, what made it suitable for a recessed study.

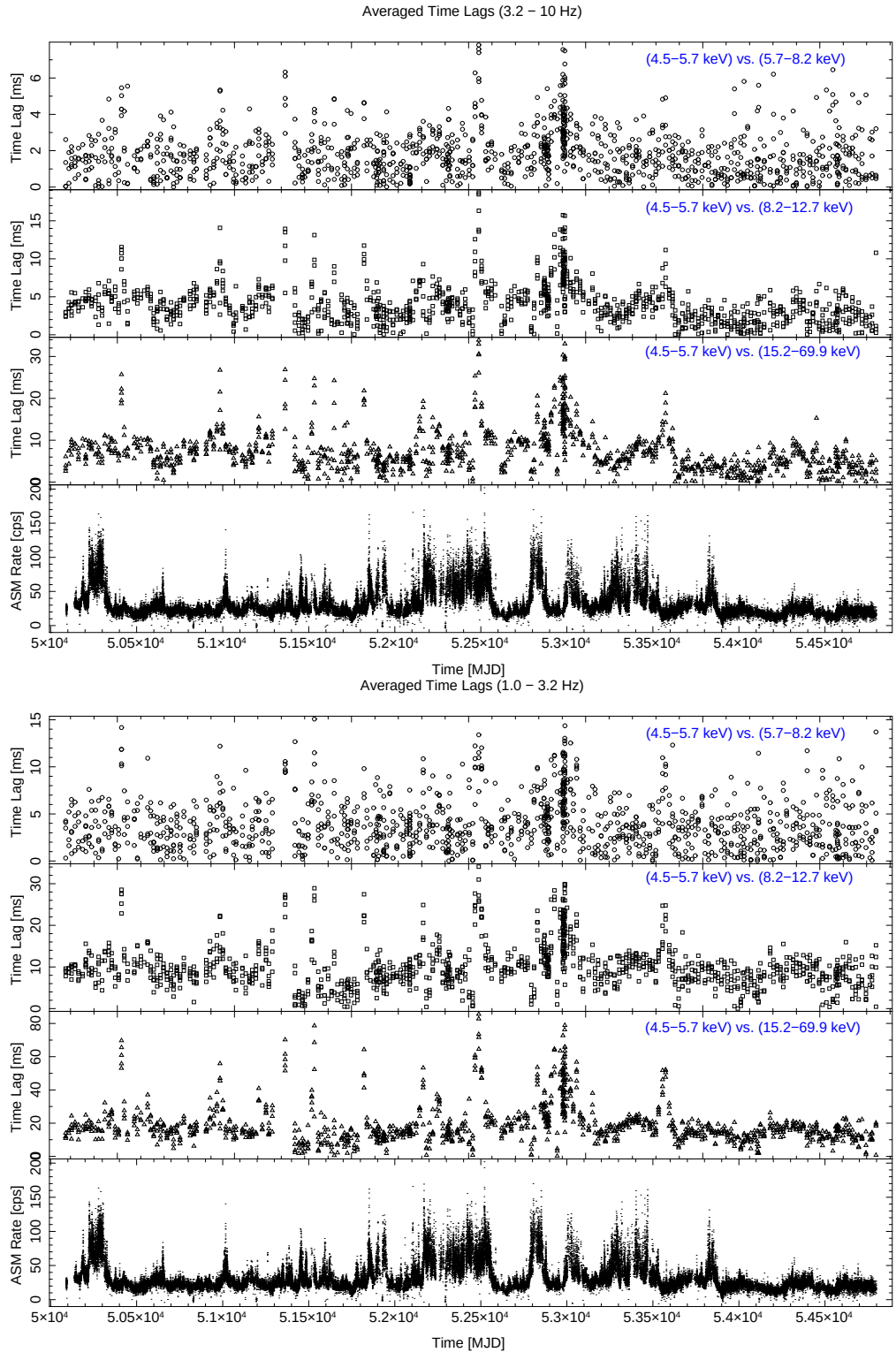

Figure 6.15: Averaged time lags of different energy band combinations at the Fourier frequency range of 1.0–3.2 Hz and 3.2–10 Hz.

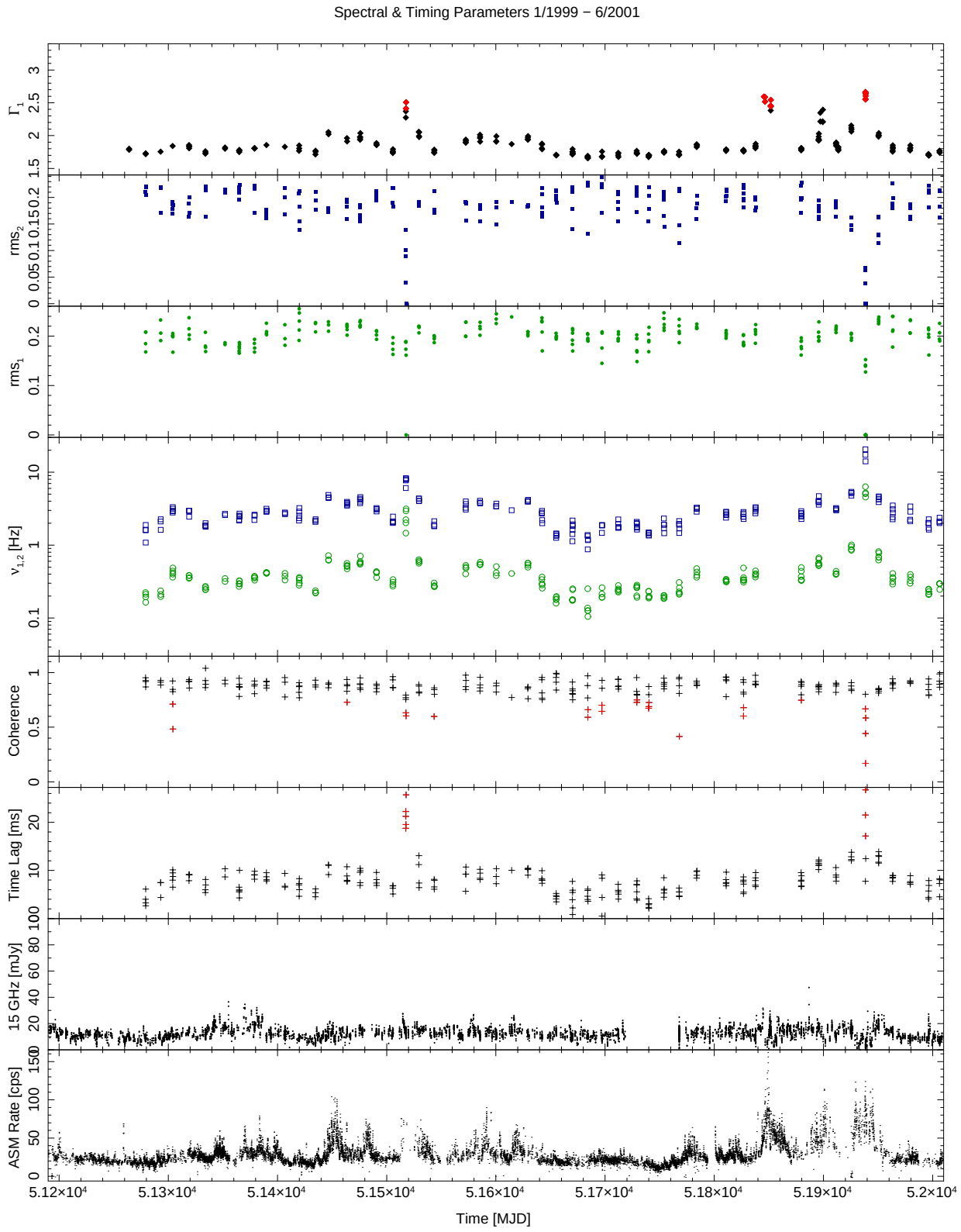

Figure 6.16: In the top panel, Γ_1 is plotted as a measure of spectral hardness. The peak frequencies $\nu_{1,2}$ and the rms contribution of the first two Lorentzians $\mathrm{rms}_{1,2}$ are shown below (green = L_1; blue = L_2). The cross power density quantities, time lag and coherence, respectively, are calculated of energy bands 2 and 5 within the Fourier frequency range 3.2–10 Hz and stated in the next two panels. The two bottommost panels are used for a plot of the total radio flux, detected at the position of Cyg X-1 with the Ryle telescope and the long-term lightcurve of the ASM in the 2-12 keV band. Remarkable peaks in coherence and time lag are colored red. Soft states with a photon index $\Gamma_1 > 2.4$ are also colored red in the topmost panel.

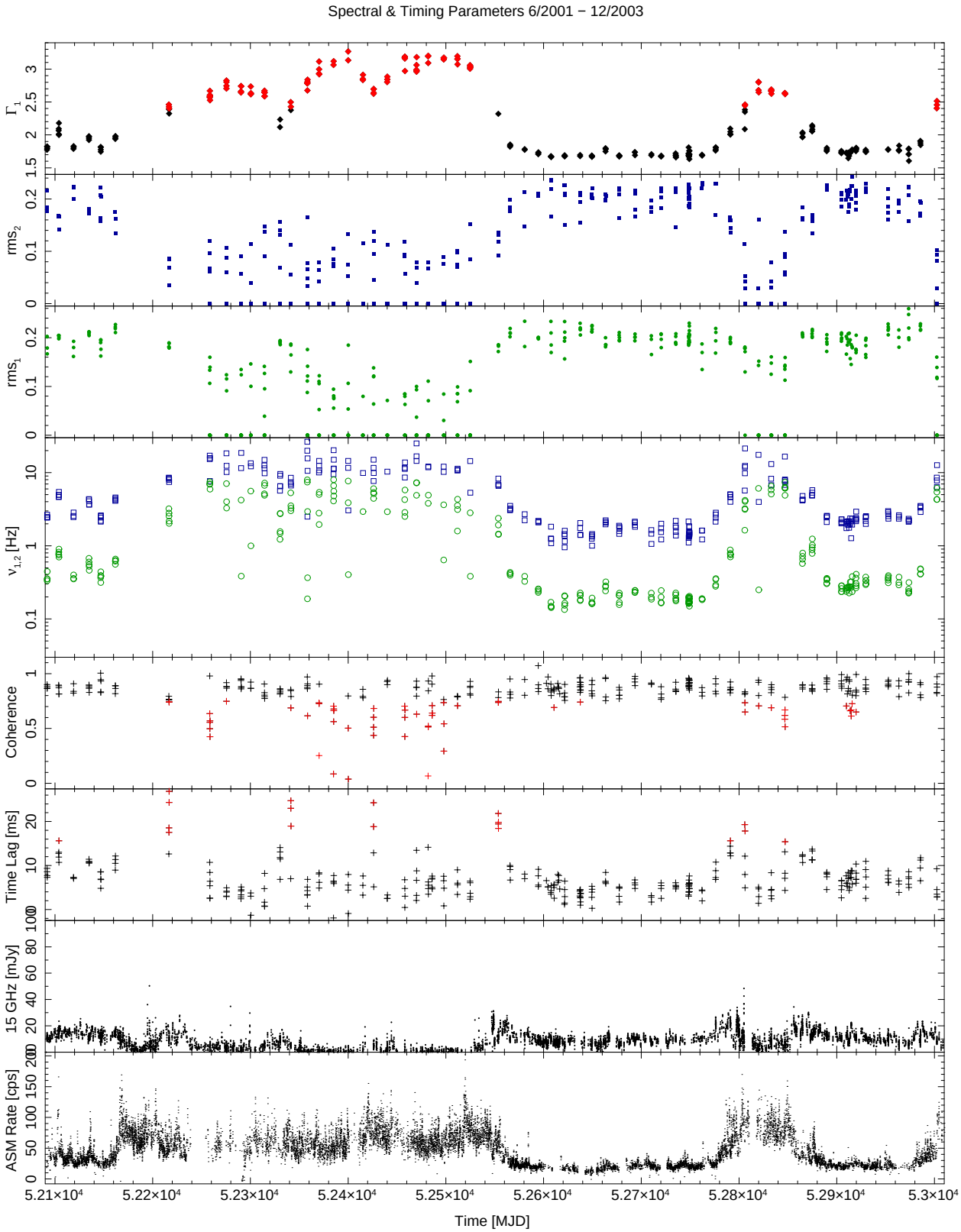

Figure 6.17: same as Fig. 6.16

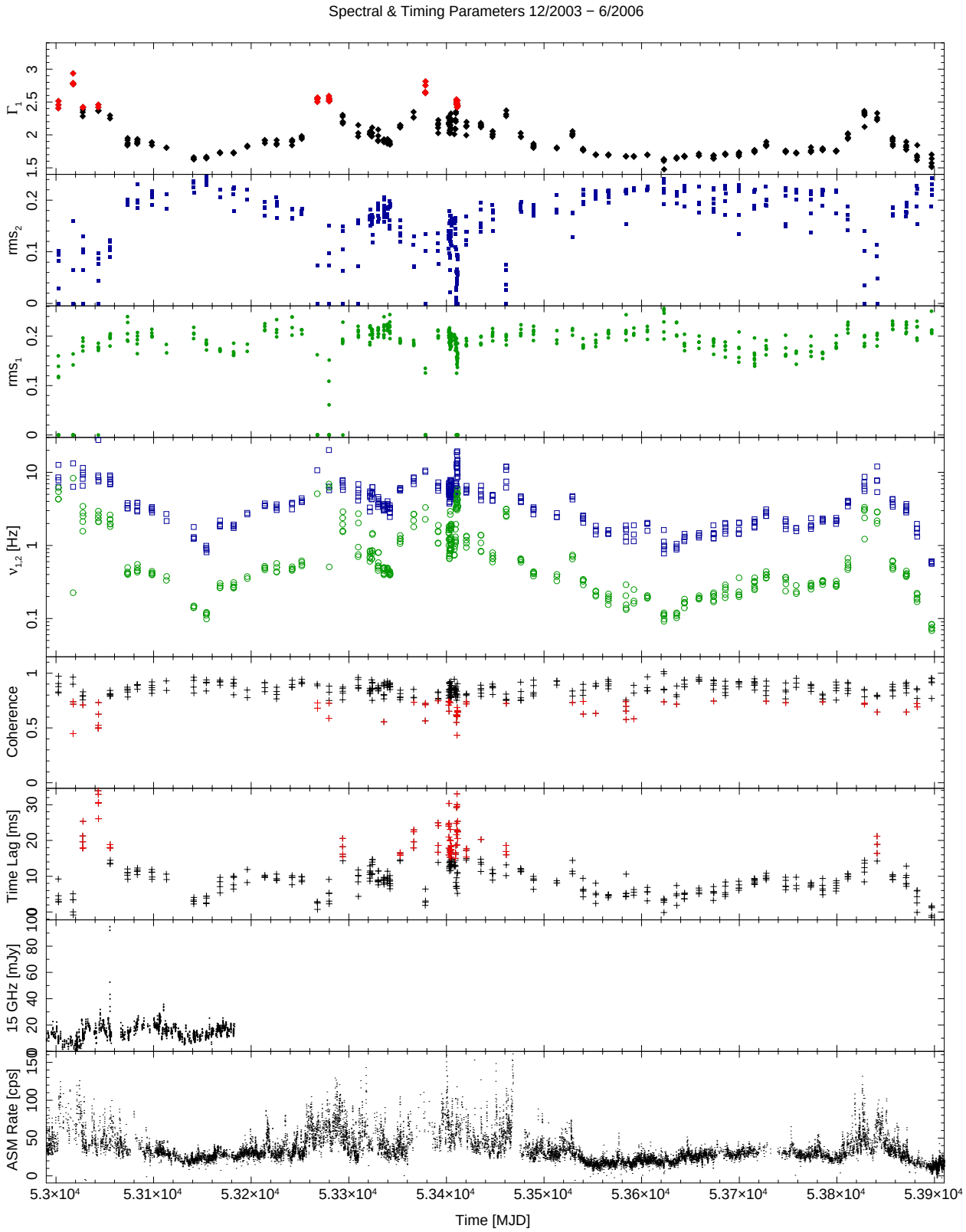

Figure 6.18: same as Fig. 6.16

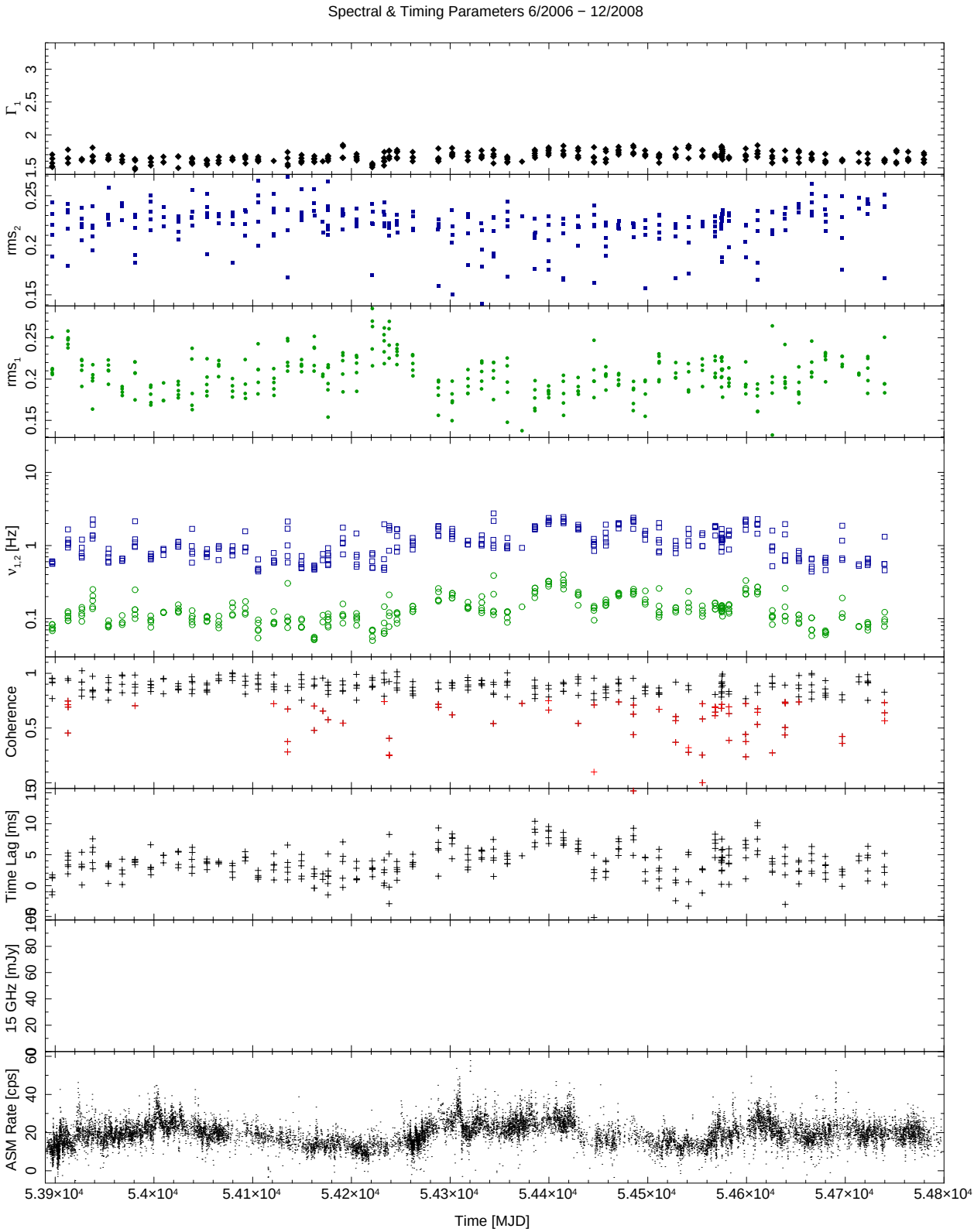

Figure 6.19: same as Fig. 6.16

Chapter 7

Summary & Outlook

The High Mass X-ray Binary Cygnus X-1 has been observed since 12 years with a long-term campaign with the Rossi X-ray Timing Explorer. A huge database of biweekly observations with the same datamodes was collected over the years. This work has analyzed ten years of those data, which were taken from 1999 to 2008. For the larger fraction of this time the Ryle Telescope has taken simultanous radio data. As Cygnus X-1 is one of the few known persistent HMXBs with a black hole as compact object, the data provide a great opportunity to study these objects over many years in multiple wavelength bands. The spectra of the source were fitted with the phenomenological model of a broken powerlaw to obtain the spectral properties of Cyg X-1 over the time. Several state transitions occured in the time between 1999 and 2006, which are included in the data. Cyg X-1 is usually found in the low/high state. In the data several soft states were also included, among them one with the highest photon index of the power law ($\Gamma_1 \approx 3.3$) in 2002 and a short soft state in early 2005, which was subject to the diploma thesis of Moritz Böck (2008). In the last two years, beginning in late 2006, Cygnus X-1 came to persistent low/hard state and no X-ray or radio flares occured. The photon index of the powerlaw is one of the hardest ever observed ($\Gamma_1 \approx 1.5$). Cygnus X-1 showed a slightly different broken powerlaw spectrum in the last two years. It has to be checked, if there is a possible change in its general spectral behavior.
The second scope of this work was the combined Fourier timing analysis of the lightcurves, which are available beides the spectra. Following mainly the PhD thesis of Katja Pottschmidt (2002), a software package for computations of Fourier quantities was developed. The resulting power spectral densities (PSD) and lag spectra were also subject to previous works. The combined spectro-timing analysis reveals more information about the X-ray source than the simple view on the spectra. Known correlations between spectral and timing parameters, obtained from modelling the power spectra with Lorentzians in hard states, a powerlaw with exponential cutoff in soft states and a mixture of both in state transitions, were proven. The results of Pottschmidt et al. (2003) from 1997–2001 are nested mostly in our data and the results of spectral-timing correlations could be confirmed over a wide range. The modeling of hard state PSDs showed a clear correlation between the photon index Γ_1 and the peak frequencies of the two to three Lorentzians, which describe the PSD best in this state. The correlation between the rms and the peak frequency of these Lorentzians seems to have a energy dependancy, which was seen for the first time in this database.In some soft state PSDs no evidences for broad noise components were found. The variability of the source is here described best with a single powerlaw. The time lags calculated for different combinations of measured energy bands, show an energy dependency, as well as a correlation to the energy difference between the bands. This is in agreement with models, which describe the spectrum of Black Hole binaries with a Comptonization corona, in or around the accretion disk, where the soft seed photons are reprocessed and upscattered to higher energies. The lags show a significant increase, when a X-ray and radio flare was detected. In most cases the state changes after these events, but there are also a number of failed state transitions, in which the spectral state drops back to the hard state after evidences for a softening were apparent.

Böck (2008) analyzed a single state transition and put into question, what the exact changes in the emission of Cyg X-1 are, when a transition happens. This is still part of his current work. The hardness intensity diagram of this work has possibly revealed more of these transition, which are on short timescales and therefore undiscovered so far. A next step in the examination of the campaign data is the test of physical models with the data. Expanding the spectrum to even higher photon energies, taking *Integral* observations into account, and studying the radio emission of the jet in more detail is a possible extension to the analysis presented here. Victoria Grinberg will start her diploma thesis here at Remeis observatory soon and is going to focus on this questions. Even if Cygnus X-1 leaves many questions about its nature open, there are still more X-ray binaries to study and our techniques should also be used on their data.

Bibliography

Axelsson M., Borgonovo L., Larsson S., 2006, Astron. Astrophys. 452, 975

Balbus S.A., Hawley J.F., 1998, Reviews of Modern Physics 70, 1

Bardeen J.M., Carter B., Hawking S.W., 1973, Communications in Mathematical Physics 31, 161

Begelman M.C., Blandford R.D., Rees M.J., 1984, Reviews of Modern Physics 56, 255

Belloni T., 2005, In: Burderi L., Antonelli L.A., D'Antona F., di Salvo T., Israel G.L., Piersanti L., Tornambé A., Straniero O. (eds.) Interacting Binaries: Accretion, Evolution, and Outcomes, Vol. 797. American Institute of Physics Conference Series, p.197

Belloni T., Hasinger G., 1990 227, L33

Bendat J.S., Piersol A.G., 2000, Random Data, New York, Wiley-VCH, 2000

Benlloch S., Pottschmidt K., Wilms J., et al., 2004, In: Kaaret P., Lamb F.K., Swank J.H. (eds.) X-ray Timing 2003: Rossi and Beyond, Vol. 714. American Institute of Physics Conference Series, p.61

Bevington B.R., Robinson D.K., 1992, Data reduction and error analysis for the physical sciences, New York, WCB McGraw-Hill, 1992

Blandford R.D., Znajek R.L., 1977, MNRAS 179, 433

Böck M., 2008, *Master's thesis*, Dr. Remeis Observatory Bamberg, Germany

Bowyer S., Byram E.T., Chubb T.A., Friedman H., 1965, Sci 147, 394

Bradt H.V., Rothschild R.E., Swank J.H., 1993, Astron. Astrophys. Suppl. Ser. 97, 355

Brocksopp C., Fender R.P., Larionov V., et al., 1999a, MNRAS 309, 1063

Brocksopp C., Tarasov A.E., Lyuty V.M., Roche P., 1999b, Astron. Astrophys. 343, 861

Casella P., Belloni T., Homan J., Stella L., 2004, Astron. Astrophys. 426, 587

Chandrasekhar S., 1931a, MNRAS 91, 456

Chandrasekhar S., 1931b, Astrophys. J. 74, 81

Charles P.A., Seward F.D., 1995, Exploring the X-ray universe, Cambridge, New York: Cambridge University Press

Churazov E., Gilfanov M., Revnivtsev M., 2001, MNRAS 321, 759

Coppi P.S., 1999, In: Poutanen J., Svensson R. (eds.) High Energy Processes in Accreting Black Holes, Vol. 161. Astronomical Society of the Pacific Conference Series, p. 375

Dove J.B., Wilms J., Maisack M., Begelman M.C., 1997, Astrophys. J. 487, 759

Dove J.B., Wilms J., Nowak M.A., et al., 1998, MNRAS 298, 729

Einstein A., 1916, Annalen der Physik 354, 769

Fender R., 2002, In: Guthmann A.W., Georganopoulos M., Marcowith A., Manolakou K. (eds.) Relativistic Flows in Astrophysics, Vol. 589. Lecture Notes in Physics, Berlin Springer Verlag, p. 101

Frank J., King A., Raine D., 1992, Cambridge Astrophysics Series 21

Fürst F., Wilms J., Rothschild R., et al., 2009, Earth and Planetary Science Letters, in press

Gallo E., Fender R., Kaiser C., et al., 2005, Nature 436, 819

Gallo E., Fender R.P., Pooley G.G., 2003, MNRAS 344, 60

Genzel R., Eckart A., 1999, In: Falcke H., Cotera A., Duschl W.J., Melia F., Rieke M.J. (eds.) The Central Parsecs of the Galaxy, Vol. 186. Astronomical Society of the Pacific Conference Series, p.3

Ghez A.M., Morris M., Becklin E.E., et al., 2000, Nature 407, 349

Gierliński M., Zdziarski A.A., Poutanen J., et al., 1999, MNRAS 309, 496

Gies D.R., Bolton C.T., 1986, Astrophys. J. 304, 371

Gies D.R., Bolton C.T., Fender R., et al., 2003, In: Bulletin of the American Astronomical Society, Vol. 35. Bulletin of the American Astronomical Society, p.1332

Gleissner T., Wilms J., Pottschmidt K., et al., 2004, Astron. Astrophys. 414, 1091

Gruber D.E., Blanco P.R., Heindl W.A., et al., 1996, Astron. Astrophys. Suppl. Ser. 120, C641

Hanke M., 2007, *Master's thesis*, Dr. Remeis Observatory Bamberg, Germany

Hanke M., Wilms J., Nowak M.A., et al., 2009, Astrophys. J. 690, 330

Heger A., Fryer C.L., Woosley S.E., et al., 2003, Astrophys. J. 591, 288

Herrero A., Kudritzki R.P., Gabler R., et al., 1995, Astron. Astrophys. 297, 556

Hjellming R.M., Wade C.M., 1971, Astrophys. J. 168, L21

Houck J.C., Denicola L.A., 2000, In: Manset N., Veillet C., Crabtree D. (eds.) Astronomical Data Analysis Software and Systems IX. ASP Conf. Ser. 216, p. 591

Iben, Jr. I., Renzini A., 1983, ARA&A 21, 271

Iben I.J., 1991, ApJS 76, 55

Iben I.J., Tutukov A.V., Yungelson L.R., 1995, ApJS 100, 217

Jahoda K., Markwardt C.B., Radeva Y., et al., 2006, ApJS 163, 401

Jahoda K., Swank J.H., Giles A.B., et al., 1996, In: Siegmund O.H., Gummin M.A. (eds.) Proc. SPIE Vol. 2808, p. 59-70, EUV, X-Ray, and Gamma-Ray Instrumentation for Astronomy VII, Oswald H. Siegmund; Mark A. Gummin; Eds., Vol. 2808., p.59

Karttunen H., Krüger P., Oja H., et al., (eds.) 2007, Fundamental Astronomy

Keeping E.S., 1995, Introduction to Statistical Inference, New York, Dover Publications, 1995.

Kerr R.P., 1963, Phys. Rev. Let. 11, 237

Körding E., Falcke H., 2004, Astron. Astrophys. 414, 795

Kreykenbohm I., 2004, Ph.D. thesis, Universität Tübingen

Lachowicz P., Zdziarski A.A., Schwarzenberg-Czerny A., et al., 2006, MNRAS 368, 1025

Larwood J., 1998, MNRAS 299, L32

Leahy D.A., Darbro W., Elsner R.F., et al., 1983, Astrophys. J. 266, 160

Levine A.M., Bradt H., Cui W., et al., 1996, Astrophys. J., Lett. 469, L33

Liang E.P., Nolan P.L., 1984, Space Sci. Rev. 38, 353

Magdziarz P., Zdziarski A.A., 1995, MNRAS 273, 837

Makishima K., Maejima Y., Mitsuda K., et al., 1986, Astrophys. J. 308, 635

Malzac J., 2007, Memorie della Societa Astronomica Italiana 78, 382

Markoff S., 2005, Astrophys. Space. Sci. 300, 189

Markoff S., Nowak M.A., Wilms J., 2005, Astrophys. J. 635, 1203

McClintock J.E., Remillard R.A., 2003, ArXiv e-prints (astro-ph/0306213)

McConnell M., Ryan J., Zdziarski A., et al., 2002, APS Meeting Abstracts 17078–+

Meschede D., 2002, Gehrtsen Physik, 21th edition, Berlin, Springer, 2002.

Miller J.M., 2007, ARA&A 45, 441

Miller J.M., Fabian A.C., Wijnands R., et al., 2002, Astrophys. J. 578, 348

Mitsuda K., Inoue H., Koyama K., et al., 1984, Publ. Astron. Soc. Jpn. 36, 741

Miyamoto S., Kitamoto S., Iga S., et al., 1992, Astrophys. J., Lett. 391, L21

Ninkov Z., Walker G.A.H., Yang S., 1987, Astrophys. J. 321, 425

Nowak M.A., 2000, MNRAS 318, 361

Nowak M.A., 2006, In: VI Microquasar Workshop: Microquasars and Beyond.

Nowak M.A., 2008, ArXiv e-prints (astro-ph/08101519)

Nowak M.A., Lehr D.E., 1998, In: Non-linear Phenomena in Accretion Disks around Black Holes., p.233

Nowak M.A., Vaughan B.A., 1996, MNRAS 280, 227

Nowak M.A., Vaughan B.A., Wilms J., et al., 1999a, Astrophys. J. 510, 874

Nowak M.A., Wilms J., Vaughan B.A., et al., 1999b, Astrophys. J. 515, 726

Oda M., 1977, Space Sci. Rev. 20, 757

Oppenheimer J.R., Snyder H., 1939, Physical Review 56, 455

Oppenheimer J.R., Volkoff G.M., 1939, Physical Review 55, 374

Pooley G.G., Fender R.P., 1997, MNRAS 292, 925

Pooley G.G., Fender R.P., Brocksopp C., 1999, MNRAS 302, L1

Pottschmidt K., 2002, Ph.D. thesis, Universität Tübingen

Pottschmidt K., Wilms J., Nowak M.A., et al., 2003, Astron. Astrophys. 407, 1039

Press W.H., Teukolsky S.A., Vetterling, W. T.and Flannery B.P., 1992, Numerical recipes in C. The art of scientific computing, Cambridge: University Press, —c1992, 2nd ed.

Priedhorsky W.C., Terrell J., Holt S.S., 1983, Astrophys. J. 270, 233

Remillard R.A., 2005, ArXiv e-prints (astro-ph/0504129)

Remillard R.A., McClintock J.E., 2006, ARA&A 44, 49

Reynolds C.S., Nowak M.A., 2003 377, 389

Roe P.R., 2001, Probability and Statistics in Experimental Physics, New York, Springer, 2001

Rohlfs K., Wilson T.L., 2004, Tools of radio astronomy, Tools of radio astronomy, 4th rev. and enl. ed., by K. Rohlfs and T.L. Wilson. Berlin: Springer, 2004

Rothschild R.E., Blanco P.R., Gruber D.E., et al., 1998, Astrophys. J. 496, 538

Rowan T., 1990, Ph.D. thesis, Univ. Texas at Austin

Rybicki G.B., Lightman A.P., 1979, Radiative processes in astrophysics, New York, Wiley-Interscience, 1979.

Schlittgen H.J., 1995, Zeitreihenanalyse, München, R.Oldenbourg, 1995

Schutz B.F., 1985, A First Course in General Relativity, A First Course in General Relativity, by Bernard F. Schutz, pp. 392. Cambridge, UK: Cambridge University Press, February 1985.

Schwarzschild K., 1916, Pr.Akad.Wiss. 1916, 189

Shakura N.I., Sunyaev R.A., 1973, Astron. Astrophys. 24, 337

Stirling A.M., Spencer R.E., de la Force C.J., et al., 2001, MNRAS 327, 1273

Sunyaev R.A., Titarchuk L.G., 1985, Astron. Astrophys. 143, 374

Sunyaev R.A., Trümper J., 1979, Nature 279, 506

Szostek A., Zdziarski A.A., 2007, MNRAS 375, 793

Thompson A.R., Moran J.M., Swenson, Jr. G.W., 2001, Interferometry and Synthesis in Radio Astronomy, 2nd Edition, Interferometry and synthesis in radio astronomy by A. Richard Thompson, James M. Moran, and George W. Swenson, Jr. 2nd ed.

Thorne K.S., 1974, Astrophys. J. 191, 507

Titarchuk L., 1994, Astrophys. J. 434, 570

van der Klis M., 1989, In: Ögelman H., van den Heuvel E.P.J. (eds.) Timing Neutron Stars., p. 27

Vaughan B.A., Nowak M.A., 1997, Astrophys. J. 474, L43

Walborn N.R., 1973, Astrophys. J., Lett. 179, L123+

Webster B.L., Murdin P., 1972, Nature 235, 37

Wilms J., 1998, Ph.D. thesis, Universität Tübingen

Wilms J., Allen A., McCray R., 2000, Astrophys. J. 542, 914

Wilms J., Nowak M.A., Pottschmidt K., et al., 2006, Astron. Astrophys. 447, 245

Wilms J., Pottschmidt K., Pooley G.G., et al., 2007, Astrophys. J. 663, L97

XTE-Staff 1995, Appendix F: The XTE Technical Appendix

Zdziarski A.A., Lubinski P., Smith D.A., 1999, MNRAS 303, L11

Zhang W., Jahoda K., Swank J.H., et al., 1995, Astrophys. J. 449, 930

Ziółkowski J., 2005, MNRAS 358, 851

List of Figures

1.1 Opacity of the Earth atmosphere . . . 2

2.1 Schematic view of the *RXTE* spacecraft . . . 4
2.2 Location of the SAA and *RXTE*'s orbit . . . 5
2.3 View of *RXTE*'s assembly . . . 5
2.4 A typical *RXTE* observation . . . 6
2.5 HEXTE's scintillation counters . . . 7
2.6 ASM Instrument . . . 8
2.7 The Ryle Telescope . . . 9

3.1 Hertzsprung-Russell diagram . . . 11
3.2 Effective gravitational potential of a binary system . . . 15
3.3 Accreting mechanisms in HMXB and LMXB . . . 15
3.4 Sketch of the emission by disk and jet . . . 17
3.5 Possible geometries of a Compton corona . . . 19
3.6 Iron line diagnostics . . . 20
3.7 Overview of the most important states of BHBs . . . 21
3.8 The q-diagram . . . 22
3.9 Location of Cygnus X-1 . . . 23
3.10 Radio image of the Cyg X-1 region . . . 24
3.11 Radial velocity curve of HDE 226868 . . . 26
3.12 Orbital modulation of X-ray and radio flux . . . 27
3.13 Superorbital modulation . . . 28
3.14 Geometry of the tilted accretion disk . . . 29
3.15 General Relativity frequencies in an accretion disk . . . 30

4.1 Source and background dominated PSD . . . 35
4.2 Lightcurves in different time resolutions and the computed PSD in two usual depictions 37
4.3 Example PSD with effective noise level . . . 39
4.4 Deadtime influence on the noise component for different numbers of activated detectors 40
4.5 Vector representation of the cross power density . . . 41
4.6 Coherence spectra of Cyg X-1 . . . 43
4.7 A time lag spectum of Cyg X-1 . . . 44

5.1 Components of PCA's response matrix . . . 46
5.2 Photoabsorption for different column densities . . . 49
5.3 Bad PSD statistics and resulting fit problems . . . 52
5.4 Overview of all five hard state power spectral density models . . . 53

6.1 The resulting photon indices from broken powerlaw fits . . . 56
6.2 Hardness intensity diagram of Cygnus X-1 . . . 58
6.3 Correlation between the photon indices of the broken powerlaw model . . . 59

6.4 Area of the iron line vs. powerlaw index Γ_1 61
6.5 Overview of Cyg X-1 spectral evolution over 10 years 62
6.6 Γ_1 – PSD Landscapes 63
6.7 Quality-rms Confidence map of the first Lorentzian 64
6.8 Overview of different PSD fit results 65
6.9 Correlation of peak frequency and photon index 1 66
6.10 Correlation of peak frequency and photon index 2 66
6.11 Ratio of the peak frequencies 67
6.12 Lorentzian peak frequency vs. rms in all 5 energy bands 68
6.13 Cutoff-powerlaw domination of soft states 69
6.14 Lag and coherence of a typical Cygnus X-1 hard state 69
6.15 Averaged time lags of different energy bands 71
6.16 Spectral-temporal overview of Cyg X-1 (Part 1) 72
6.17 Spectral-temporal overview of Cyg X-1 (Part 2) 73
6.18 Spectral-temporal overview of Cyg X-1 (Part 3) 74
6.19 Spectral-temporal overview of Cyg X-1 (Part 4) 75

Danksagungen

Wenn eine Arbeit, die auf Englisch verfasst wurde, mit einer erweiterten deutschen Zusammenfassung beginnt, dann darf sie auch mit “Danksagungen” enden.
Ich möchte mich abschließend bei allen bedanken, die mir während meiner einjährigen Arbeitszeit an dieser Diplomarbeit zur Seite gestanden haben. Beginnen möchte ich im Erdgeschoß der Dr. Karl Remeis–Sternwarte bei meinem Betreuer Jörn Wilms, der mir in den letzten knapp eineinhalb Jahren viel Freunde an der Astrophysik, speziell natürlich an der Röntgenastrophysik vermittelt hat. Wenn man ihn einmal in seinem Büro antrifft, steht er immer mit Ratschlägen und guten Ideen zur Seite und beantwortet geduldig alle Fragen, die ein Diplomand nur so stellen kann. In Zeiten der Abwesenheit ist er, wenn man die Zeitverschiebung mit einberechnet, die dann oft zwischen ihm und Bamberg liegt, auch per E-Mail oder Telefon immer erreichbar und hilft so gut er kann. Das Arbeitsgebiet der Röntgenastronomie, speziell mit Objekten wie Neutronensternen, galaktischen schwarzen Löchern und aktiven Galaxienkernen, über das ich auch bis vor einigen Wochen noch Vorlesungen bei ihm gehört habe, finde ich seitdem ich an die Sternwarte kam, sehr faszinierend.
Die Dr. Karl Remeis–Sternwarte in Bamberg ist ein Arbeitsplatz, der nicht nur wegen des historischen Gebäudes und des mehrere Hektar großen Geländes, ein hervorragender Platz ist, um Astronomie zu betreiben, auch herrscht hier ein sehr angenehmes Klima unter den Mitarbeitern. Die, die mir am nächsten standen, während meiner Diplomarbeitszeit sind meine Zimmerkollegen Manfred Hanke und Moritz Böck. Mein Gegenüber und Schreibtischmitbewohner Manfred, der einer Sucht erlegen ist, eine unkrautartig wachsende Pflanze zu vermehren, hat geduldig alle 10.000 Fragen, die ich ihm zu ISIS gestellt habe, beantwortet und weiß auf jede astrophysikalische Fragestellung eine Antwort oder zumindest die passende Referenz. Auch bei Moritz möchte ich mich für viele lehrreiche Unterhaltungen über Cygnus X-1 und die Analysen des Objekts bedanken. Seine Diplomarbeit war ein ständiger Begleiter und ein Nachschlagewerk in den letzten Wochen meiner Arbeit. Im Nebenzimmer sorgen Felix, Christian und Laura auch immer für gute Gespräche und gute Laune. Bei Laura muß ich mich an dieser Stelle entschuldigen. Da ich ja in ihrer Anwesenheit schon immer perfekt hochfränkischen Dialekt spreche, gibts es jetzt auch noch die Danksagung auf Deutsch. Sorry! Im Erdgeschoß gilt es noch das Zimmer mit Ingo Kreykenbohm und Matthias Kadler zu erwähnen. Mehrmals täglich komme ich dort zu Besuch vorbei und es entstanden entweder fachliche, oder auch lustige, aber auf jeden Fall immer gute Diskussionen. Auch den übrigen Mitarbeitern der Sternwarte aus den anderen Arbeitsgruppen möchte ich an dieser Stelle danken, daß man hier so nett und freundlich aufgenommen wurde. Außerhalb Bambergs gilt es noch Katja Pottschmidt zu erwähnen, deren Methoden und IDL Programme ich hier in meiner Arbeit umgesetzt habe. Auch bei ihr möchte ich mich für die vielen Hilfestellungen zu Fragen rund um Software und Cygnus X-1 bedanken. Victoria Grinberg, die jetzt mit mir gerade auf Wohnungssuche in Bamberg ist, gilt auch ein besonderer Dank, da sie mir in der Anfangsphase meiner Arbeit Vergleichswerte aus der Vorläufersoftware produziert hat, mit denen ich meine Programme testen konnte. Jetzt zum Ende hin war sie mein Ansprechpartner, was Cygnus X-1 betrifft, in meist nächtlichen Chatgesprächen am Computer. Viel Glück für die anstehenden Diplomprüfungen! Zum Abschluß möchte ich mich noch bei Maggy, die gerade in Amerika weilt, dafür bedanken, daß sie mir genug in den Hintern getreten hat, daß ich irgendwann nach langem Studium doch nochmal dazu gekommen bin, eine Diplomarbeit zu schreiben. Wenn ich jetzt jemanden vergessen habe, so möge auch er sich bedankt fühlen; es könnte einfach an der Uhrzeit liegen, zu der ich diese Seite mit Buchstaben fülle. Meinen Eltern gilt noch ein besonderer Dank, daß sie mich über das gesamte Studium hinweg (nicht nur finanziell) unterstützt haben.


JORGE CHAM © 2009
THE ORIGIN OF THE THESES
WWW.PHDCOMICS.COM